Exploring Inorganic Materials Synthesis Prediction with High Dimensional Phase Diagrams

by

Jiadong Chen

A dissertation submitted in partial fulfillment
of the requirements for the degree of
Doctor of Philosophy
(Materials Science and Engineering and Scientific Computing)
in the University of Michigan
2024

Doctoral Committee:

Assistant Professor Wenhao Sun, Chair
Associate Professor Bryan R. Goldsmith
Professor Elizabeth A. Holm
Professor Emmanouil Kioupakis
Associate Professor Liang Qi

Jiadong Chen

jiadongc@umich.edu

ORCID iD: 0009-0004-7603-8838

Dedication

This dissertation is dedicated to communities with an interest in materials science and computational modeling, with special dedication to one of the pioneers of modern thermodynamics – Josiah Willard Gibbs.

Acknowledgements

Thank everyone who has showed up over the past five years of my PhD journey.

First and foremost, I want to express my deepest gratitude to my advisor, Prof. Wenhao Sun. Thank you for assigning me a project that spans so many applications, demonstrating significant impact and depth. I am continually learning and am inspired by your vision and enthusiasm. I vividly recall the day we walked down the hallway and you suggested I thought about my research across every other group. I was surprised then because I felt it could not be done, and I am surprised now because I see that it is indeed possible. You are the one who encouraged and guided me into the competent computational materials scientist I am today. As an international student, language barriers initially hindered my presentations, but your guidance quickly boosted my confidence in communicating my research effectively.

It is my truly pleasure to be your student, and now, to become your first PhD to graduate. I struggle to find the words to express my gratitude to you. All my thoughts and feelings can only condense into two simple words: thank you. Thank you, Prof Sun.

Thank you to my dissertation committee—Professor Elizabeth Holm, Professor Emmanouil (Manos) Kioupakis, Professor Liang Qi, and Professor Bryan Goldsmith—for guiding me through the prelims, data meetings, and the final defense. Your advice, discussions, and support have been invaluable to my academic journey.

I am fortunate to have interacted with all my colleagues, including Joonsoo Kim, Emily Oliphant, Woohyeon Baek, Shibo Tan, Nicholas David, Gillian James, Joshua Willwerth, Abrar

Rauf, Taorui Chen, Anirudh Appachar, Chao Feng, Nina Perry, and others. It has been a pleasure discussing, learning, and creating with you. Thank you for being part of the same research group. I fondly remember the days when our office was nearly empty, with just three people and three desks, and when I was filled with worry about the research. Today, we have exciting papers and ten top-talented PhD students in the group, pushing the frontiers of computational materials science. I am proud to see how much our group has grown.

I am grateful for my collaborators, Sam Cross, Eric Wang, Matthew Powell Palm, etc. for your hard work and brilliant ideas that have contributed to our outstanding achievements.

Thanks to the senior PhD students I met at the University of Michigan, including Zihao Deng, Sicen Du, Guanglong Huang, Yiqiao Huang, Chaoming Yang, Mingfei Zhang, and others. You have all been my mentors, generously sharing your experiences in research, work, and life. You are all role models for me as I progress through my career.

Thanks to all my friends and classmates. I value each and every one of your friendships, as you have been a vital part of my PhD journey. I'm grateful for the opportunities we've had to study together, celebrate together, and support each other through homework, research, and future aspirations. Wishing you all the best.

To Ganlin Chen, Fenghe Fu, Chao Huang, Shibo Tan, Yuchen Wu, Zhucong Xi, and Zhixiong Yin: We entered the University of Michigan together five years ago, and we've experienced many ups and downs together throughout this time. It has been my pleasure to spend these moments with you. We could not go home during the COVID-19 pandemic. You all are my family in Ann Arbor. Thanks for taking care of me when I am injured, for offering advice when I am in trouble, for being happy for me when I succeed, for being angry for me when unfair things happen, and for cheering me up when I am tired. Thank you for being my friends.

Specially thanks to Bai Jiang. Thank you for lighting up when I am lost. Thank you for critiquing me when I become arrogant. Thank you for grounding me when I am anxious. Thank you for believing me when I am not. Thank you for letting me share a part of your journey. Thank you for helping me become a better version of myself.

Finally, thanks to my parents, my grandmothers, and my entire family. Thanks for believing in my decision to study abroad. Thanks for providing me with the freedom to pursue my interest without hesitation or doubt. Please forgive me for not being able to visit home frequently. If I have obtained any measure of success, it is because I am standing on top of your shoulders.

Table of Contents

List of Tables

List of Figures

Abstract

Why are certain compounds synthesizable while others are not? This question represents a fundamental inquiry in the field of solid-state chemistry. It also serves as a central focus within the realm of computational materials prediction, aligning closely with the objectives of the Materials Genome Initiative. This dissertation primarily focuses on the prediction of material synthesis with a dual-pronged approach. Firstly, it extensively explores material stability by constructing high-dimensional phase diagrams driven by fundamental thermodynamics. This process aims to generate phase diagrams for complex experimental synthesis conditions, and offers a comprehensive visual thermodynamic representation of material stability. Additionally, this dissertation delves into targeted material synthesis, utilizing high dimensional phase diagram to enhance target material stability or design efficient synthesis recipes. These approaches accelerate the realization of theoretically predicted materials and guides the process of high-throughput robotic experimental synthesis, ultimately advancing our understanding and capabilities in materials synthesis.

Phase diagrams are crucial tools for materials scientists, indicating the equilibrium phases under specific thermodynamic conditions. While most phase diagrams are two-dimensional, with axes typically representing temperature-pressure or temperature-composition, the complexity of modern materials demands consideration of additional thermodynamic factors, such as elastic, surface, electromagnetic, or electrochemical work. This expansion necessitates phase diagrams in higher dimensions ($\geqslant 3$). In our pursuit of constructing high-dimensional phase diagrams with any thermodynamic variable on its axes, we explore the duality between extensive and intensive

conjugate variables in equilibrium and non-equilibrium thermodynamics. This duality takes various forms, including distinctions between closed and open boundary conditions, relationships between Internal Energy and its Legendre transformations, and the point-line duality in convex hulls versus half-space intersections. Specifically, we derive the duality relationships for chemical work involving extensive composition variables (N) and intensive chemical potentials (μ).

Designing thermodynamic conditions to enhance or diminish the stability of a target material is a crucial task in materials engineering. For instance, during materials synthesis, the objective is often to increase the stability of a target phase relative to its precursors or competing byproduct phases. To facilitate this, we introduced a generalized Clausius-Clapeyron relation, guiding the identification of optimal directions on a high-dimensional phase diagram for stabilizing or destabilizing a target phase. Using this approach, we analyze the acid stability of manganese oxide catalysts through a 4-dimensional Pourbaix diagram with axes representing pH, redox potential, nanoparticle size, and aqueous potassium ion concentration. Additional discussions on Pourbaix diagrams with varying natural variables and in different solvents like aqueous solutions, supercritical ammonia and ethanol contribute to the broadening of Pourbaix diagram applications.

Efficient synthesis is essential for realizing predicted materials and producing complex ones. However, solid-state synthesis of multicomponent oxides often encounters challenges from undesired by-product phases, which can stall reactions kinetics. Here, we present a thermodynamic strategy to navigate high-dimensional phase diagrams, seeking precursors that avoid low-energy competing by-products and maximize reaction energy for rapid kinetics. Validating this strategy using a robotic inorganic materials synthesis laboratory, we find our predicted precursors often yield purer target materials than traditional ones. Robotic labs offer a data-driven platform for experimental synthesis science, guiding both human and robotic chemists.

Chapter 1 Materials Synthesis Guided by Thermodynamics Phase Diagrams

1.1 Challenges on bringing computational materials to life

The Materials Genome Initiative (MGI), initiated by the U.S. government in 2011, seeks to expedite the discovery, design, and deployment of new materials. Over the past few years, MGI has catalyzed transformation and innovation in materials research. Through the integration of high-throughput experimental techniques, advanced computational methods, and machine learning, researchers can rapidly screen and design materials to meet various application needs. The initiative not only accelerates the materials development cycle but also reduces costs and enhances material performance. Furthermore, MGI has fostered the development of materials data sharing and standardization. By establishing open data platforms and shared resources, researchers can more easily access and disseminate material information, accelerating global collaboration and innovation.

However, realizing the vision of MGI still faces challenges, including issues related to data quality and standardization, integration between theory and experiment, and interdisciplinary team collaboration. One of the significant challenges facing the MGI revolves around the abundance of computational materials data stored in databases, contrasted with the difficulty of experimentally synthesizing these materials, even when their structure and composition information are known. Despite advances in computational modeling and simulation techniques, which have led to the generation of vast amounts of data predicting the properties and behavior of materials, translating these predictions into real-world applications remains a formidable obstacle.

To effectively realize computational materials, it's crucial to understand the process of material formation from both thermodynamic and kinetic perspectives. This understanding provides insights into the stability, phase transitions, and reaction pathways of materials, which are essential for guiding experimental synthesis. Thermodynamics governs the stability of materials under various conditions, providing fundamental insights into the energetics of material phases and reactions. By applying thermodynamic principles, such as free energy minimization, researchers can predict the equilibrium phases of materials and identify stable configurations.[1,2,3] These predictions serve as a valuable starting point for experimental synthesis, guiding the selection of precursor materials and reaction conditions. Moreover, kinetics plays a vital role in phase transformations, nucleation, and growth processes,[4] which is crucial for controlling the morphology, structure, and properties of synthesized materials.

1.2 Mysteries of synthesis science in chemically complex materials

Chemically complex materials refer to materials composed of multiple different elements or molecules, exhibiting complex structures and properties. These materials often possess multiple functionalities or performances, and therefore find widespread applications in fields such as high-performance batteries,[5] superconductors,[6] biomedical products,[7] etc. For example, chemically complex materials such as $LiFePO_4$, demonstrate excellent electrochemical performance, enabling high energy density, long cycle life, and good safety for modern battery technology. In high-temperature superconductors, copper oxides, such as $YBa_2Cu_3O_7$,[8] and iron-based chemically complex materials, such as LaFeAsO,[9] exhibit superconductivity at low temperatures, with extremely low resistance and excellent electrical current transport properties. In medical ceramic products, chemically complex materials are commonly used in the fabrication of artificial joints and dental restorative materials, such as hydroxyapatite ($Ca_{10}(PO_4)_6(OH)_2$).[10]

Despite the remarkable capabilities exhibited by chemical complex materials, their synthesis continues to present significant challenges. These challenges arise from the necessity for precise control over the composition of chemical elements, the diversity of chemical reactions, and the lack of efficient synthesis methods. For example, traditional synthesis recipes of chemical complex materials typically entail the mixing multiple precursors together, where each precursor usually contributes to only one element. However, this process can frequently form low-energy intermediate phases, which consumes most of the reaction free energy. Consequently, the synthesis process becomes trapped in kinetic byproducts, hindering the formation of the final target product.

Synthesis science remains poorly understood, prompting researchers to rely on machine learning techniques and high-throughput experimentation for assistance. Machine learning has made significant strides in predicting materials properties,[11] optimizing synthesis parameters,[12] accelerating the discovery of novel materials,[13] and identifying novel synthesis routes.[14] Meanwhile, high-throughput robotic experimentation drives autonomous processes for materials design,[15] automated characterization,[16] and the creation of a single-source clean database.[17] However, while machine learning approaches leverage large datasets to uncover insights, they often fall short of deepening our understanding of fundamental materials science. In addition, before we better grasp the complexities of materials formation, high-throughput robotic labs primarily facilitate the trial-and-error process and consume large number of resources. Without a comprehensive understanding of the underlying mechanisms governing synthesis, rapid experimentation only provides a superficial understanding of the intricate processes involved.

Machine learning could further enhance its effectiveness in guiding materials synthesis by incorporating more robust, physically informed features. These features, rooted in fundamental thermodynamics, offer a deeper understanding of the underlying principles governing materials

formation. In this dissertation, examples can be chemical potential stability window, relative stability, inverse hull energy, etc. Similarly, high throughput experimentation could contribute to advancing science by swiftly validating hypotheses proposed from thermodynamic and kinetic principles. By rapidly testing a multitude of experimental conditions, high throughput experimentation can efficiently explore the validity of hypotheses regarding materials synthesis processes.

Unraveling the mysteries of synthesis necessitates a generalized approach that integrates advanced computational methods with thorough theoretical thermodynamic and kinetics understanding, enabling researchers to delve into the complicated processes underlying materials formation at a fundamental level.

1.3 Lack of user-specified phase diagram resources

There are various synthesis methods available today, including solid-state synthesis, sol-gel method, hydrothermal synthesis, chemical vapor deposition, electrochemical synthesis, and more. Regardless of the method chosen, researchers typically begin by consulting phase diagrams. This is because phase diagrams offer valuable insights into the thermodynamic stability of materials under specific experimental conditions. By consulting phase diagrams, researchers can identify the conditions where a material exists in a stable state or undergoes phase transitions. Since this information is crucial for determining the appropriate synthesis conditions required to fabricate the desired material, phase diagrams serve as invaluable tools for researchers in planning and executing synthesis experiments effectively.

Between 1873 and 1876, Josiah Willard Gibbs wrote three seminal papers that established the geometric foundations of equilibrium phase diagrams.[1,2,3] Today, many tens of thousands of phase diagrams have been constructed and catalogued. However, despite the enormous number of

phase diagrams now available, the variety of phase diagrams has remained relatively limited. Generally, four main types of phase diagrams are utilized: 1) Temperature–Pressure; 2) Temperature–Composition; 3) Ellingham (T, μ_{O2});[18] and 4) Pourbaix diagrams (pH, Redox potential E).[19] All four of these phase diagrams are derived from the Gibbs free energy, which has natural variables of temperature, pressure and composition. This thermodynamic potential is applicable to what Gibbs called 'simple systems'—defined to be macroscopically homogeneous, isotropic, uncharged and chemically inert; uninfluenced by gravity, electricity, distortion of the solid masses, or capillary tensions.

However, modern materials are decidedly non-simple. Today, we are becoming increasingly aware of how other forms of thermodynamic work—such as surface, [20,21,22] elastic, [23,24,25] electromagnetic, [26,27] electrochemical work, [19] etc.—influence phase stability under the complex chemical environments of modern materials devices.[28] Each additional form of work will increase the dimensionality of the free energy, by:

$$dU = TdS - PdV + \sum_i \mu_i dN_i + \gamma dA + \phi dQ + \sigma_{ijkl} d\varepsilon_{ijkl} + \vec{\boldsymbol{E}} \cdot d\vec{\boldsymbol{P}} + \vec{\boldsymbol{B}} \cdot d\vec{\boldsymbol{M}} + \ldots$$

This indicates that the relevant thermodynamic potential and phase diagram for these materials inherently exist in high-dimensional spaces. As phase diagrams are commonly two-dimensional today, we generally examine lower-dimensional slices of these multi-dimensional phase diagrams, resulting in a loss of crucial thermodynamic information. This can lead to erroneous interpretations, where certain observed metastable phases are incorrectly labeled as 'non-equilibrium' states. These phases might represent the lowest free-energy state within a higher-dimensional equilibrium phase diagram. Even if non-equilibrium phases are indeed present, a high-dimensional depiction of their free energies will offer a more comprehensive understanding of their kinetic origins.

The time has come to lift ourselves out of the Flatland of 2D phase diagrams. Urgently needed is a new theoretical framework that makes high-dimensional thermodynamics more accessible—both computationally and conceptually.

1.4 Exploratory and Targeted synthesis prediction with high dimensional phase diagrams

To tackle the challenges faced above, in this dissertation thesis, we lay a geometric foundation to construct, interpret, and navigate generalized high-dimensional phase diagrams—which can be in any dimension, with any intensive or extensive thermodynamic variables on the axes. Although this dissertation study is certainly not the first to construct phase diagrams with various forms of work on the axes,[29–34] our emphasis here is to unify the geometric underpinnings of high-dimensional thermodynamics, which from our perspective, does not have a comprehensive and detailed framework in the literature yet.

Gibbs' arguments on the convex nature of equilibrium thermodynamics only applies to phase diagrams with extensive variables as axes. Here, in **Chapter 2**, we discuss how the Legendre transformation connects to the concept of Point-Line duality from projective geometry, which enables the computation of phase diagrams with all-intensive axes or mixed intensive/extensive axes. Using composition (N) and chemical potential (μ) as example conjugate variables, we examine the dualities between closed and open thermodynamic boundary conditions, their corresponding thermodynamic potentials, and the resulting phase diagrams with axes of mixed intensive/extensive variables.[35]

When one seeks to ascertain the stability of a specific target material, it is more convenient to establish open boundary conditions around the target, allowing for extensive exchange of variable quantities with an external reservoir. This results in stability regions for single target materials in our intensive variable phase diagrams, like **Chapter 2** did. However, there are instances where the focus shifts towards determining the stability difference between a target material and an undesired phase impurity at the phase boundary. In **Chapter 3**, efforts are directed towards transforming the undesired

phase into the target material, or destabilizing the phase impurity to enhance the stability of the target. If high-dimensional phase diagrams serve as maps, then we require a 'compass' to guide us in the direction that either enhances or reduces the stability of specific phases. To develop this compass, we derive a generalized high-dimensional Clausius-Clapeyron relation. This relation simultaneously identifies the full set of experimental parameters that either stabilize or destabilize a particular phase of interest.[36]

In addition to considering single target phases and phase boundaries, our phase diagram framework works for various synthesis methods, with a particular focus on solid-state synthesis and solvothermal synthesis. This dissertation marks the first instance of incorporating particle size, ion concentration, and metal element doping into Pourbaix diagrams for aqueous solutions. Furthermore, it presents the first phase diagram aimed at guiding inorganic material synthesis in nonaqueous solvents, such as supercritical ammonia, and organic solvents like ethanol. We also explore the evolution of Pourbaix diagram development and discuss its increasing efficacy over time, culminating in our ability to manipulate solvent environments using computational methods with ease.

In my view, high-dimensional phase diagrams with various variables represent exploratory synthesis, delving into a vast array of material stability across uncharted high-dimensional parameter spaces. However, when it comes to synthesizing a specific target material, additional information is required. This includes knowledge of the optimal reactions to employ and how to prevent the formation of phase impurities during experiments. This approach is known as targeted synthesis. In Chapter IV, we propose a thermodynamic strategy for navigating the high-dimensional compositional phase diagram to pinpoint optimal reaction pathways.[37] This involves identifying precursor compositions that avoid kinetically competitive byproducts while maximizing the thermodynamic driving force for rapid reaction kinetics. To test our synthesis principles, we collaborate with a high-throughput robotic automated inorganic materials synthesis laboratory, which offers increased efficiency, reproducibility, accuracy, scalability and versatility.

[1] Gibbs, Josiah Willard. "Graphical methods in the thermodynamics of fluids." *The Collected Works of J. Willard Gibbs, Ph. D., LL. D* (1957): 1-32.

[2] Gibbs, Josiah Willard. "A method of geometrical representation of the thermodynamic properties by means of surfaces." *Transactions of Connecticut Academy of Arts and Sciences* (1873): 382-404.

[3] Gibbs, Josiah Willard. "On the equilibrium of heterogeneous substances." *American Journal of Science* 3.96 (1878): 441-458.

[4] Jackson, Kenneth A. *Kinetic processes: crystal growth, diffusion, and phase transitions in materials*. John Wiley & Sons, 2010.

[5] Zhang, Wei-Jun. "Structure and performance of LiFePO4 cathode materials: A review." *Journal of Power Sources* 196.6 (2011): 2962-2970.

[6] Tretyakov, Yurii D., and Evgenii A. Goodilin. "Chemical principles of preparation of metal-oxide superconductors." *Russian Chemical Reviews* 69.1 (2000): 1-34.

[7] Vallet-Regí, Maria. "Ceramics for medical applications." *Journal of the Chemical Society, Dalton Transactions* 2 (2001): 97-108.

[8] Beno, M. A., et al. "Structure of the single-phase high-temperature superconductor YBa2Cu3O7− δ." *Applied physics letters* 51.1 (1987): 57-59.

[9] Okada, Hironari, et al. "Superconductivity under high pressure in LaFeAsO." *Journal of the Physical Society of Japan* 77.11 (2008): 113712.

[10] Nayak, Amit Kumar. "Hydroxyapatite synthesis methodologies: an overview." *International Journal of ChemTech Research* 2.2 (2010): 903-907.

[11] Pilania, Ghanshyam, et al. "Accelerating materials property predictions using machine learning." *Scientific reports* 3.1 (2013): 2810.

[12] Huo, Haoyan, et al. "Machine-learning rationalization and prediction of solid-state synthesis conditions." *Chemistry of Materials* 34.16 (2022): 7323-7336.

[13] Liu, Yue, et al. "Materials discovery and design using machine learning." *Journal of Materiomics* 3.3 (2017): 159-177.

[14] He, Tanjin, et al. "Precursor recommendation for inorganic synthesis by machine learning materials similarity from scientific literature." *Science advances* 9.23 (2023): eadg8180.

[15] Szymanski, Nathan J., et al. "An autonomous laboratory for the accelerated synthesis of novel materials." *Nature* 624.7990 (2023): 86-91.

[16] MacLeod, Benjamin P., et al. "Flexible automation accelerates materials discovery." *Nature Materials* 21.7 (2022): 722-726.

[17] Eyke, Natalie S., Brent A. Koscher, and Klavs F. Jensen. "Toward machine learning-enhanced high-throughput experimentation." *Trends in Chemistry* 3.2 (2021): 120-132.

[18] Ellingham, Harold JT. "Reducibility of oxides and sulphides in metallurgical processes." *J. Soc. Chem. Ind* 63.5 (1944): 125-160.

[19] Pourbaix, Marcel. "Atlas of electrochemical equilibria in aqueous solutions." *NACE* (1966).

[20] Navrotsky, Alexandra. "Nanoscale effects on thermodynamics and phase equilibria in oxide systems." *ChemPhysChem* 12.12 (2011): 2207-2215.

[21] Frolov, Timofey, and Yuri Mishin. "Phases, phase equilibria, and phase rules in low-dimensional systems." *The Journal of chemical physics* 143.4 (2015).

[22] Elliott, Janet AW. "Gibbsian surface thermodynamics." *The Journal of Physical Chemistry B* 124.48 (2020): 10859-10878.

[23] Chen, Yimu, et al. "Strain engineering and epitaxial stabilization of halide perovskites." *Nature* 577.7789 (2020): 209-215.

[24] Schlom, Darrell G., et al. "A thin film approach to engineering functionality into oxides." *Journal of the American Ceramic Society* 91.8 (2008): 2429-2454.

[25] Fitzgerald, E. A., et al. "Influence of strain on semiconductor thin film epitaxy." *Journal of Vacuum Science & Technology A: Vacuum, Surfaces, and Films* 15.3 (1997): 1048-1056.

[26] Spaldin, Nicola A., and Manfred Fiebig. "The renaissance of magnetoelectric multiferroics." *Science* 309.5733 (2005): 391-392.

[27] Cheong, Sang-Wook, and Maxim Mostovoy. "Multiferroics: a magnetic twist for ferroelectricity." *Nature materials* 6.1 (2007): 13-20.

[28] Sun, Wenhao, and Matthew J. Powell-Palm. "Generalized Gibbs' Phase Rule." *arXiv preprint arXiv:2105.01337* (2021).

[29] Kaptay, George. "Nano-Calphad: extension of the Calphad method to systems with nano-phases and complexions." *Journal of materials science* 47 (2012): 8320-8335.

[30] Liu, Zi-Kui, and Yi Wang. *Computational thermodynamics of materials*. Cambridge University Press, 2016.

[31] Navrotsky, Alexandra. "Nanoscale effects on thermodynamics and phase equilibria in oxide systems." *ChemPhysChem* 12.12 (2011): 2207-2215.

[32] Xue, Fei, Yanzhou Ji, and Long-Qing Chen. "Theory of strain phase separation and strain spinodal: Applications to ferroelastic and ferroelectric systems." *Acta Materialia* 133 (2017): 147-159.

[33] Todd, Paul K., et al. "Selectivity in yttrium manganese oxide synthesis via local chemical potentials in hyperdimensional phase space." *Journal of the American Chemical Society* 143.37 (2021): 15185-15194.

[34] Voorhees, Peter W., and William C. Johnson. "The thermodynamics of elastically stressed crystals." *Solid state physics*. Vol. 59. Academic Press, 2004. 1-201.

[35] Chen, Jiadong, Matthew J. Powell-Palm, and Wenhao Sun. "The geometry of high-dimensional phase diagrams: II. The duality between closed and open chemical systems." *arXiv preprint arXiv:2404.05197* (2024).

[36] Chen, Jiadong, Matthew J. Powell-Palm, and Wenhao Sun. "The geometry of high-dimensional phase diagrams: III. Engineering relative stability in four dimensions." *arXiv preprint arXiv:2404.05201* (2024).

[37] Chen, Jiadong, et al. "Navigating phase diagram complexity to guide robotic inorganic materials synthesis." *Nature Synthesis* (2024): 1-9.

Chapter 2 The Duality Between Convex Hulls and Chemical Potential Diagrams

2.1 Duality in thermodynamics

Duality is a profound and powerful concept in mathematical physics. As described by Michael Atiyah,[1] duality gives *two different points of view of looking at the same object*. For example, a periodic function can be decomposed into a Fourier series—an infinite sum of sines and cosines; or be represented by its dual the Fourier spectrum—a vector of coefficients for each sine or cosine term. In solid-state physics, Gibbs used duality to invent the concept of the 'reciprocal lattice',[2,3] which is dual to the real-space crystalline lattice—a foundational principle in X-ray diffraction, Bloch wavefunctions, and Ewald summations. A dual representation does not produce any essentially new information, rather, it offers a new perspective to analyze and interpret a physical scenario.

In thermodynamics, there is a duality in how one can ascribe boundary conditions to a thermodynamic system. For a system containing two or more phases coexisting in equilibrium, we can either frame closed boundary conditions around this heterogeneous mixture of equilibrium phases; or if we are interested in the stability of only a single target phase, we could alternatively frame open boundary conditions around only that material, where extensive quantities (heat, volume, mass, *etc.*) are exchangeable with an external reservoir with applied intensive conditions (temperature, pressure, chemical potential, *etc.*). With closed boundary conditions, the relevant phase diagram has the corresponding extensive variable on the axis; whereas for open boundary conditions the relevant phase diagram would have an intensive variable axis. To construct the

relevant thermodynamic potential for a phase diagram with natural intensive variables, one uses the Legendre transformation, $\Phi_i = U - \Sigma_i X_i Y_i$, to change the natural variable of a thermodynamic potential from extensive in $U(X_i)$ to a new potential with the conjugate intensive natural variable, $\Phi(Y_i)$.

Gibbs' physical arguments for heterogeneous equilibrium correspond to the lower convex hulls on the Internal Energy surface, $U(S,X_i)$ of the various possible phases.[4] However, due to Gibbs' stability criterion that $\partial^2 U/\partial X_i^2 > 0$, convex hulls can only calculate heterogeneous equilibrium on thermodynamic axes of extensive variables. In many experimental contexts, the control variables are intensive, like temperature or pressure, which motivates the use of Legendre transformations from $U(S,V,N)$ to the Gibbs free energy $G(T,P,N) = U - (-PV) - TS$. In our ambition to construct generalized high-dimensional phase diagrams with any intensive or extensive thermodynamic variable on the axis, here we discuss the physical interpretation, geometric principles, and computational approaches needed to examine the duality between closed and open thermodynamic systems.

In particular, this work[5] focuses on the duality between closed and open *chemical* systems, where the extensive variable N is mass and the conjugate intensive variable μ is chemical potential. Although chemical potential diagrams have been previously made in the literature,[6-15] we believe they are underutilized, which we attribute to a lack of literature that describes how to meaningfully interpret chemical potential diagrams. First, we derive how the duality between convex hulls and half-space intersections offer a computational foundation to connect composition phase diagrams to chemical potential diagrams. We then explore how chemical potential diagrams offer a pathway to connect equilibrium thermodynamics to non-equilibrium materials kinetics—as the equations

of diffusion, nucleation, growth, and dissolution, all have terms for chemical potential in their constituent equations.

Finally, we will discuss the limitations of phase diagrams with either all composition axes or all chemical potential axes—as there are many physical scenarios where a system is closed in some elements while being open to others. We advocate for the construction of *mixed* composition-chemical potential phase diagrams, with chemical potential axes for the volatile species and composition axes for the closed species. We examine three case studies of mixed intensive-extensive phase diagrams to interpret the synthesis, operational stability, and growth of: 1) the oxynitride TaON, 2) the lithium-ion battery cathode material $LiMn_2O_4$, and 3) oxidation of the medium-entropy alloy $CrCoNiO_x$. To construct these mixed composition-chemical potential diagrams, we combine thermodynamic calculations from both convex hull and half-space intersection algorithms, and discuss the geometry of phase coexistence regions in these mixed diagrams.

More generally, our approach to duality here serves as a general blueprint to Legendre transform the $U(S,X_i)$ convex hull to any high-dimensional phase diagram, either with axes of all intensive variables (such as elastic stress, electric field, magnetic field, surface area to volume ratio, and others), or some mixture of intensive and extensive variables.

2.2 The duality between open and closed thermodynamic systems

It is not meaningful to construct or interpret phase diagrams before establishing the boundary conditions for the thermodynamic system being analyzed. For a material that can undergo chemical reactions, there are two ways to frame boundary conditions, as illustrated in **Figure 2.1**. When using the Gibbs free energy, which has a natural extensive variable of composition, one frames a ***closed*** thermodynamic system where the total composition within a

reactor is fixed. Inside these closed boundary conditions, an initial non-equilibrium set of reactants will evolve to a final equilibrium phase or a heterogeneous mixture of phases, depending on the ratio of elements in the total reaction vessel. For thermodynamic systems with many phases and chemical species, the resulting network of stoichiometrically-balanced chemical reactions can become very complicated to navigate.[16,17]

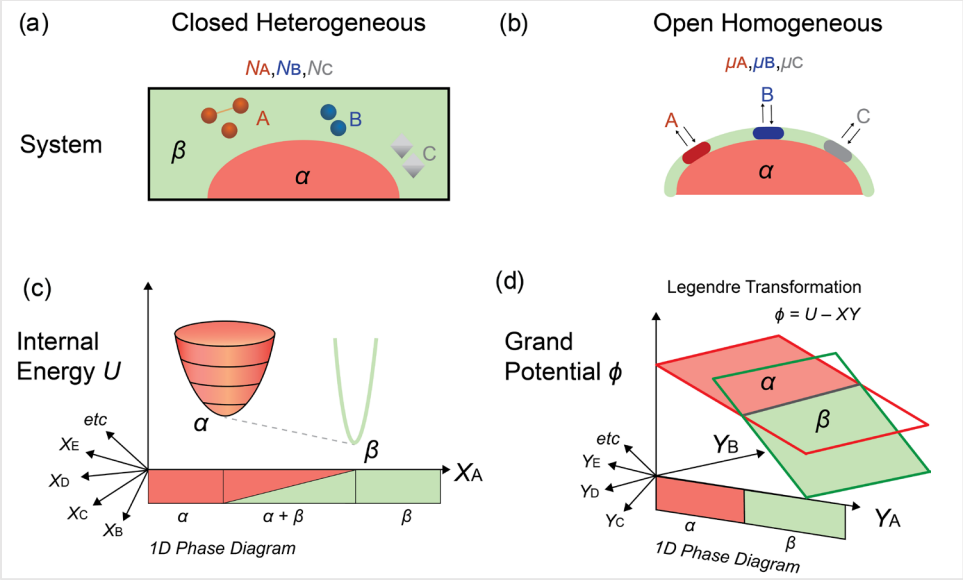

Figure 2.1: The duality between closed and open thermodynamic systems; shown in (a, b) with corresponding free energy surfaces (c,d), solved with convex hulls on extensive axes, or half-space intersections on intensive axes.

From a materials engineering perspective, our interest may instead only be with regard to a single target phase—for example, to predict optimal synthesis conditions, or to evaluate operational stability in complex chemical environments. In such cases, we may not need to (or care to) fully characterize all the possible reactions within a closed chemical system. Instead, we could frame the thermodynamic boundaries around only the material-of-interest, which we treat as open to an external chemical reservoir that has a propensity to deposit mass onto, or dissolve mass away from, our material-of-interest. The thermodynamic propensity to flux mass onto or away from the target material is given by the chemical potential difference between the reservoir and the material.

Considering a heterogeneous system in **Figure 2.2**, suppose now that Fe is in a very large but closed box filled with humid air—this air might now react with iron to spontaneously form rust and other iron (hydro) oxides. We can analyze it as a total closed system with fixed Fe and O composition, where O will exchange between air and iron. A closed heterogeneous system will evolve to equilibrium by maximizing entropy. ΔS is maximized when all intensive variables throughout a heterogeneous system are equalized. For example, in our Fe+air system, the temperatures will be the same at equilibrium, $T_{Fe} = T_{air}$. Importantly, also, $\mu_{O,solid} = \mu_{O,air}$. Likewise, the vapor pressure of Fe means a very small amount of Fe will evaporate into the air, such that $\mu_{Fe,solid} = \mu_{Fe,air}$.

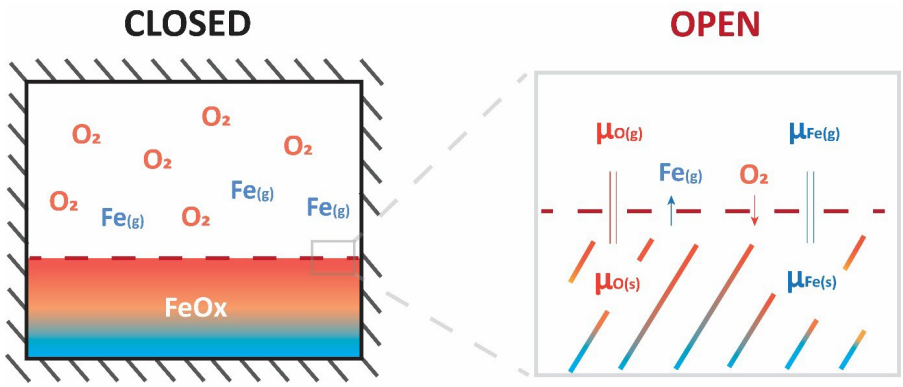

Figure 2.2: Schematic figure shows Fe solid in a closed box with humid air. O and Fe particles exchange at the interface of solid and humid air. At equilibrium, the chemical potential of O and Fe in air and solid should be the same. The dash lines around solid Fe indicate the open boundary condition. The solid lines around black box indicate closed boundary condition.

From the perspective of a material, it does not know the 'large' boundary condition of the closed system. It can only experience what is being applied at its local boundaries. In other words, while we can certainly analyze the thermodynamic equilibrium of a closed box, we can also draw an new open boundary condition around the solid Fe, and analyze as it is being acted upon by an external reservoir of air. In both cases, whether it is a closed two-phase system or a material being acted upon by an open external reservoir, the equilibrium condition is the same – the intensive variables will equilibrate at the interface.

Because there is no oxygen in Fe, there is a large driving force for oxygen to be incorporated and for Fe to transform into Fe-oxides. Fe can do work on the air by removing oxygen atoms from the air and incorporating them into its lattice. The amount of reversible work that Fe does on air is associated with a change in chemical energy; this change is the chemical potential $\mu = \partial G/\partial N$, which refers to the work required to add/remove a particle of given species.

Our choice of boundary conditions determines when we should use convex hull (extensive natural variable phase diagram) or chemical potential diagram (intensive natural variable phase diagram). It is inconvenient to analyze open systems using a closed-system phase diagram – the convex hull. For example, assuming a dope process of phosphorus airflow passing above a silicon sheet, how to control the airflow to dope the silicon into a specific phase? For silicon it has open boundary condition, and its surface changes due to applied phosphorus outside (**Figure 2.3**). At equilibrium, chemical potential of the airflow should be equal to that of phosphorus in silicon. So, a more convenient natural variable is chemical potential. The convex hull does not work here, since it does not provide much guidance on how to prepare the phosphorus flow-gas conditions. Instead, with a chemical potential diagram, airflow concentration can be directly obtained from the chemical potential of desired phase, where $\mu_p = \mu_p^o + RT ln[P]$.

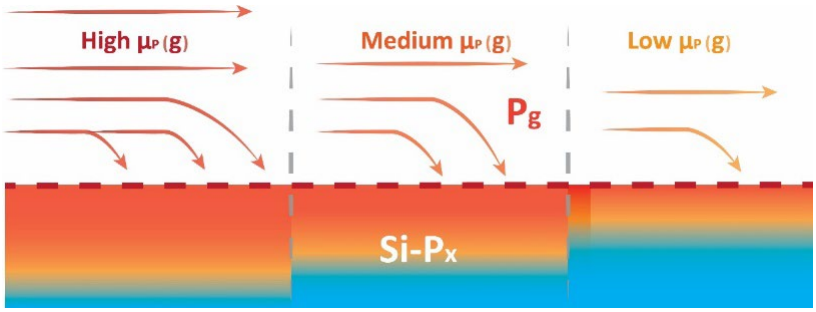

Figure 2.3: Schematic Si doping process.

A few more examples where a thermodynamic system might better be described with open instead of closed boundary conditions include the following: In gas-phase deposition, such as

chemical vapor deposition or molecular beam epitaxy, one does not usually control the composition of the volatile species; one controls partial pressure, temperature, and flow-rate, which is better described by chemical potential.[18,19] During precipitation or dissolution from an aqueous electrochemical solution, one usually cares about the material being formed or dissolved, rather than all the various chemical reactions that are possible in H_2O.[20,21] In heterogeneous solid-state systems, such as the [cathode | electrolyte | anode] system of an all-solid-state battery, one could examine heterogeneous equilibrium in the convex hull isopleth connecting the cathode and anode;[20] or equivalently one could consider the chemical potential differences at the interfaces between the various electrodes in the battery.[22] Likewise, one can make similar arguments during solid-state synthesis, as one can examine reactions with composition fixed natural variables,[15] or equivalently one could examine the chemical potential differences at the interfaces between reactants and products.[13]

The decision to either model chemical reactions in a closed heterogeneous system, or a collection of subsystems open to each other via chemical exchange, is an arbitrary decision for a human scientist. Nature will evolve the chemical system all the same—but for our conceptual benefit, we should choose our boundary conditions based on whatever considerations are convenient or important to us. To anthropomorphize the target material, it does not 'know' the composition of the reaction vessel—it will simply undergo reactions with the chemical reservoir at its physical interfaces. These reactions proceed until the chemical potentials inside the material are equivalent to the chemical potentials with the reservoir at its interface, such that equilibrium is reached.

2.3 The duality between convex hulls and half-space intersections

Chemical potential diagrams have previously been calculated, most notably by Yokokawa[6], and have been applied to study solid-oxide fuel cells,[7] hydrogen storage materials,[8] surface adsorption,[9,10,11] defects,[11,13] and materials synthesis.[13,15] In our overarching ambition to calculate high-dimensional phase diagrams, it is important to use computational phase diagram approaches that are scalable to many dimensions. A detail introduction of convex hull phase diagrams is in **Chapter 2.3.1**. Published algorithms for computing chemical potential diagrams, from our perspective, rely on inelegant approaches, often involving for loops or inefficient optimization approaches, and do not scale well to high-component chemical spaces. In addition, published chemical potential diagrams only depict equilibrium situations, while here we derive chemical potential diagrams that can represent non-equilibrium scenarios like crystal growth and dissolution.

Our derivation of the chemical potential diagram below is inspired by the discussions in Callen[23], Zia[24], and Yokokawa[6], but it is derived in a way specifically to leverage the duality between convex hulls and half-space intersections, which are computational optimization algorithms that readily scale to higher dimensions. First, we will connect the Legendre transformation to Point-Line Duality. Then we will use Point-Line Duality to connect convex hulls to half-space intersections. From our perspective, these ideas appear in the literature in scattered form, which our goal here is to unify under one physical, mathematical and computational perspective. For the sake of completeness, we present a full derivation in the **Chapter 2.3.2 – 2.3.4**. A brief summary of the derivation follows:

For phase diagrams with extensive variables, the equilibrium state is solved by convex hulls, and each state of a phase is given by a vertex on the convex hull. We then leverage a concept from projective geometry named *Point-Line Duality*. Briefly summarized: for a line of the form y

$= ax - b$, it is usually customary to treat x and y as the axes, and a and b as parameters for the line. However, since a and b provide all the information needed to define this line, we could equivalently represent this line as a point (a,b) in a–b space. Symmetrically, one can swap a,b and x,y to arrive at a similar relationship between lines in a–b space and points in x–y space. If the line is provided as an inequality, $y \leqslant ax - b$, one can show that the lower convex hull for a collection of points is equivalent to the lower half-space intersection for its dual representation of lines.

In mathematics, the Legendre transformation is a method to relate a convex function to its envelope of tangent lines. Because the tangent line to a $U(X_i)$ surface, $\partial U/\partial X_i$, gives the intensive variable Y_i; the Legendre transformation is a natural implementation of Point-Line duality. For a natural intensive variable of chemical potential, the Legendre transformation can be used to construct a new thermodynamic grand potential, $\phi = G - \mu N$. For composition axes, it is customary to transform the number of mols, N, to mol fraction, x, by the affine relationship $\Sigma_i x_i = 1$, where $x_i = N_i / \Sigma_i N_i$. This changes the intensive variable μ from the slope $\partial G/\partial N$, to the intercept rule (derivation in **Chapter 2.3.4.2**), where $\mu_i = G - (1-x_i)\cdot[dG/dx_i]$. Graphically, μ_i can be solved by a tangent line of the convex hull, extended to the vertical G axis at the elemental end-point compositions, as later illustrated in **Figure 2.8a**. Hence, the chemical potential denoted as μ in this context represents the relative chemical potential to a standard reference state. In some published papers, it is expressed as $\Delta\mu(\mu\text{-}\mu^o)$.

The $\phi(\mu)$ space is dual to the $G(x)$ space. Each phase, which was a vertex in $G(x)$ space, becomes a line in the dual $\phi(\mu)$ space. More generally, in higher dimensions, each phase becomes a hyperplane by the equation $\phi = G - \Sigma\mu_i x_i$, which corresponds directly to $y = \Sigma_i a_i x_i - b$. The equilibrium state in $G(x)$ was solved using a bounding lower-convex hull of vertices, which in dual

$\phi(\mu)$ space, corresponds to a bounding upper half-space intersection of hyperplanes. A mathematical proof of this duality is provided in **Chapter 2.3.3**.

Phase diagrams are constructed by projecting the lowest free-energy phases onto the thermodynamic axes, thus eliminating the energy axis. For example, a *T–P* phase diagram is constructed by projecting the half space intersection of $G = H + PV - TS$ onto the *T* and *P* axes. Likewise, a composition phase diagram is a projection of the $G(x)$ convex hull onto the composition axes; and a chemical potential diagram is a projection of the lower half-space envelope of ϕ surfaces onto chemical potential axes (**Figure 2.8b**). The stability region of a phase on a chemical potential diagram shows chemical potential values where its grand potential is lower than that of any other phase.

Table 2.1: Dual representation of physical aspects in closed system (the convex hull) and open system (chemical potential diagram).

Physical Aspects		**Dual Representation**	
System	**Boundary Condition**	**Closed to mass transfer**	**Open to mass transfer**
Thermodynamic Aspects	Thermodynamic Potential	Gibbs potential	Grand potential
	Euler form	$G = U + pV - TS$	$\Phi = G - \mu N$
	Differential Form	$dG = -SdT + vdP + \mu dN$	$d\Phi = -SdT + vdP - Nd\mu$
	Natural Variables	T, P, N	T, P, μ
	Heterogeneous Equilibrium	Coexistence region	Phase boundary
	Metastability	Energy above the hull	Growth
	Instability	Decomposition energy	Dissolution
Geometric aspects	Phase	Point	Hyperplane
	Equilibrium state	Convex Hull	Half-space intersection

In this work, we will present chemical potential diagrams for a variety of systems. All the thermochemical data for these diagrams are from the Materials Project database[25], which is a database of high-throughput DFT-calculated enthalpies of ordered crystalline phases. As is common in the computational materials science community, we assume that vibrational entropy is negligible in solids,

so that we can approximate $G_{solid} = E_{Solid,DFT}$[26]. The Materials Project only contains ordered crystalline phases, so we do not consider the solid-solution phases, although they are certainly relevant in real materials. Finally, DFT has known errors in formation energy[27,28], but the Materials Project has implemented a series of energetic corrections[29,30,31] which we adopt here without further scrutiny. For a thorough analysis of the actual chemical systems presented here, it would be appropriate to recalculate the thermochemical data without these assumptions—however this work primarily emphasizes the formalism, geometry and interpretation of chemical potential diagrams, so we use the unaltered Materials Project data for our visualizations.

2.3.1 The convex hull – free energy and composition phase diagram

Convex hull algorithms are commonly used in computational thermodynamics to calculate chemical equilibrium in materials systems. However, few literatures systematically introduce, explain, and interpret the convex hull phase diagrams. We begin our discussion with the thermodynamic origins of the convex hull, and why it leads to conditions of chemical equilibrium.

Gibbs establishes the stability condition of materials from two physical arguments, which leads to both the Gibbs free energy curves of single-phase compounds and heterogeneous mixtures of compounds to be convex. First, a single-phase compound can only stable against compositional self-separation if its formation energy is lower than that for any other linear combination of compositions of that phase. This results in its internal energy surface, G, being convex in the composition variable—such that $\partial^2 G/\partial^2 N > 0$. Because each pure-phase $G(N)$ surface is convex, at intermediate compositions between phases, a mixture of heterogeneous phases can also have lower total Gibbs free energy than any single homogeneous phase. This state of heterogeneous equilibrium is given by the tangent envelope that connects the bottom of $G(N)$ curves.

In **Figure 2.4**, we illustrate this convex hull for a binary system, *A–B*, with a vertical axis of *absolute* Gibbs free energy *G*, which is the sum of material internal chemical potential μ and quantity of a component *N*: $G = \Sigma \mu_i N_i$. The absolute Gibbs free energy, *G*, is extensive with respect to the quantity of each component, N_A and N_B. Each phase in *A*-*B* space is shown in **Figure 2.4** by a red arrow, and the equilibrium state would be solved by the convex envelope that wraps beneath the red arrows.

However, chemical equilibrium is usually analyzed not using absolute Gibbs free energies, but rather, by normalizing the Gibbs free energy to a per atom or per molar basis ($\bar{G}$). In **Figure 2.4a**, this can be represented by a change of basis from a G-N_A-N_B space to a G-x_B-N_{total} space, where $x_B = N_B/N_{total}$. Graphically, this operation is done by slicing the absolute convex hull along the $x_B = 1 - x_A$. Mathematically, this results in the convex hull becoming an affine hull, meaning that composition sums to one, $\Sigma x_i = 1$. For a *n* component system, this can be expressed as:

$$\overline{G} = \frac{G}{N_{total}} = \sum_{i=1}^{n} \mu_i \frac{N_i}{N_{total}} = \sum_{i=1}^{n} \mu_i x_i \qquad (1)$$

Because chemical equilibrium does not depend on N_{total}, the stability of compounds is usually analyzed in $\bar{G}$-x_B space, where *G* is normalized to N_{total} and x_A is removed, as shown in **Figure 2.4b**. Note that this reduces the dimensionality of the thermodynamic space by one.

In the *ab initio* materials design community, the free-energy of substances is usually modeled as stoichiometric line-compounds (*linearization assumption*); in other words, for pure composition materials with no off-stoichiometry. In reality, the Gibbs free energy surfaces of a phase are convex, and has a curvature of $\partial^2\bar{G}/\partial x^2 = \partial\mu/\partial x$, where chemical potential μ represents how much chemical work to add or remove an atom the further one gets away from a stoichiometric compound. This $\partial^2\bar{G}/\partial N^2$ term can be considered as *chemical capacitance*, or the capacity of a compound to store chemical work (as additional atoms); analogous to how $\partial^2\bar{G}/\partial T^2$

is the heat capacity and is the capacity of a compound to store heat. For the simplicity of expression, in the following discussion, we will use G as $\bar{G}$ - normalized Gibbs free energy per atom.

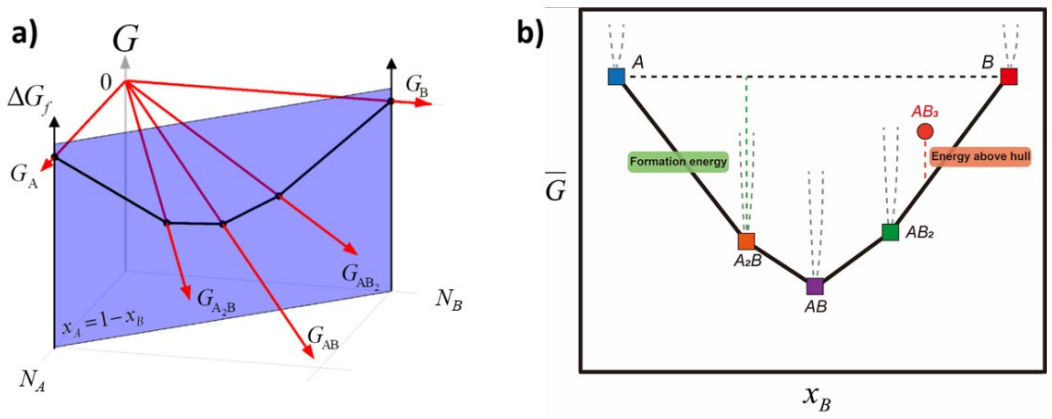

Figure 2.4: (a) A binary A-B system in G-NA-NB space. Each red arrow represents the absolute Gibbs free energy of a stable compound, which changes as NA and NB change. (b) The binary A-B system in $\bar{G}$-xB space, where G is normalized to per atom.

For example, NaCl, which is an ionic solid, would have a very high chemical capacitance $\partial^2\bar{G}/\partial x^2$, as any off-stoichiometry like $Na_{0.51}Cl_{0.49}$ would have very high electrostatic energy arising from ionic repulsion. On the other hand, a miscible metallic alloy like Au-Ag can easily become off-stoichiometric without a significant energetic penalty, and would therefore have a low chemical capacitance. For real materials, the chemical capacitance of any phase is non-zero, as shown by parabolas in **Figure 2.4b**. However, in density function theory (DFT) calculations we often assume $\partial^2\bar{G}/\partial x^2$ is infinite, which leads to a non-differentiable convex hull. One can calculate the chemical capacitance of real compounds by evaluating the energy of off-stoichiometric compositions, for example by Special Quasi-Random Structures (SQS) or lattice-based alloy cluster expansions.

The convex hull in $\bar{G}$-x space represents the equilibrium states, and materials with energy above the convex hull represent metastable phases. For example, in **Figure 2.4b**, only when a compound falls onto the convex hull, its free energy is not above linear combination between any two materials at the given composition – meaning that the compound is a thermodynamic stable

phase. In contrast, the compound AB_3 is metastable with respect to decomposing to AB_2+B; The 'energy above the hull' is a thermodynamic measurement of metastability. In a data-driven evaluation of the thermodynamic scale of metastability, we previously showed that for inorganic crystalline materials, 90% of known metastable materials are within 70 meV/atom of the hull. This metastability threshold depends on chemistry—where strongly bonding solid-state materials (nitrides, oxides) tend to have higher metastable thresholds than softly-bonding materials (tellurides, iodides); and on composition—where compounds metastable against phase-separation tend to access higher thermodynamic metastability thresholds than polymorphic compounds. Importantly, not all materials with a low energy above the hull are necessarily synthesizable, although the specific synthesizability criteria for metastable materials is not precisely understood today.

2.3.2 The Legendre Transformation and Point-Line Duality

There is a duality between a convex curve and its envelope of tangent planes. In projective geometry, this duality is called *Point-Line Duality*, where the convex curve is referred to as the 'primal' surface, and the envelope of tangent planes is the 'dual' surface. This dual surface encodes the inclination of the tangent planes for the Internal Energy surface—in other words, it redefines the conjugate intensive variable as the natural variable. This process is performed by the Legendre transformation, which defines a new thermodynamic potential Φ, by a change in natural variable from an extensive variable X to intensive variable Y. The general expression can be written as: $\Phi = U - XY$, where $Y = \partial U/\partial X$. For example, the Helmholtz potential, $F(T,V) = U - TS$, replaces the extensive variable S with its intensive conjugate T, and the Gibbs potential, $G(T,P) = U + PV - TS$, further replaces volume with pressure.

In **Figure 2.5**, we illustrate a transformation of the Internal Energy $U(S)$ to the Helmholtz free energy $F(T)$. If a thermodynamic system is in contact with an external temperature reservoir, then when the system reaches equilibrium with the external reservoir, U should be minimized *under a constraint* where the externally applied temperature is some T_1. This is shown as a tangent line with slope as $\partial U/\partial S = T_1$, as illustrated by the red line in **Figure 2.5a**. A new thermodynamic condition is then defined through Legendre transformation, $F(T_1) = U_1 - (\partial U / \partial S)_{T_1} S_1$.

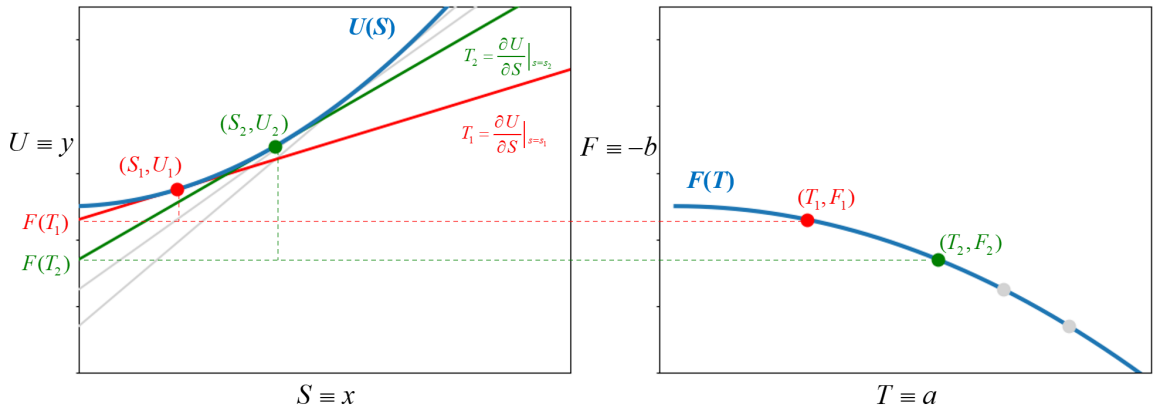

Figure 2.5: Schemtic relationship between (a) U and S, (b) F and T, at fixed volume for homogenous phases. [S, U] and [T, F] are dual spaces and the two blue curves are duality of each other.

On **Figure 2.5a**, $F(T_1)$ corresponds to the point at $S = 0$. In other words, $F(T_1)$ is the y-intercept of the tangent line to $U(S)$ at the point where $\partial U/\partial S = T_1$. More generally speaking, $F(T) = U - (\partial U/\partial S)S = U - TS$, which encodes the information of $U(S)$, but without a dependence on S. The natural variable of F is now T, and the differential form is $dF = -SdT$.

If we traverse all points on the $U(S)$ curve with different values of $T = \partial U/\partial S$, we can trace out the $F(T)$ curve which is shown in **Figure 2.5b**. Based on the stability criterion for homogenous phases, U is *convex up* with respect to extensive variables, so $\partial^2 U/\partial S^2 > 0$. Because $\partial^2 U/\partial S^2 = T/c_v$, where c_v is the heat capacity at constant volume, this stability criterion implies that heat capacity for a self-stable phase must be positive. If we trace F with respect to T, we notice the curve is

concave, $\partial^2 F/\partial T^2 < 0$. This negative curvature in $F(T)$ is also a consequence of the positive heat capacity of materials.

Point-Line Duality leverages the duality between a line $y = ax - b$ in primal $[x, y]$ space, to a point (a, b) in dual $[a, b]$ space. In thermodynamics, from **Figure 2.5**, we can reformulate the tangent line to $U(S)$ as: $y = ax - b \rightarrow U = TS + F$. Here, the correspondence is $U \equiv y$, $T \equiv a$, $S \equiv x$, and $F \equiv -b$; meaning that $[U, S]$ and $[-F, T]$ are dual spaces. Since $-F$ and F show one-to-one correspondence, we can also say that $[U, S]$ and $[F, T]$ spaces are dual with each other. In **Figure 2.5**, for each line on the $U(S)$ curve, we can draw its dual point in $[F, T]$ space, shown by the green and red lines in $[U, S]$ space and points in $[F, T]$ space. In this sense, the blue convex $U(S)$ curve is dual to its corresponding concave $F(T)$ curve.

Table 2.2: Table of the Point-Line duality between primal $[x, y]$ space and dual $[a, b]$ space.

	Primal	**Dual**
2 dimensional	$[x, y]$	$[a, b]$
N-dimensional	$[x_1, x_2, \ldots, x_{n-1}, y]$	$[a_1, \ldots, a_{n-1}, b]$
	Point	**Hyperplane**
2 dimensional	(x, y)	$b = xa - y$
N-dimensional	$(x_1, x_2, \ldots, x_{n-1}, y)$	$b = \sum_{i=1}^{d-1} x_i a_i - y$

In higher dimensions $d > 2$, the corresponding notion is *Point-Hyperplane duality*, where a hyperplane is defined as a d–1 dimensional subspace which splits a space into two half-spaces. The hyperplane can be defined in the primal $[x, y]$ space as $y = \sum_{i=1}^{d-1} a_i x_i - b$, while the corresponding point in the dual $[a, b]$ space is $(a_1, \ldots, a_{n-1}, b)$. The above discussion is generalized in **Table 2.2**, which gives the corresponding relationships between points and lines in different dual spaces. In thermodynamics, we should treat the primal space in its multidimensional form of

$U(S, X_1, \ldots, X_i)$, with the energy scalar U as the y-axis, and the various extensive variables as corresponding to the x_i terms.

2.3.3 Mathematical derivation of duality

From a materials thermodynamics standpoint, Point-Line Duality holds particular significance as it is related to the duality between G-x convex hulls and their corresponding half-space intersections, which are Φ-μ chemical potential diagrams. As a definition of half-space intersection: a line in a plane separates the plane into two sections, each of which is called a half-plane; in higher dimensions, the notion is half-space. Half-space intersections forms an inner envelope. Here, we provide a mathematical derivation of this duality relationship, and show its relevance to thermodynamic phase diagrams, which proves the duality between the composition vs. chemical potential phase diagrams.

Consider a set of points, P, in primal space. As shown in **Figure 2.6**, a point $p \in P$ is a vertex of a lower convex hull, $\mathcal{LH}(P)$, if and only if there is a non-vertical line l passing through p such that all other points of P lie above l. Correspondingly, in dual space, represented by an asterisk, the line segment $p^* \in P^*$ is a part of the lower envelope ($\mathcal{LE}(P^*)$ half-space hyperplanes), if and only if there is a point l^* on the line p^* such that l^* lies below all other lines of P^*.

These arguments generalize to N-dimensional spaces, where for a N-dimensional point $p \in P$ to be a vertex of an N-dimensional lower convex hull, there must be a non-vertical hyperplane l, passing through p such that all other points of P lie above l. The dual statement is that for a hyperplane $p^* \in P^*$ to be a part of a lower envelope, there is a point l^* on the plane p^*, such that l^* lies below all other lines of P^*. In projective geometry, $[x, y]$ and $[a, b]$ are dual to one another,

but in thermodynamics [U, S] and [$-F$, T] are dual to one another, meaning that the lower envelope from projective geometry becomes an upper envelope when applied to thermodynamics.

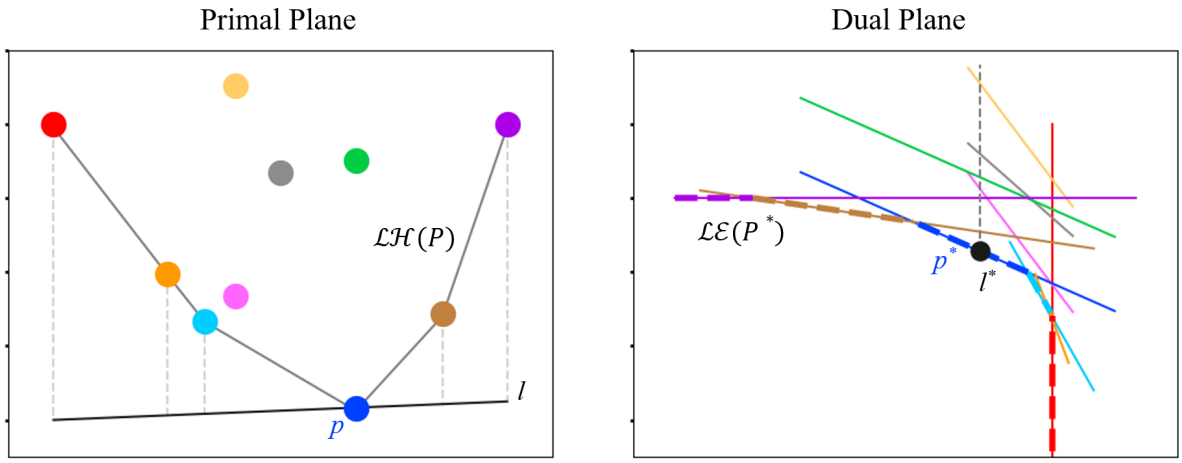

Figure 2.6: The duality between a lower convex hull and a lower envelope. Colors of points in the primal space correspond to their lines in the dual space.

Similarly, in this study, a set of points in the convex hull G-x primal space, are represented by a set of hyperplanes in the chemical potential diagram ϕ-μ space, forming the half-space intersections. In the same way that $F(T)$ is a Legendre transformation of $U(S)$, and therefore is its dual, we can perform a similar Legendre transformation from $G(x)$ to the grand potential, $\phi(\mu)$. At constant temperature and pressure, this can be defined as:

$$\overline{G}\left(T,P,x_1,x_2...x_n\right)\xrightarrow{LT}\overline{\phi}\left(T,P,\mu_1,\mu_2...\mu_n\right)$$

$$\phi = G-\sum_{i=1}^{n}\frac{\partial\overline{G}}{\partial x_i}x_i = G-\sum_{i=1}^{n}\mu_i x_i$$

For each phase, which is given by a vertex in G-x_1-x_2 space, its corresponding Grand free energy is given by $\phi = G - \sum_{i=1}^{n}\mu_i x_i$. Taking a binary Mn-O system as an example, this Grand free energy is written as $\phi = G - \mu_{\mathrm{Mn}}x_{\mathrm{Mn}} - \mu_{\mathrm{O}}x_{\mathrm{O}}$. Although the binary convex hull can be fully represented with either x_{Mn} or x_{O}, as $x_{\mathrm{Mn}} = 1 - x_{\mathrm{O}}$, for a duality analysis we can include the

redundant x_2 information. Therefore, a point in [x_{Mn}, x_O, $\bar{G}$] space corresponds to a 2-D hyperplane in [μ_{Mn}, μ_O, $\bar{\phi}$] space.

Based on the way $\bar{\phi}$ is defined, a phase p on the Mn-O convex hull can be represented by the plane equation p^* as $\bar{\phi} = \bar{G}^p - \mu_{Mn}x_{Mn}^p - \mu_O x_O^p$, where x_O^p, x_{Mn}^p, $\bar{G}^p$ represents composition of oxygen, manganese, and Gibbs formation free energy per atom of Mn_3O_4. Then, because e^* is a point on the plane p^*, we have $\bar{\phi}^* = \bar{G}^p - \mu_{Mn}^* x_{Mn}^p - \mu_O^* x_O^p$. In **Figure 2.7 left**, for a plane Mn_3O_4 $p^* \in P^*$ to be a part of a lower envelope in [μ_{Mn}, μ_O, $\bar{\phi}$] space, there is a point $e^* = (\mu_{Mn}^*, \mu_O^*, \bar{\phi}^*)$ on the plane p^*, such that e^* lies below all other planes of P^*. In other words, for any plane $j^* \in \{i \mid i \in P^*, i \neq p^*\}$, where j* is $\bar{\phi} = \bar{G}^j - \mu_{Mn}x_{Mn}^j - \mu_O x_O^j$, $\bar{\phi}^*$ should be no greater than the corresponding $\bar{\phi}^j$ value at μ_{Mn}^*, μ_O^* on the plane j^*. Mathematically, this means at μ_{Mn}^*, μ_O^*:

$$\overline{\phi^*} \leq \overline{\phi^j}$$

Therefore, if equation above is true, there exists a point e^* on the plane p^* such that the e^* is below any other plane j^*. This means p^* is on the lower half-space intersection envelope.

For a point $e^* = (\mu_{Mn}^*, \mu_O^*, \bar{\phi}^*)$ on plane p^* in [μ_{Mn}, μ_O, $\bar{\phi}$] space, its dual plane e in [x_{Mn}, x_O, $\bar{G}$] space is $\bar{G} = \bar{\phi}^* + \mu_{Mn}^* x_{Mn} + \mu_O^* x_O$, as shown as the light blue triangle in **Figure 2.7 right**. Every points on this plane has same chemical potentials. Then the dual of p^* is $p = (x_{Mn}^p, x_O^p, \bar{G}^p)$, which is material Mn_3O_4. If p is a vertex on the convex hull, there is a plane e passing through p, and below all other vertices from P (all other materials). This means for any point $j \in \{i \mid i \in P, i \neq p\}$, where $j = (x_{Mn}^j, x_O^j, \bar{G}^j)$, $\bar{G}^j$ should be greater than the corresponding $\bar{G}^e$ value on the plane e at x_{Mn}^j, x_O^j, as shown as the red point on the convex hull of left figure. Mathematically, this means at x_{Mn}^j, x_O^j:

$$\overline{G^e} \leq \overline{G^j}$$

Since $\bar{G}^e = \bar{\phi}^* + \mu_{Mn}^* x_{Mn}^j + \mu_O^* x_O^j$, we can substitute $\bar{G}^e$ and rearrange the inequality as:

$$\overline{\phi^*} \leq \overline{G^j} - \mu_{Mn}^* x_{Mn}^j - \mu_O^* x_O^j$$

Here, the right-hand side is $\bar{\phi}^j$ at $\mu_{Mn}{}^*$, $\mu_O{}^*$. So, the inequality is equal at $\mu_{Mn}{}^*$, $\mu_O{}^*$ to

$$\overline{\phi^*} \leq \overline{\phi^j}$$

If equation above is true, then there is a plane e passing through p and below all other points, which means p is a vertex on the convex hull. Eq. 1 and Eq. 2 are as same as each other, which proves that a convex hull in [x_{Mn}, x_O, $\bar{G}$] space and the chemical potential diagram [μ_{Mn}, μ_O, $\bar{\phi}$] space is dual to one another.

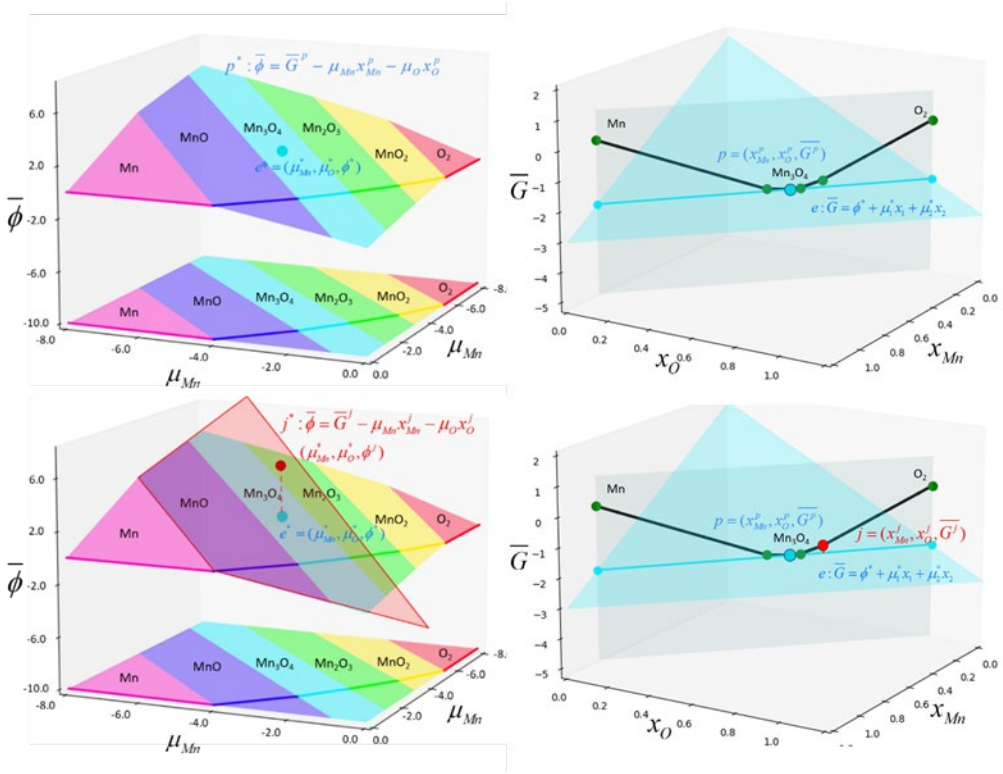

Figure 2.7: Left) Mathematical description of half-space intersection in chemical potential diagram. Right) Mathematical description of convex hull in formation energy and composition phase diagram.

2.3.4 Computation of chemical potential diagrams

2.3.4.1 Linearization assumption

In **Figure 2.5**, we illustrated the duality between a convex envelope of tangent lines to $U(S)$ and a concave set of points to $F(T)$ for a single phase. To construct a phase diagram, one calculates phase transitions between multiple phases. In the computational DFT community, we often calculate the phase transition boundary between multiple phases as if single phases have infinite curvature in the extensive variables, as shown in **Figure 2.5b**. For example, if you are calculating temperature-dependent phase transitions using $G(T)$, for each single phase, we linearize $G(T)$, where $G = H - TS$, by treating S as a constant. This linearization assumes a zero curvature for $\partial^2 G/\partial T^2 = C_p/T$; in other words, we are assuming that the heat capacity is zero. Then, each phase is a vertical line in $G(S)$ space, because S is a constant and G is affected by T. A vertical line means the second derivative of thermodynamic potential with respect to S is infinite.

Note that linearizing the thermodynamic potential in intensive variables means that conjugate extensive variables are assumed constant, and the second derivative with respect to intensive variables of a phase is zero. The reflection of this linearization in the conjugated extensive variables is that the second derivatives with respect to them are infinite.

When calculating chemical potential diagrams, we can also linearize $\phi(\mu)$, where $\phi = G - \mu x$, such that x is a constant. Therefore, the second derivative of ϕ with respect to μ is zero. Chemically speaking, a constant x means that we are considering only stoichiometric phases—no off-stoichiometry for a phase is favorable due to a very large energy increase. This linearization assumption also corresponds to the nature of solid-state DFT calculations, since DFT calculations are typically performed on stoichiometric compounds, and it can be laborious to evaluate the energy at off-stoichiometric, disordered compositions.

Linearization produces good approximations of phase boundaries in thermodynamics, and makes calculations faster, while still retaining interpretability. If we truly need to calculate a solution phase, we can include a series of vertices to represent a continuous $G(x)$ curve in the composition axis. Most importantly, linearization also enables the use of computational codes that calculate the half-space intersection. We will discuss this in the following sections.

2.3.4.2 Computation of chemical potential diagrams through the Intercept Rule

Here, we briefly derive the Intercept Rule in a 2-component system. The affine constraint in a binary space is $x_A = 1 - x_B$. This constraint eliminates a degree-of-freedom, and therefore, a dimension from the chemical space; from G-N_A-N_B to $\bar{G}$-x_B. Here, $\bar{G} = \mu_A x_A + \mu_B x_B$, so that $d\bar{G} = \mu_A dx_A + \mu_B dx_B$. By substituting the affine relationship of the convex hull where $dx_A = -dx_B$, we can derive: $\bar{G} = \mu_A + (\mu_B - \mu_A)\, x_B$, $d\bar{G} = (\mu_B - \mu_A)\, dx_B$. By substituting $(\mu_B - \mu_A)$ with $d\bar{G}/dx_B$, we can get the chemical potential of A or B as: $\mu_B = G(x_B) + (1-x_B)[\partial G(x_B)/dx_B]$, and $\mu_A = G(x_B) - (x_B)[\partial G(x_B)/dx_B]$. Geometrically speaking, this places μ_A and μ_B directly on the $\bar{G}$-intercepts of the tangent plane to the convex hull where the x_B is either 0 and 1, respectively. The chemical potential then has the same magnitude and units of the formation energy. In other words, the intercept of the tangent line for a phase with the $\bar{G}$-axis provides the chemical potential of each specie in the material at equilibrium.

Additionally, the intercept rule serves as way to demonstrate the duality between the convex hulls and chemical potential diagrams. However, calculation of intercepts require the computation of gradients or normal vectors of phase coexistence regions (tangent planes). This process is computationally expensive when the chemical potential diagram involves more than two components. An alternative, more efficient approach is to calculate the half-space intersection of the convex hull, as it offers greater ease of scalability to higher dimensions.

2.3.4.3 Computation of chemical potential diagrams through half-space intersection

Phase diagram with all chemical potential axes

Half-space intersections offer an easy and scalable approach to construct chemical potential diagrams. First, we define the grand potential for each phase using $\phi = G - \Sigma\mu_i x_i$, then we construct a half-space intersection. The implementation python codes and tutorial examples are in Github link: https://github.com/dd-debug/chemical_potential_diagram_and_convex_hull_and_pourbaix_diagram

We utilize the *HalfspaceIntersection* class from *scipy* to get the dual of points from each single phase from the convex hull. To use the *HalfspaceIntersection*, we need to prepare the coefficients in a form of $A\mathbf{x} + B \leq 0$, where A and B are each a coefficients matrix, and $\mathbf{x}$ is variables matrix. Matrix below shows the corresponding matrix form in our study. Each single phase corresponds to one row of A and B coefficient matrix, formed by composition x_i and formation energy G. Each row defines a hyperplane in the ϕ-μ_i space. This is why the Linearization assumption is necessary, because it ensures each single phase has stoichiometric composition to fulfill the input requirements of *HalfspaceIntersection* class.

Therefore, each phase is a flat hyperplane in ϕ-μ space. All these hyperplanes then form a half-space intersection – which produces a lower inner envelope, which produces whatever phase has the lowest free energy ϕ at a specific set of applied chemical potentials.

$$AX + B \leq 0$$

$$\begin{bmatrix} (x_1 & x_2 & \dots & x_N & 1)_\alpha \\ (x_1 & x_2 & \dots & x_N & 1)_\beta \\ & \dots & & & \end{bmatrix} \begin{bmatrix} \mu_1 \\ \mu_2 \\ \dots \\ \mu_N \\ \phi \end{bmatrix} + \begin{bmatrix} -G_\alpha \\ -G_\beta \\ \dots \end{bmatrix} \leq 0$$

HalfspaceIntersection constructs a fully enclosed polytope, and so we also need border hyperplanes and an internal point to define the region to enclose by half-space intersection. Border

hyperplanes are constructed based on the boundary limits of the chemical potential as we choose, which ensures that the half-space is enclosed. Then, the half-space intersection can be calculated. Next, using the *intersection* attribute from the *HalfspaceIntersection* class, we obtain the domain information of single-phase and phase-coexistence regions, and chemical potential diagrams are ready to plot.

Equilibrium envelope

The chemical potential diagrams generated in this study include scenarios of both equilibrium and non-equilibrium conditions. To the best of our knowledge, this is the first time that this complete chemical potential diagram is reported, which also shows the growth and dissolution chemical potential ranges of each phase. Existing chemical potential diagrams in the literature are exclusively confined to equilibrium conditions, constituting a specific subset of the complete chemical potential diagram, where $\phi = [G]_{internal} - [\Sigma_i \mu_i x_i]_{external} = 0$, signifying the equivalence of external applied chemical potential to the internal chemical potential at equilibrium. We called this equilibrium version of chemical potential diagram as the *equilibrium envelope*.

Following the same procedure, we can also use *halfspaceintersection* Class to construct the equilibrium envelope, by removing ϕ variable and its coefficient, because $\phi = 0$. This can be expressed as:

$$AX + B \leq 0$$

$$\begin{bmatrix} (x_1 & x_2 & \dots & x_N)_\alpha \\ (x_1 & x_2 & \dots & x_N)_\beta \\ & \dots & & \end{bmatrix} \begin{bmatrix} \mu_1 \\ \mu_2 \\ \dots \\ \mu_N \end{bmatrix} + \begin{bmatrix} -G_\alpha \\ -G_\beta \\ \dots \end{bmatrix} \leq 0$$

2.4 Equilibrium and non-equilibrium regions on a chemical potential diagram

When analyzing the stability of a material under open boundary conditions, one should distinguish in the mind between the *internal* intensive variable of a substance, Y_i, versus the *external* intensive variable of the reservoir $Y_{external}$. If the $Y_{internal} \neq Y_{external}$, then the conjugate extensive quantity X will flow through the boundary until $Y_{internal} = Y_{external}$, after which entropy will be maximized and equilibrium is reached. For example, if 50°C water is exposed to an external temperature reservoir of 10°C, heat will flow out of water into the reservoir, and the entropy of water will be reduced correspondingly. Water has a continuous span of entropies in this temperature range, so it can change its *internal* extensive entropic state to equilibrate with an *external* intensive temperature reservoir.

Likewise, for chemical work, to equilibrate the internal chemical potential of a material with the external chemical potential of the reservoir, mass can be transferred across the boundaries. At **equilibrium**, the externally applied chemical potential reservoir will be exactly equal to the internal chemical potential of a material; $\mu_{material} = \mu_{reservoir}$, such that there is no driving force to transfer mass to or from the reservoir. For a ***non-equilibrium*** situation, if external chemical potentials are different than the internal chemical potentials of a material, mass will have a propensity to flux from high μ to low μ; where a material will grow if $\mu_{reservoir} > \mu_{material}$, or it will dissolve or corrode if $\mu_{reservoir} < \mu_{material}$. Because growth and dissolution are fundamental aspects of materials kinetics, chemical potential diagrams offer a direct link between non-equilibrium thermodynamics and kinetics of transport.

The internal chemical potential of the material derives from the energies of its quantum-chemical and electrostatic bonds—which determines its scalar formation energy. **Figure 2.8a** visualizes the formation energies of phases from the Mn-O system with its interpretation for equilibrium and non-equilibrium scenarios from the perspective of a convex hull. The corresponding chemical potentials can be interpreted from the intercept rule—where μ_{Mn} or μ_O are the intercept of the tangent lines of the convex hull with the vertical energy axis at the elemental end-point compositions.

The equilibrium chemical potential window of the single phase Mn_3O_4 is bound between the cotangent lines of Mn_2O_3/Mn_3O_4 and Mn_3O_4/MnO, where these cotangent lines indicate the chemical potentials where Mn_3O_4 can coexist in equilibrium with Mn_2O_3 or Mn_3O_4. **Figure 2.8b** shows the corresponding chemical potential windows of each Mn_xO_y phase, indicated by the vertical line segments at a given composition. Because phases on the convex hull are points, the Legendre transformation of these phases form the grand potential surfaces, whose half-space intersection is shown **Figure 2.8d**. The condition where the *externally* applied chemical potentials are equal to the *internal* chemical potential of a material can be written as:

$$\phi = [G]_{internal} - [\Sigma_i \mu_i x_i]_{external} = 0.$$

Therefore, the conditions of equilibrium on a chemical potential diagram correspond to a *slice* of grand potential surfaces where $\bar{\phi} = 0$, accentuated by the darker lines on **Figure 2.8 d**. We call this the *equilibrium envelope* of the chemical potential diagram. All regions in chemical potential diagrams display the external chemical potential applied by the reservoir, but darker lines additionally represent the situation where *internal* chemical potential of each material on the convex hull is equal to the external chemical potential from the reservoir. The lines formed by the equilibrium envelope ($\phi = 0$) are consistent with the vertical segments formed by intercept rule as illustrated in **Figure 2.8b**.

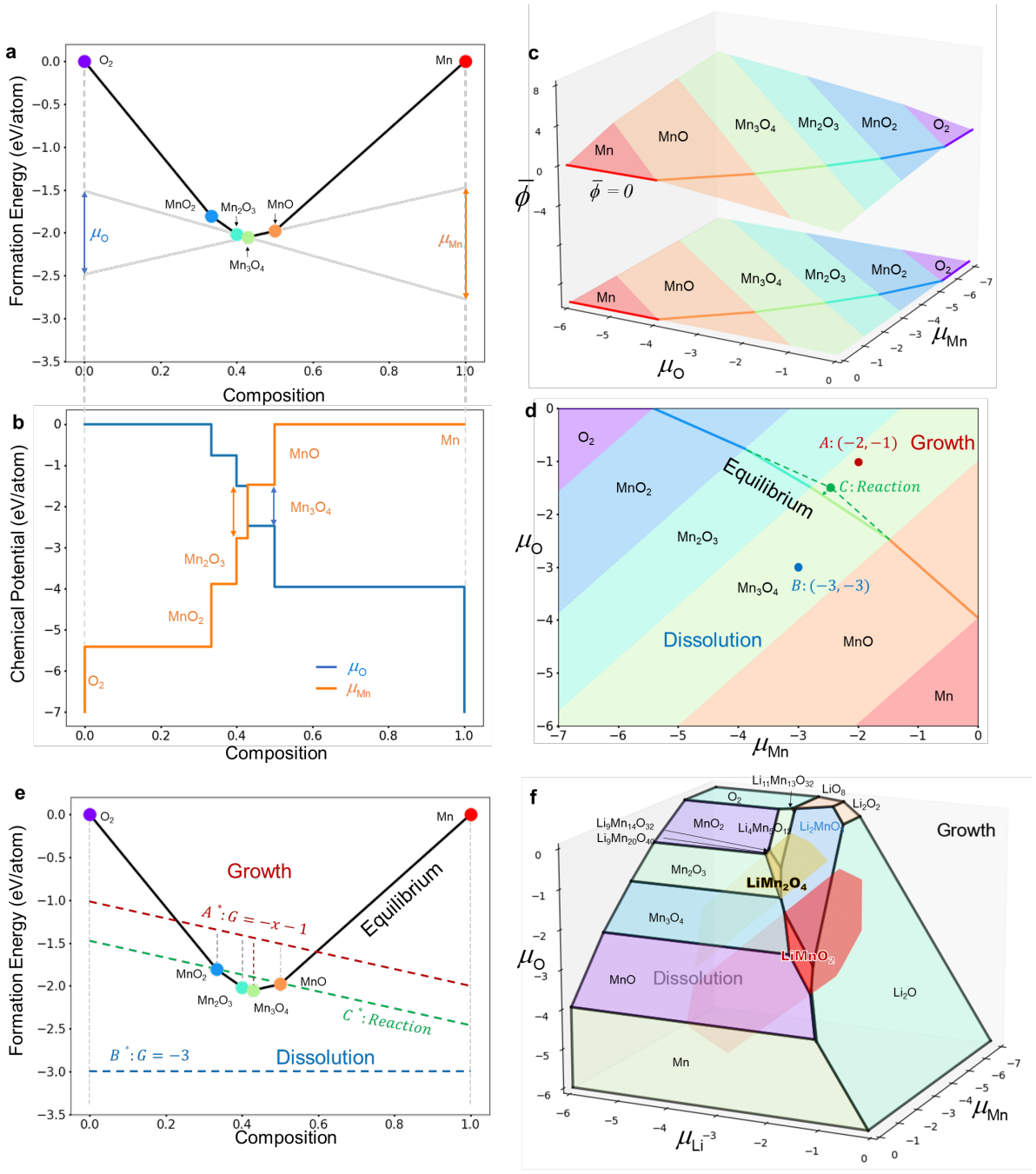

Figure 2.8: Duality between convex hulls and chemical potential diagrams in the binary Mn-O system. (**a**) Tangent lines to the convex hull, and their intercepts with the energy axes, show the elemental chemical potential window for Mn_3O_4. (b) Chemical potential windows for μ_{Mn} and μ_O various MnO_x phases indicated by vertical segments. (c) Grand potential hyperplanes for the Mn-O chemical potential diagram. The equilibrium envelope is emphasized by a dark line at $\phi = 0$ (d) Dissolution and growth regimes on the chemical potential diagram and (e) their dual relationship with the convex hull. (f) Ternary chemical potential diagram, with the growth and dissolution regimes for $LiMn_2O_4$ and $LiMnO_2$ illustrated as extending in and out of the stability regions on the equilibrium envelope.

The equilibrium envelope further separates a chemical potential diagram into non-equilibrium regions of growth and dissolution. For example suppose Mn_3O_4 is placed in contact with an external chemical reservoir where the boundary conditions are $(\mu_{Mn}, \mu_O)_{external} = (-2, -1)$, indicated by the red label A in **Figure 2.8d**. These chemical potentials are higher than the internal μ_{Mn} and μ_O in Mn_3O_4, so Mn and O will flux from the external chemical reservoir onto Mn_3O_4, leading to crystal growth. On the convex hull in **Figure 2.8e**, the dual representation to this point on the chemical potential diagram corresponds to the line A^* on the convex hull. Likewise, if Mn_3O_4 is exposed to low $(\mu_{Mn}, \mu_O)_{external} = (-3, -3)$, shown as point B in **Figure 2.8d** and the line B* in **Figure 2.8e**, Mn and O will flux out of Mn_3O_4 into the reservoir, leading to dissolution of Mn_3O_4. The precise chemical or structural nature of the external chemical reservoirs are irrelevant, only their μ_{Mn} and μ_O chemical potentials matters.

The chemical potential diagram can also show conditions for solid-solid phase transformation from a metastable solid to an equilibrium phase. If a different MnO_x phase, for example Mn_2O_3, were exposed to an external chemical potential such as point A or B, which is in the non-equilibrium region corresponding to Mn_3O_4, there would first be a thermodynamic driving force for phase transformation from Mn_2O_3 to Mn_3O_4, followed by subsequent growth or dissolution of Mn_3O_4. In the convex hull of **Figure 2.8e**, the phase transformation that originates from Mn_3O_4 has the largest energy drop from line A* compared to all other MnO_x phases. Nucleation and diffusion kinetics aside, the bulk driving force preferences the transformation and further growth of Mn_3O_4. Additionally, because Mn_3O_4 has the shallowest energy drop to B*, any other MnO_x composition exposed to this external chemical reservoir can first reduce its free energy by transforming to Mn_3O_4, and then dissolving mass out to the reservoir.

Additionally, chemical potential diagrams can be employed to illustrate solid-state reactions. In **Figure 2.8e**, the green dashed line, denoted as C*, represents the reaction between MnO_2 and MnO. By Point-Line duality, this corresponds to point C in the chemical potential diagram (**Figure 2.8d**), which is the intersect between the extension of the equilibrium envelope lines for MnO_2 and MnO. The reaction driving force is the distance from point C to the Mn_3O_4 equilibrium envelope along the

μ_O: μ_{Mn} = 1 direction. This reaction energy on the chemical potential diagram is equal to the distance between C* and Mn_3O_4 on the convex hull.

Our geometric interpretation of the binary convex hull and chemical potential diagram can be readily extended to higher component systems. **Figure 2.8f** illustrates a ternary μ_{Li}-μ_{Mn}-μ_O chemical potential diagram. The chemical potential diagram exists in 3 dimensions, since one can vary all three chemical potentials independently for non-equilibrium scenarios. However, the equilibrium envelope is still a 2-dimensional manifold, due to the special constraint that $\bar{\phi} = [G]_{internal} - [\Sigma_i x_i \mu_i]_{external} = 0$. Nonetheless, one can see that the non-equilibrium regions similarly extend into and out of the equilibrium manifold, for example as highlighted for $LiMn_2O_4$ (yellow) and $LiMnO_2$ (red). All other arguments of growth and dissolution can be applied to this ternary chemical potential diagram.

2.5 Mixed Composition-Chemical Potential Diagrams

There are many physical situations where a chemical system is open to some elements, but are closed in others. For example, in the stability of metal oxynitrides, oxygen and nitrogen can be volatile, whereas the metal(s) usually are not. In such cases, pure chemical potential diagrams or pure compositional phase diagrams may not be the most useful. Here we advocate for the construction of mixed composition and chemical potential phase diagrams, interpreting three representative case studies for oxynitride stability, lithium-ion cathode stability, and oxidation of multicomponent alloys.

Although mixed composition-chemical potential diagrams can be interpreted from the geometry of the intercept rule, they are not straightforward to calculate, as they require using convex hulls in the composition axes, and then half-space intersections for the chemical potential axes. We present a method where equilibrium is calculated both with convex hulls and half-space intersections, then the coordinates of each phase are mixed-and-matched depending on if the

desired axis is composition or chemical potential. Details of this computational implementation are discussed in **Chapter 2.5.4**.

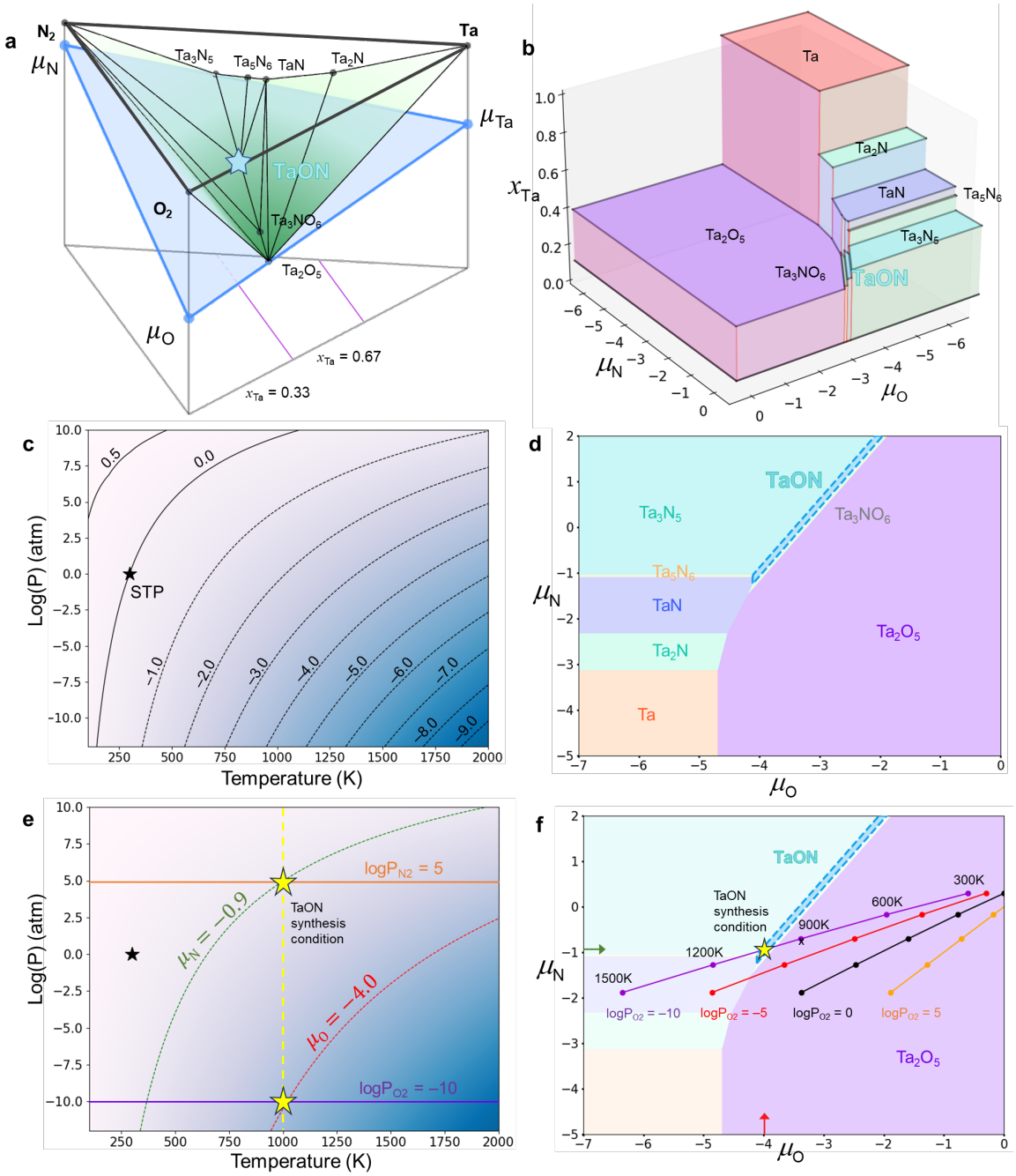

Figure 2.9: **a**) Ternary x_{Ta}-x_N-x_O convex hull. Blue triangle represents tangent plane to the TaON vertex, whose intercepts with the energy axis provides the corresponding elemental chemical potentials. **b**) Mixed x_{Ta}-μ_O-μ_N phase diagram. **c**) The chemical potential of a diatomic gas like O_2 or N_2, as a function of temperature and partial pressure. Iso-μ lines are marked from -9 to 0.5 eV/atom. **d)** μ_O-μ_N projection of the mixed x_{Ta}-μ_O-μ_N diagram. **e**) Gas conditions for N_2 and O_2 where TaON is stable, marked with yellow star. **f**) Lines on the μ_O-μ_N projected diagram corresponding to gases at various partial pressures, where we fixed $\log P_{N2} = 5$, and then show isolines corresponding to μ_O and μ_N at various $\log P_{O2}$ and temperature.

2.5.1 Synthesis of metal oxynitrides

Oxynitrides are a class of mixed-anion materials with applications for semiconductors and optoelectronics,[32] water-reduction photocatalysts,[33] electrocatalytic nitrogen reduction,[34] hard coating,[35] energy storage,[36,37] *etc*. Introducing additional anions with different sizes, electronegativities, and charges can effectively modulate the physical properties of oxide-based compounds[38,39]. However, oxynitrides are difficult to synthesize, and if synthesized, do not always retain operational stability (for example during catalysis in harsh electrochemical environments). Here, we examine the boundary conditions and relevant phase diagram in evaluating the stability of tantalum oxynitride, TaON.

It is not straightforward to experimentally control the oxygen and nitrogen *composition* in a reaction vessel, as oxygen and nitrogen are gases at standard state and at elevated temperatures. For this reason, it is not very convenient to examine oxynitride stability on phase diagrams with oxygen and nitrogen *composition* axes. If we are only concerned about the stability of the oxynitride, we can instead frame our thermodynamic system around just the oxynitride itself, with boundary conditions open to oxygen and nitrogen transfer, while closed in the non-volatile metal species. The corresponding phase diagram should therefore be a mixed x_{metal}-μ_{O}-μ_{N} diagram.

In **Figure 2.9a**, we illustrate the geometric connection between an all-extensive x_{metal}-x_{O}-x_{N} convex hull with its mixed x_{metal}-μ_{O}-μ_{N} phase diagram. For a target TaON phase, the blue triangle indicates the tangent plane to the TaON vertex. The intercept of this tangent plane with the energy axes at the pure elemental compositions corresponds to the elemental chemical potentials. Tilting this tangent plane about the TaON vertex maps out μ_{O} and μ_{N} chemical potentials where TaON is a stable equilibrium phase. This tangent plane tilting process is similar to retrieving the temperature and pressure of a phase on the Maxwell *U-S-V* surface, except that on the Maxwell surface the

slope of the tangent plane $\partial U/\partial X$ directly gives the intensive variable Y, whereas in affine composition axes (where $x_1 = 1 - x_2 - x_3$), the conjugate intensive chemical potential variable is given by the intercept rule.

The x_{Ta}-μ_O-μ_N phase diagram is shown in **Figure 2.9b**, where single-phase regions correspond to horizontal polygons with black borders parallel to the μ_O and μ_N axis. 2-phase coexistence regions are formed by the vertical rectangles connecting two single-phase polygons parallel to the x_{Ta} direction, The 3-phase coexistence regions are given by the vertical red lines that connect two 2-phase coexistence regions. The x_{Ta} axis shows how changing μ_O and μ_N can control the Ta molar fraction. However, this 3-dimensional diagram can also be projected onto just the μ_O-μ_N axes, as in **Figure 2.9d**.

The chemical potential of a gaseous phase is given by $\mu_{gas} = \mu_0 + RT\ln[P_{gas}] - TS_{gas}$, where μ_0 is the standard state chemical potential, P_{gas} is the partial pressure, and S_{gas} is its entropy. N_2(g) and O_2(g) are the equilibrium elemental phases at standard state, so for both oxygen and nitrogen, $\mu_0 = 0$ at 298K and $P = 1$ atm. The dependence of μ_{gas} on temperature and partial pressure is schematized in **Figure 2.9c**, which provides an experimental reference guide that can be used together with the x_{metal}-μ_O-μ_N. The combination of **Figures 2.9b**, **c**, **d** provides theoretical utility similar to the Ellingham diagram, however the Ellingham diagram cannot examine materials stability with two independent volatile gaseous species, whereas the chemical potential diagram construction can.

Although TaON is on the Ta-O-N convex hull, and is therefore a thermodynamically stable phase, its stability window is very narrow in the μ_O-μ_N diagram, meaning that the conditions to stabilize TaON may need to be very precise. In particular, μ_N should be much greater than μ_O for TaON to be stable. In **Figure 2.9f**, we place a yellow star in the TaON stability window at (μ_O, μ_N)

= (-4 eV, -0.9 eV). By referencing the diagram in **Figure 2.9e**, we can determine the O_2 and N_2 gas conditions that correspond to this TaON stability point.

For an oxynitride exposed O_2(g) and N_2(g), the temperatures of the two gases will be the same—however, their relative partial pressures can be varied independently. On **Figure 2.9e**, we should search for a temperature (a vertical line) that intersects iso-μ lines of -0.9 eV for N_2, and -4 eV for O_2. One such condition is at 1000K, with $\log P_{N2} = 5$ and $\log P_{O2} = -10$. In **Figure 2.9f**, we use a series of dotted lines to represent different temperatures and different $\log P_{O2}$, with each line having a fixed $\log P_{N2} = 5$. For most conditions, these lines fall in Ta_2O_5 region, showing that TaON is unstable with respect to Ta_2O_5 under most conditions in air. However, for the line $\log P_{O2} = -10$, we can intersect the TaON region at 1000K.

Although we conducted our stability analyses with respect to O_2 and N_2 gas, we can use other nitrogen or oxygen precursors to shift the μ_N and μ_O chemical potentials. For example, to overcome the triple bond in the N_2 molecule, nitrides are usually much more readily synthesized with activated nitrogen precursors, such as ammonia where the half reaction $\mu_N = \mu_{NH3} - 3/2\ \mu_{H2}$ yields $\mu_N = 0.4$ eV at standard state; and plasma-cracked atomic nitrogen has been benchmarked to $\mu_N = 1$ eV/N.[40,41] These chemical potentials are equivalent to N_2(g) partial pressures of 10^{16} atm and 10^{40} atm, respectively. A low oxygen chemical potential can also be obtained by reducing agents, for example, reduction with carbon monoxide yields an equilibrium chemical potential of $\mu_O = \mu_{CO2} - \mu_{CO} = -2.6$ eV/atom at STP, equivalent to an O_2(g) partial pressure of 10^{-104} atm (assuming the reaction is not kinetically-limited). Similar analyses can be done to obtain the effective chemical potential of chemical species in various other states, including solvated aqueous ions, or atoms in other solids.

The x_{Ta}-μ_O-μ_N chemical potential diagram can also yield other insights that cannot be readily obtained from a compositional phase diagram. **Figure 2.9d** show that to reduce Ta_2O_5 to metallic Ta, μ_O needs to be below -4.6 eV, which are also conditions generally needed to synthesize pure tantalum nitrides. The phase boundary between the various tantalum nitrides TaN_x and the Ta_2O_5 also indicates conditions for the stability of the pure tantalum nitrides in air.

2.5.2 Stability of the Li-ion cathode material $LiMn_2O_4$

$LiMn_2O_4$ is a candidate cathode material for rechargeable Li-ion batteries, in particular because Mn is not a critical element like cobalt-based battery electrodes.[42,43] $LiMn_2O_4$ has a spinel crystal structure with diffusion channels that enable fast diffusion of Li^+, even at relatively low concentration of Li^+ .[44,45] However, during the synthesis and electrochemical operation of $LiMn_2O_4$, many competing ternary $Li_xMn_yO_z$ phases can form, such as $Li_4Mn_5O_{12}$ and $LiMnO_2$, as well as the solid-solution phases that can form between these ternary phases and MnO_2, Mn_3O_4. (**Figure 2.10a,b**). The complexity of the available phases and structural transformations, especially between layered rocksalt structures and the spinel structures, can result in undesired phases in the form of impurities during synthesis, as well as irreversible decomposition pathways during electrochemical cycling and operation.

Under various synthesis or operation contexts, all 3 elements Li, Mn and O can be volatile in $LiMn_2O_4$. The oxygen chemical potential can be controlled by an oxidizing or reducing environment during synthesis, and likewise thermal decomposition by metal reduction and oxygen evolution also depends on μ_O[46] During battery charging and discharging, Li is cycled in and out of $LiMn_2O_4$ through the electrolyte,[22] where $\mu_{Li} = \mu_{Li,\text{metal}}^{o} - e\varphi$,[20] where φ is the electric potential, and $\mu_{Li,\text{metal}}^{o} = 0$ because μ is referenced to the chemical potential to elemental Li. Because the electrolyte is adjacent to $LiMn_2O_4$, the electrolyte can exchange Li, Mn or O with $LiMn_2O_4$. In

particular, one major issue hampering the widespread adoption of manganese-based cathodes is dissolution of the redox-active Mn ion in organic electrolytes, where Mn diffuses through the electrolyte to form an undesirable solid-electrolyte interface (SEI) at the anode, which erodes overall battery capacity.[47]

Although all three elements can be exchanged through an open boundary condition, it can be confusing to analyze $LiMn_2O_4$ stability on a full μ_{Li}-μ_{Mn}-μ_O chemical potential diagram, since it becomes difficult to isolate the work of the reservoir on the individual volatile species. It may be better to close the system to two components, and examine the role of the reservoir chemical potential on just the third component. From **Figure 2.10a** through **Figure 2.10d**, we illustrate how to interpret an x_{Li}-x_{Mn}-μ_O diagram from the Li-Mn-O ternary convex hull. Each slice in **Figure 2.10a, b** is an isopleth between oxygen and a fixed Li_xMn_{1-x} ratio. The Li:Mn isopleth with a 1:2 ratio (purple), corresponding to $LiMn_2O_4$, intersects both pure phases as well as 2-phase tie lines. By viewing the convex hull along this isoplethal slice in **Figure 2.10c**, we can use the intercept of tangent lines against the μ_O axis to illustrate the different phase transition and phase-coexistence regions. By repeating this process for all Li_xMn_{1-x} ratios, we can construct the full x_{Li}-x_{Mn}-μ_O diagram in **Figure 2.10d**. The right-side axis of **Figure 2.10c** shares the same color correspondence with the stability and coexistence regions in **Figure 2.10d**.

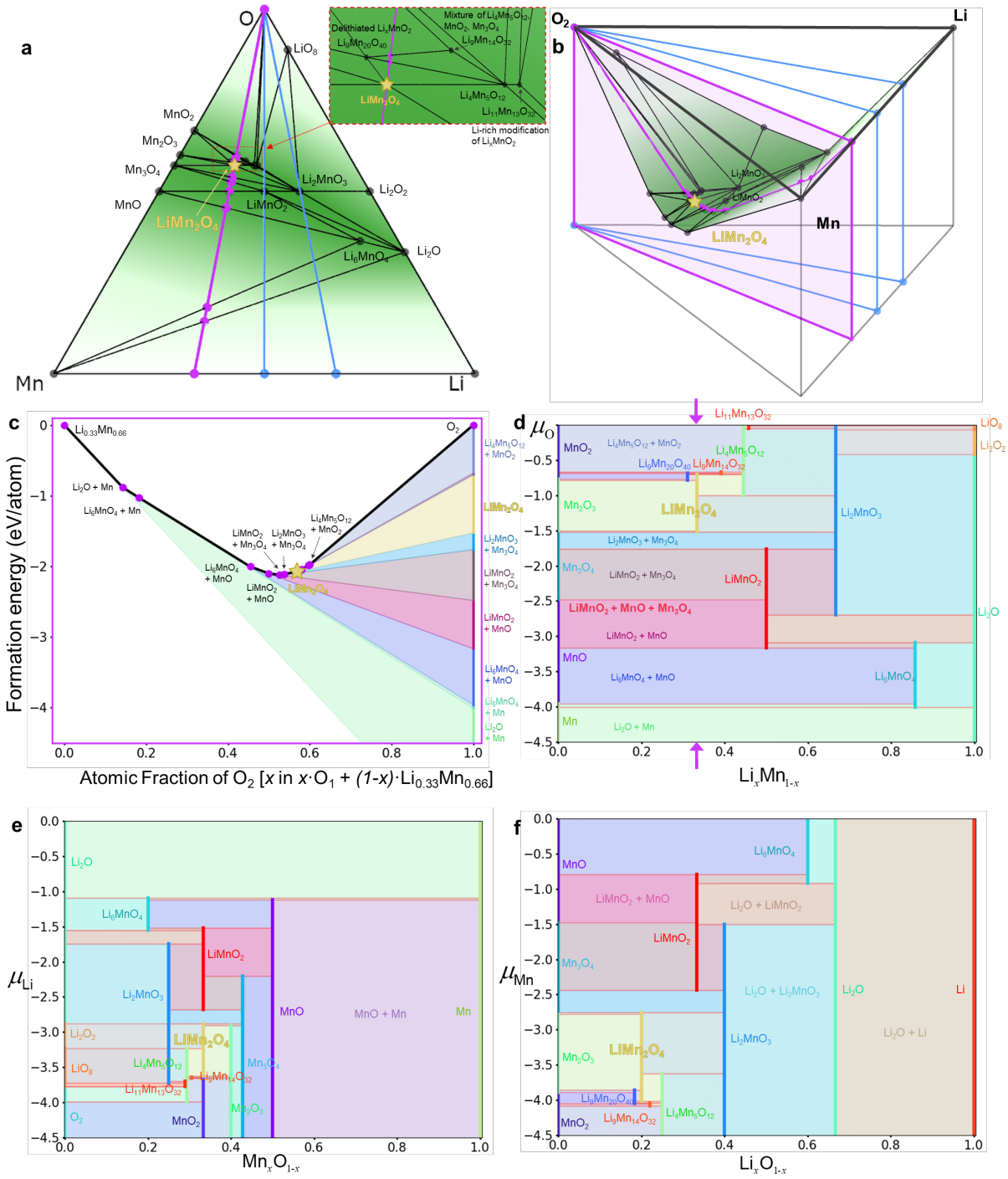

Figure 2.10: **a**) Ternary x_{Li}-x_{Mn}-x_O convex hull. Inset shows DFT calculated-phases with ordered compositions, where $Li_9Mn_{20}O_{40}$ phase represents delithiated Li_xMnO_2, the lithium-rich modification of $LiMn_2O_4$ is represented by $Li_{11}Mn_{13}O_{32}$, and the $Li_9Mn_{14}O_{32}$ phase represents a tie-line between MnO_2-$Li_4Mn_5O_{12}$. Isopleths between O_2 to Li_xMn_{1-x} are shown, with a purple highlight for a ratio of Li:Mn = 1:2. **b**) Ternary convex hull with energy axis, with isoplethal slices shown. **c)** Intercept rule construction of stability regions and phase coexistence along the μ_O axis. **d**) mixed x_{Li}-x_{Mn}-μ_O phase diagram, **e**) mixed x_{Mn}-x_O-μ_{Li} phase diagram, **f**) mixed x_{Li}-x_O-μ_{Mn} phase diagram. For the phase coexistence in x_1-x_2-μ_3 diagram, single phases are vertical lines, 2-phase coexistence regions are rectangles that connects two single phases, and 3-phase coexistence regions are horizontal red lines that connects the ends of three single phases.

From the x_{Li}-x_{Mn}-μ_O in **Figure 2.10d**, we can examine reactions involving $LiMn_2O_4$ with O_2 gas, for example during synthesis or thermal decomposition. The μ_O for O_2 gas can be referenced to different temperatures and partial pressures using the earlier diagram from **Figure 2.10c**. The μ_O stability window for $LiMn_2O_4$ is between [-1.5, -0.6] eV/atom; corresponding to temperature range around 600 – 900K, for P_{O2} ranges from [0.21, 1] atm, corresponding to ambient atmosphere. This stability condition is in line with the reported solid-state synthesis temperatures of $LiMn_2O_4$, which range from 700 – 1000K[48,49], as well as the thermal decomposition temperature of $LiMn_2O_4$ at 1100K.[50] Additionally, compared to layered structure electrodes, such as $LiMnO_2$, higher μ_O is beneficial for the stability of $LiMn_2O_4$, which matches the experimental fact that the Mn^{3+}/Mn^{4+} redox in $LiMn_2O_4$ requires a larger amount of oxygen redox to achieve high capacity, compared to Mn^{2+}/Mn^{4+} in $LiMnO_2$[51].

To analyze lithiation process of $LiMn_2O_4$ for a given Mn:O ratio, we can utilize the x_O-x_{Mn}-μ_{Li} axis. As shown in **Figure 2.10e**, when we raise the voltage (thereby decreasing μ_{Li}) to charge $LiMn_2O_4$, it undergoes oxidation and transforms into MnO_2. We note that on the equilibrium phase diagram, the MnO2 phase corresponds to the ground-state β (pyrolusite) phase, whereas for the real $LiMn_2O_4$ system, topotactic delithiation results in metastable λ-MnO_2, which maintains the spinel framework. On the other hand, reducing the electrostatic potential (increasing μ_{Li}) can result in phase separation to Li_2MnO_3 + Mn_3O_4. The μ_{Li} window between -3.7 and -2.8 eV/atom corresponds to the phase transitions between MnO_2 and $LiMn_2O_4$, as well as the transition from $LiMn_2O_4$ to $LiMnO_2$.

For electrolyte stability, Mn dissolution from $LiMn_2O_4$ will occur if the μ_{Mn} is lower in the electrolyte than the lower-limit μ_{Mn} stability window in $LiMn_2O_4$. For example, dissolution of Mn occurs if the applied μ_{Mn} in the electrolyte is below -4.1 eV, which as shown in **Figure 2.10f**, can

induce multiple phase transformations to $Li_4Mn_5O_{12}$, $Li_9Mn_{20}O_{40}$, $Li_9Mn_{14}O_{32}$. To design an organic electrolyte that is resistant to Mn-dissolution, one needs to identify an organic electrolyte where the Mn-ion solvation energy overlaps the stability window of $LiMn_2O_4$ in the μ_{Mn} axis. To perform this analysis, one can construct the corresponding chemical potential diagram of the electrolyte from a convex hull using the same tangent line principles discussed here.

2.5.3 Oxidation of compositionally-complex alloys

Compositionally-complex alloys (CCAs) have near equimolar concentrations of multiple metal species, and in special cases form single-phase solid-solution high-entropy alloys (HEAs) and medium-entropy alloys (MEAs), which may have valuable properties for high-temperature materials for spacecraft and satellites, [52] corrosion-resistance for seawater treatment equipment, [53, 54] superior electron transport for electronic device, *etc*. [55, 56, 57] However, discontinuous oxide granules or oxide layers can form when these alloys are exposed to O_2 atmospheres and high temperature. Although experimental measurements of the surface oxide phases formed in HEAs and MEAs are becoming more numerous,[58,59] thermodynamic modeling remains sparse. [60] This may be due to the complexity of the possible binary, ternary, and quaternary oxides that compete to form during HEA/MEA oxidation.

To analyze the oxidation behaviors of multi-component alloys, we take $CrCoNiO_x$ as a representative example. The chemical potential of oxygen in an HEAs depends on many factors, such as penetration depth of oxygen as it diffuses in, as well as the μ_O applied by the temperature and partial pressure of O_2 gas at the surface. The appropriate boundary conditions for this system are closed in the metal species, but with open exchange of volatile oxygen species. The relevant phase diagram is therefore closed with metal composition axes x_{Cr}-x_{Co}-x_{Ni}, and open with a μ_O axis.

For the sake of visualization, we examine a here 3-metal MEA, however, the underlying geometric arguments and analyses are readily extendable to higher-component alloys.

Typically, phase diagrams for 4-component systems are viewed in barycentric coordinates using a 3D Gibbs tetrahedron to represent the quaternary convex hull, with 4 composition variables but no energy axis (**Figure 2.11a**). The energy axis can be recovered by constructing pseudo-ternary convex hulls by taking compounds as terminal points of the convex hull, and plotting the formation energy of phases relative to the terminal compounds, as illustrated in **Figure 2.11b**.

Each phase in the quaternary convex hull is a vertex, which we assign a color corresponding to the metal composition. We assign red, green, and blue to Co, Cr, and Ni, respectively. The color of binary through quaternary phases are then determined by their barycentric Co:Cr:Ni molar ratio. We use color saturation to correspond to the lowest critical oxygen chemical potential in which the phase is thermodynamically preferred to form, where white indicates pure O_2 gas.

Figure 2.11c, **d** shows two x_{Cr}-x_{Co}-x_{Ni}-μ_O phase diagrams at high and low μ_O ranges—split up to more clearly visualize the phase coexistence regions. By comparing the critical oxygen chemical potentials, we can extract the tendency of various metal constituents to oxidize; for example, Cr will oxidize at μ_O = -4 eV to form a protective Cr_2O_3 scale, which is before Ni and Co which both oxidize around μ_O = -2.5 eV. Experimentally, the oxidation of equimolar CrCoNi is shown to form only a Cr_2O_3 layer[55,56,58], as anticipated by these diagrams. Additionally, a mixed spinel (Co,Ni)Cr_2O_4 is experimentally observed[55,56,58,61], which in our phase diagram on **Figure 2.11c** may correspond to a solid-solution that would form along the tie line between $CoNi_2O_4$ and $CrNiO_4$.

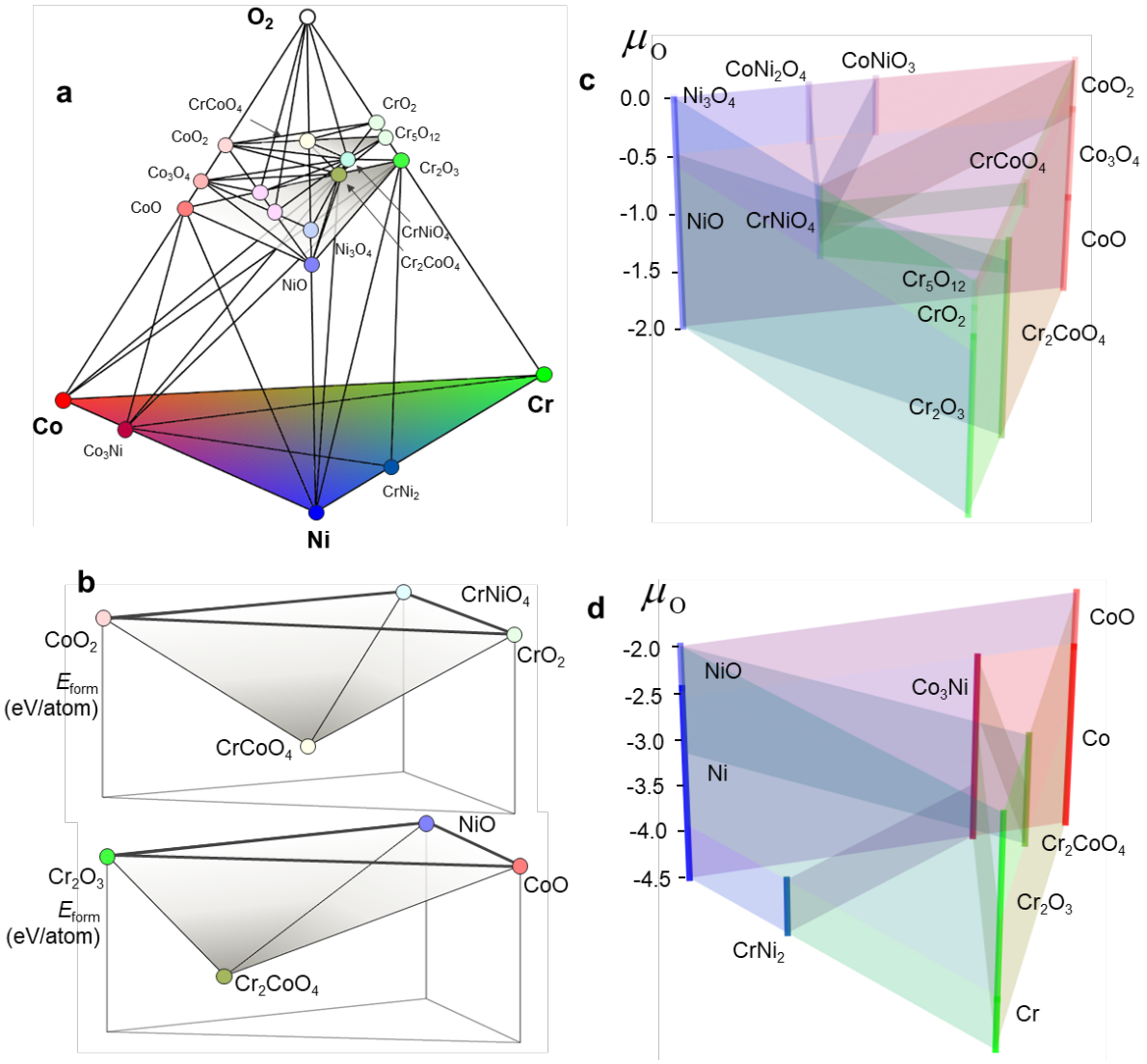

Figure 2.11: **a**) Quaternary x_{Co}-x_{Cr}-x_{Ni}-x_O convex hull. Each single phase is assigned a color based on metal composition of Cr:Co:Ni ratio, and a transparency based on the lowest critical μ_O for a given phase. Two triangular ternary isopleths are shown in gray colorscale, connecting CoO_2-$CrNiO_4$-CrO_2, and Cr_2O_3-NiO-CoO. **b**) Psuedo-ternary convex hulls with a recovered formation energy axis, with energies referenced to the terminal compound phases. **c**). Mixed x_{Cr}-x_{Co}-x_{Ni}-μ_O phase diagram, where **c**) μ_O in [-2.0, 0.0] eV/atom, and **d**) μ_O in [-4.5, -2.0] eV/atom.

In **Figure 2.11c**, **d**, each single phase is a vertical line, a 2-phase coexistence region is vertical rectangle plane bounded by two single phase lines, a 3-phase coexistence region is a triangular prism formed by three single phase lines, and finally a 4-phase coexistence region is a horizontal triangle connected by two 3-phase coexistence triangular prisms. Although 2-phase coexistence regions and 4-phase coexistence regions are both 2-D manifolds, they have different physical interpretations because there is no degree of freedom for changing μ_O in 4-phase

coexistence, leading to a horizontal 2D region, whereas we can change μ_O in 2-phase coexistence, leading to a vertical 2D region.

2.5.4 Computation of mixed composition/chemical potential diagrams

We now describe the computational construction of mixed composition and chemical potential diagrams. The implementation Python codes and tutorial examples are in Github link:

https://github.com/dd-debug/chemical_potential_diagram_and_convex_hull_and_pourbaix_diagram

Our approach here involves the extraction of extensive variables x_i information from the convex hull, followed by the acquisition of intensive variables μ_i from chemical potential diagrams. Note that all the compositional data of both single-phase and phase coexistence regions are embedded in the Pymatgen convex hull phase diagram analysis package. Furthermore, the computation of chemical potential information can be achieved through our half-space intersection (**Chapter 2.3.4**) method.

Our discussion focuses on the equilibrium states of materials, with chemical potential information derived from the equilibrium envelope (outlined in **Chapter 2.3.4.3**) from the chemical potential diagram. Using a ternary system as an example, in compositional space (x_1-x_2-x_3), each single phase is represented as a point, a 2-phase coexistence is symbolized by a tie line connecting the two single phases, and a 3-phase coexistence is a triangular region defined by three single phases as terminal points. In contrast, when considering a ternary system in chemical potential space (μ_1-μ_2-μ_3), each single phase is characterized as a 2D polygon, and a 2-phase coexistence region is a linear segment shared by two single phases. In this scenario, a 3-phase coexistence region simplifies to a point, as no degree of freedom exists for chemical potential

alterations at such a juncture. This point corresponds to the intercepts of a tangent plane over a 3-phase coexistence triangle on the convex hull.

2.5.4.1 μ_1-μ_2-x_3 phase diagram (x_{Ta}-μ_O- μ_N)

Within the μ_1-μ_2-x_3 phase diagram, the dimensionality of a single phase depends on the projection of the equilibrium envelope onto the μ_1 and μ_2 axes. Each material is inherently represented as a 2-D polygon within the μ_1-μ_2-μ_3 space, which implies that its projection onto any two μ_1 and μ_2 axes generally results in 2-D polygons. However, when we project a 2-D polygon from the 3-D (μ_1-μ_2-μ_3) space onto a 2-D (μ_1-μ_2) plane, the information related to μ_3 is disregarded. The dimensionality of this projection hinges on the orientation of the plane in the 3-D space. For instance, as illustrated in **Figure 2.9c**, if we had phases without Ta, they would be lines when projected to μ_O and μ_N (here we manually remove all N_xO_y gas phases); whilst phases with Ta are 2-D polygons. Further discussion regarding this projection methodology is in Chapter 3.[62]

A 2-phase region is a 1D line in both a ternary convex hull and ternary chemical potential diagram, so it is 2D rectangle in μ_1-μ_2-x_3 diagram that has one principal axis in the μ_1-μ_2 plane, and one principal axis in the x_3 direction. A 3-phase coexistence has a fixed chemical potential μ_1, so it is a vertical line parallel to the x_3 direction. To identify 2-phase or 3-phase regions, we systematically examine every combination of two / three single phases to see if they shared a common line / vertex. Finally, 2-phase regions are plotted as vertical plane, and 3-phase regions are plotted as vertical red lines, as shown in **Figure 2.9b**.

2.5.4.2 μ_1-x_2x_3 phase diagram (μ_{Li}-$x_{Mn}x_O$)

Because of the affine constraint, the molar ratio between Element 2 and Element 3 can be represented with a single variable, which we refer to as x_2x_3. This means that a μ_1-x_2x_3 phase diagram is in fact a 2D phase diagram. A single phase on the equilibrium envelope of a μ_1-μ_2-μ_3

diagram is given by a 2-D polygon, meaning it has a single value of x_2x_3; and a linear μ_1 range for the single phase, defined by calculating its maximum and minimum values along the μ_1 axis. As a result, a single phase is depicted as a 1-D line parallel to the μ_1 axis, in **Figure 2.10d**, **e**, **f**.

A 2-phase region appears as a line in both the ternary convex hull and the three-component equilibrium envelope. This implies that a 2-phase region in μ_1-x_2x_3 diagram is a 2D rectangle. During the calculation of the equilibrium envelope, the *HalfspaceIntersection* class returns facets in the form of interconnected triangles, collectively forming two-dimensional polygons corresponding to individual phases. Co-planar triangles may need to be merged in order to produce non-simplicial polygons. The identification of the boundary lines for each phase can be achieved by counting the number of appearances for each boundary line. Specifically, the true boundary lines associated with a single phase occur only once, whereas interior edges formed from two co-planar triangles are counted twice, since they share two adjacent triangles.

To find the μ_1 range of 2-phase regions, we systematically examine every combination of two single phases to see if they share common boundary lines. If they do, it represents the two phases can coexist. This process yields the μ_1 span for each 2-phase coexistence region, which can be combined with the calculation of the two-phase coexistence regions for x_2x_3 from a convex hull to generate a 2D rectangle.

Since a 3-phase region is characterized by a single point, with fixed chemical potential values, its dimensionality depends on the projection of a 3-phase triangle from convex hull to x_2x_3 space, resulting in a 1D line that is parallel to the x_2x_3 axis. Similar to the approach used for 2-phase regions within equilibrium envelope, we systematically examine every combination of three single phases to see if they shared a common vertex. If they do, it signifies a 3-phase coexistence

region. By finding its μ_1 value and calculating the molar ratio x_2x_3 range of the three coexisting phases, a horizontal 3-phase line could be constructed, as horizontal red line in **Figure 2.10d**, **e**, **f**.

2.5.4.3 μ_1-x_2-x_3-x_4 phase diagram (μ_O-x_{Ni}-x_{Cr}-x_{Co})

Quaternary systems follow a similar pattern as ternary systems. In convex hulls, a 4-phase coexistence region is a 3D tetrahedron. Unlike the convex hull, the equilibrium envelope does not use barycentric coordinates, necessitating a discussion on the visualization of higher dimensional polytopes. Intuitively, the μ_1-x_2-x_3-x_4 diagram can be envisioned as a compilation of various ternary Gibbs compositional triangles x_2-x_3-x_4 at different μ values. In the μ-axis, single phase regions are vertical lines since they have fixed composition and linear range on μ_1 axis. By determining the maximum and minimum values of μ_1 for each phase, we can visualize single phases. All the single, 2-phase, and 3-phase coexistence regions within a ternary composition phase diagram are preserved. The interesting coexistence phenomena in a μ_1-x_2-x_3-x_4 then arise at the boundaries between ternary phase diagram slices, as discussed below.

For a 2-phase region, the chemical potential can change along μ_1. So, a 2-phase region can be a vertical rectangle connecting two single phase vertical lines (here vertical refers to parallel to the μ axis). 2-phase coexistence can also represent the crossover point between two pure phases in the vertical axis, for example, the point between Co and CoO.

Given that the exhaustive combination of every two single phases in a 4-component system can be computationally demanding, we adopt an efficient approach. Initially, we identify the distinct μ_1 ranges shared by different sets of entries. Subsequently, we extend the compound phase diagram along the μ_1 direction, generating triangular prisms for each specific μ_1 range. Finally, these triangular prisms are interconnected to form a comprehensive representation. This method

leverages the *GrandPotentialPhaseDiagram* class from pymatgen to construct the compound phase diagram.

In the case of a 3-phase region, besides one degree of freedom offered by chemical potentials, the 3-phase triangle within the convex hull can be transformed into a $x_2x_3x_4$ Gibbs triangle. In this scenario, the overall dimensionality is 3-D. To be more specific, the 3-phase region takes the form of a triangular prism, with the Gibbs triangle extending along the μ_1 direction. A 4-phase region assumes the shape of a Gibbs $x_2x_3x_4$ triangle. This is because the chemical potentials are fixed (resulting in 0-D), while the composition is allowed to vary within the $x_2x_3x_4$ triangle.

2.5.5 Dimensionality of Coexistence Regions in Mixed Diagrams

The essential geometric object corresponding to phase coexistence is the simplicial polytope, which is an *N*-dimensional analogue of a triangle. The counting relations between the vertices, edges, and facets of a simplicial polytope are given by the Dehn-Somerville relations, which takes a similar form to Pascal's triangle. For example, a 4-phase coexistence tetrahedron is a 3-dimensional simplex, which has ${}_4C_1 = 4$ vertices (single phases), ${}_4C_2 = 6$ edges (2-phase coexistence), ${}_4C_3 = 4$ triangles (3-phase) and ${}_4C_4 = 1$ tetrahedron (4-phase). Even when one performs a Legendre transformation, the fundamental underlying geometric structure of the $U(S,X)$ simplex, as well as its coexistence regions, are preserved.

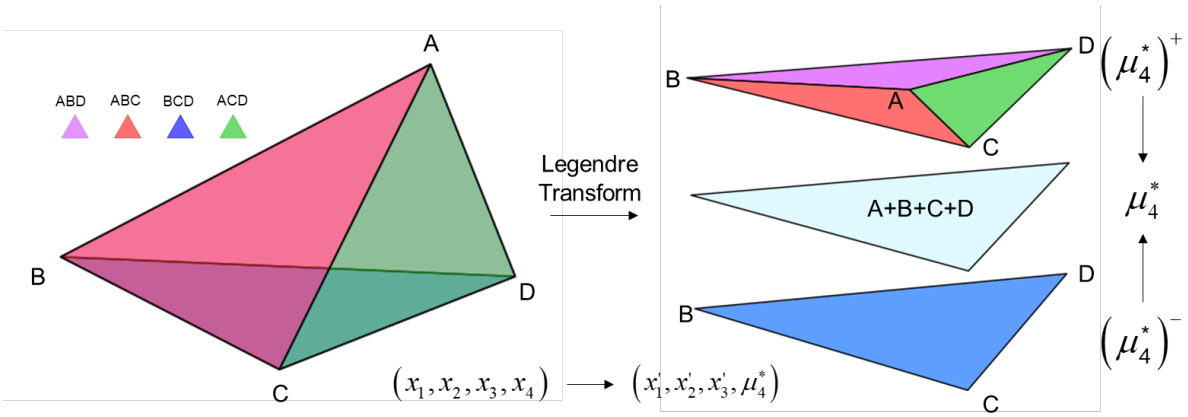

Figure 2.12: A 3D simplicial polytope (a tetrahedron) with extensive natural variables is smushed via a Legendre transformation to a fixed intensive variable of μ_4^*. All simplicial facets from the tetrahedron, and thereby its phase coexistence information, remains preserved following the Legendre transformation.

On a four-phase coexistence tetrahedron, all vertices share the same chemical potentials μ_1 through μ_4. On composition axes, the coordinates for each vertex can be written as (x_1, x_2, x_3, x_4), where 1, 2, 3, 4 correspond to different elements, and $x_4 = 1 - x_1 - x_2 - x_3$ by the affine constraint. Upon a Legendre transformation from x_4 to μ_4, the x_4 coordinates all change to the same μ_4, which effectively smushes all the vertices, edges and facets from the tetrahedron onto a single μ_4^* value, as illustrated in **Figure 2.12**. Each x_i coordinate then changes to x_i' by the new affine constraint, $x_3' = 1 - x_1' - x_2'$.

Importantly, all the 2-phase edges, 3-phase triangles, and the 4-phase tetrahedron are preserved after the Legendre transformation. The Legendre transformation does not generate any new phase coexistence information, nor does it lose any information. It simply provides a different perspective, but for the same equilibrium of heterogeneous substances. On mixed phase diagrams the phase coexistence regions no longer appear like simplicial polytopes, but are in fact down-projections of the high-dimensional simplices from the $U(S,X_i)$ space where they originated. These the geometric considerations of phase coexistence are the same with any other intensive variable as well, for example on a traditional ternary composition phase diagram (x_1, x_2, x_3, T), or replacing μ_4 with pressure, magnetic field, area-to-volume ratio, *etc.*

2.5.5.1 A generalized phase rule for mixed μ-x diagrams

Here we detail a generalized phase rule for the dimensionality of phase coexistence regions in mixed μ-x phase diagrams. In a system with N components, these regions possess $N - C$ dimensions in chemical potential space and $C - 1$ dimensions in convex hull space, based on Point-line duality. When all elements of the C-phase span all composition axis, the dimensionality remains $N - C$, if the number of μ-axes (N_μ) used for visualization is more than $N - C$. For instance, a 2-phase region in a quaternary system within μ_1-μ_2-μ_3 space is 2-D. However, if N_μ is smaller than $N - C$, the dimensionality of the C-phase coexistence regions is reduced to N_μ.

> N: elements number
> N_μ: the number of μ axis to be visualized
> $N - C$: dimensionality of a C-phase coexistence region in μ space.
> For μ, dimensionality of a C-phase coexistence region to be visualized is: min (N-C, N_μ)

Similarly, if the number of composition axis we want to visualize (N_x) is smaller than the dimension number of C-phase coexistence region ($C - 1$), for the visualization of composition axis, the C-phases coexistence polytope dimensions are N_x.

> N_x: the number of x axis to be visualized
> C-1: dimension of a C-phases coexistence region in compositions space
> For x, dimensionality of a C-phase coexistence region to be visualized is: min (C-1, N_x-1)

Finally, we add the dimensions for μ and composition together.

> Finally, the dimensionality of a C-phase coexistence polytope for a N-component system in a $\mu{\cdot}N_\mu$-$x{\cdot}N_x$ diagram is: min (N–C, N_μ) + min (C–1, N_x–1)

For example, for 1-phase region for quaternary system in μ_1-μ_2-x_3x_4 phase diagram, for μ, dimension to be visualized is min (4–1, 2) D, which is 2D; for compositions, dimension to be visualized is min (2–1, 2–1), which is 1D. Therefore, the total dimension is 3D. We also offer other quaternary system dimensionality of phase coexistence regions in **Table 2.3**.

Table 2.3: Table of dimensionality of phase coexistence regions in quaternary μ-x phase diagrams.

	1-phase	**2-phase**	**3-phase**	**4-phase**
μ_1-μ_2-μ_3-μ_4	3-D polytope	2-D plane	1-D line	0-D point
x_1-x_2-x_3-x_4	0-D point	1-D line	2-D triangle	3-D tetrahedron
μ_1-$x_2x_3x_4$	1-D line	2-D vertical rectangle	3-D triangular prism	2-D triangle
μ_1-μ_2-μ_3-x_4	2-D polygons for phases w/o x_4; Others: 3-D polytopes	2-D rectangle for 2-phase w/o x_4; 3-D prism for others;	1-D line for 3-phase w/o x4; 2-D rectangle for others	1-D line
μ_1-μ_2-x_3x_4	1-D lines for phases w/o x_3 & x_4; Others: 2-D polygons	If x_4 is covered in 2-phase: 3-D polytope	If x_4 is covered in 3-phase: 2-D polygon	1-D line

2.6 Outlook

Duality gives *two different points of view of looking at the same object*. As summarized in the table below, there is a duality in thermodynamics between open and closed systems; which corresponds to a duality between the Internal Energy potential and its Legendre transformation; which corresponds to a duality in computation between a convex hull and its half-space intersection. Our implementation of these duality concepts for chemical work are geometrically identical to the duality relationships between the Maxwell $U(S,V)$ surface and the $G(T,P)$ free energy surfaces which we are commonly familiar with today. Our primary contribution here was to extend these concepts from the $G(T,P,x)$ space to the grand potential $\phi(T,P,\mu)$ space. The dualities in macroscopic boundary conditions for classical thermodynamics can further be linked to dualities at the atomistic scale, in the statistical mechanics description between an *NVT* canonical ensemble and the μVT grand canonical ensemble.

Table 2.4: Table of duality in thermodynamics.

Duality in Thermodynamics		
Thermodynamic System	Closed equilibrium mixture of heterogeneous substances	Subsystem of single material open to an external reservoir

Thermodynamic Potential	Internal Energy $U(X_i)$ with extensive natural variables	Legendre transformation to $\Phi(Y_i)$ with natural intensive variable
Computational Thermodynamics	Convex hull of vertices	Half-space intersection of hyperplanes

Our motivation for this work was to address the underutilization of chemical potential diagrams in the existing materials thermodynamics literature. Although computational tools for chemical potential diagrams have existed for over two decades, we believe that the bottleneck to their widespread proliferation is not their computation, but rather, is the physical understanding and interpretation of these diagrams. In particular, chemical potential diagrams offer a unique connection to the kinetics of diffusion, nucleation and growth, which has broad and obvious value in materials science and engineering. Therefore, the essential intellectual task in deploying chemical potential diagrams (or any phase diagram for that matter) is connecting a physical scenario to its boundary conditions and corresponding thermodynamic potential, and then from the available thermochemical data to the computation of a final phase diagram.

In framing open boundary conditions to analyze the stability of a material-of-interest with respect to an open reservoir, the next question becomes, how can one control the relative stability of a target material, when there may be numerous forms of available work? In **Chapter 3**, we derive a generalized Clausius-Clapeyron relation to examine the gradients of phase boundaries on high-dimensional phase diagrams, providing a pathway to control the relative stability of specific phases.

[1] Atiyah, M. F. "Duality in mathematics and physics." *Conferències FME* 5 (2007): 2007-2008.

[2] Gibbs, Josiah Willard, and Edwin Bidwell Wilson. *Vector analysis: A text-book for the use of students of mathematics and physics, founded upon the lectures of j. willard gibbs*. Yale University Press, 1901.

[3] Fathi, Mohammad Bagher. "History of the reciprocal lattice." *Powder Diffraction* 34.3 (2019): 260-266.

[4] Sun, Wenhao, and Matthew J. Powell-Palm. "Generalized Gibbs' Phase Rule." arXiv preprint arXiv:2105.01337 (2021).

[5] Chen, Jiadong, Matthew J. Powell-Palm, and Wenhao Sun. "The geometry of high-dimensional phase diagrams: II. The duality between closed and open chemical systems." *arXiv preprint arXiv:2404.05197* (2024).

[6] Yokokawa, H. "Generalized chemical potential diagram and its applications to chemical reactions at interfaces between dissimilar materials." *Journal of phase equilibria* 20.3 (1999): 258-287.

[7] Ahmad, E. A., et al. "Thermodynamic stability of LaMnO3 and its competing oxides: A hybrid density functional study of an alkaline fuel cell catalyst." *Physical Review B* 84.8 (2011): 085137.

[8] https://onlinelibrary.wiley.com/doi/abs/10.1002/adma.200700843

[9] Reuter, Karsten, and Matthias Scheffler. "First-principles atomistic thermodynamics for oxidation catalysis: surface phase diagrams and catalytically interesting regions." *Physical review letters* 90.4 (2003): 046103.

[10] Reuter, Karsten, and Matthias Scheffler. "Composition, structure, and stability of RuO 2 (110) as a function of oxygen pressure." *Physical Review B* 65.3 (2001): 035406.

[11] Kitchin, John R., Karsten Reuter, and Matthias Scheffler. "Alloy surface segregation in reactive environments: first-principles atomistic thermodynamics study of Ag 3 Pd (111) in oxygen atmospheres." *Physical Review B* 77.7 (2008): 075437.

[12] Korte-Kerzel, Sandra, et al. "Defect phases–thermodynamics and impact on material properties." *International Materials Reviews* 67.1 (2022)

[13] Freysoldt, Christoph, et al. "First-principles calculations for point defects in solids." *Reviews of modern physics* 86.1 (2014): 253.

[14] Todd, Paul K., et al. "Selectivity in yttrium manganese oxide synthesis via local chemical potentials in hyperdimensional phase space." *Journal of the American Chemical Society* 143.37 (2021): 15185-15194.

[15] Chen, Jiadong, et al. "Navigating phase diagram complexity to guide robotic inorganic materials synthesis." *arXiv preprint arXiv:2304.00743* (2023).

[16] Wen, Mingjian, et al. "Chemical reaction networks and opportunities for machine learning." *Nature Computational Science* 3.1 (2023): 12-24.

[17] Feinberg, Martin. "Foundations of chemical reaction network theory." (2019).

[18] Jackson, Adam J., Davide Tiana, and Aron Walsh. "A universal chemical potential for sulfur vapours." *Chemical science* 7.2 (2016): 1082-1092.

[19] Nair, Sreejith, et al. "Solid-source metal-organic MBE for elemental Ir and Ru films." *Journal of Vacuum Science & Technology A* 41.6 (2023).

[20] Sun, Wenhao, et al. "Non-equilibrium crystallization pathways of manganese oxides in aqueous solution." *Nature communications* 10.1 (2019): 573.

[21] Richards, William D., et al. "Interface stability in solid-state batteries." *Chemistry of Materials* 28.1 (2016): 266-273.

[22] Zhu, Yizhou, Xingfeng He, and Yifei Mo. "Origin of outstanding stability in the lithium solid electrolyte materials: insights from thermodynamic analyses based on first-principles calculations." *ACS applied materials & interfaces* 7.42 (2015): 23685-23693.

[23] Callen, Herbert B., and H. L. Scott. "Thermodynamics and an Introduction to Thermostatistics." (1998): 164-167.

[24] Zia, Royce KP, Edward F. Redish, and Susan R. McKay. "Making sense of the Legendre transform." *American Journal of Physics* 77.7 (2009): 614-622.

[25] Jain, Anubhav, et al. "Commentary: The Materials Project: A materials genome approach to accelerating materials innovation." *APL materials* 1.1 (2013).

[26] Ong, Shyue Ping, et al. "Li− Fe− P− O2 phase diagram from first principles calculations." *Chemistry of Materials* 20.5 (2008): 1798-1807.

[27] Hautier, Geoffroy, et al. "Accuracy of density functional theory in predicting formation energies of ternary oxides from binary oxides and its implication on phase stability." *Physical Review B* 85.15 (2012): 155208.

[28] Kirklin, Scott, et al. "The Open Quantum Materials Database (OQMD): assessing the accuracy of DFT formation energies." *npj Computational Materials* 1.1 (2015): 1-15.

[29] Wang, Amanda, et al. "A framework for quantifying uncertainty in DFT energy corrections." *Scientific reports* 11.1 (2021): 15496.

[30] Jain, Anubhav, et al. "Formation enthalpies by mixing GGA and GGA+ U calculations." *Physical Review B* 84.4 (2011): 045115.

[31] Kingsbury, Ryan S., et al. "A flexible and scalable scheme for mixing computed formation energies from different levels of theory." *npj Computational Materials* 8.1 (2022): 195.

[32] Jang, Jun Tae, et al. "Study on the photoresponse of amorphous In–Ga–Zn–O and zinc oxynitride semiconductor devices by the extraction of sub-gap-state distribution and device simulation." *ACS applied materials & interfaces* 7.28 (2015): 15570-15577.

[33] Ahmed, Manan, and Guo Xinxin. "A review of metal oxynitrides for photocatalysis." *Inorganic Chemistry Frontiers* 3.5 (2016): 578-590.

[34] Young, Samuel D., et al. "Metal oxynitrides for the electrocatalytic reduction of nitrogen to ammonia." *The Journal of Physical Chemistry C* 126.31 (2022): 12980-12993.

[35] Zhang, Zongbo, et al. "Hydrophobic, transparent and hard silicon oxynitride coating from perhydropolysilazane." *Polymer International* 64.8 (2015): 971-978.

[36] Yu, Minghao, et al. "Holey tungsten oxynitride nanowires: novel anodes efficiently integrate microbial chemical energy conversion and electrochemical energy storage." *Advanced materials* 27.19 (2015): 3085-3091.

[37] Young, Samuel D., et al. "Thermodynamic Stability and Anion Ordering of Perovskite Oxynitrides." *Chemistry of Materials* 35.15 (2023): 5975-5987.

[38] Harada, Jaye K., et al. "Heteroanionic materials by design: Progress toward targeted properties." *Advanced Materials* 31.19 (2019): 1805295.

[39] Kageyama, Hiroshi, et al. "Expanding frontiers in materials chemistry and physics with multiple anions." *Nature communications* 9.1 (2018): 772.

[40] Caskey, Christopher M., et al. "Thin film synthesis and properties of copper nitride, a metastable semiconductor." *Materials Horizons* 1.4 (2014): 424-430.

[41] Sun, Wenhao, et al. "The thermodynamic scale of inorganic crystalline metastability." *Science advances* 2.11 (2016): e1600225.

[42] Thackeray, Michael M. "Manganese oxides for lithium batteries." *Progress in Solid State Chemistry* 25.1-2 (1997): 1-71.

[43] Deng, Yuanfu, et al. "Recent advances in Mn-based oxides as anode materials for lithium ion batteries." *Rsc Advances* 4.45 (2014): 23914-23935.

[44] Lee, Jinhyuk, et al. "Unlocking the potential of cation-disordered oxides for rechargeable lithium batteries." *science* 343.6170 (2014): 519-522.

[45] Thackeray, M. M., et al. "Electrochemical extraction of lithium from LiMn2O4." *Materials Research Bulletin* 19.2 (1984): 179-187.

[46] Lee, Byungju, et al. "First-principles study of the reaction mechanism in sodium–oxygen batteries." *chemistry of Materials* 26.2 (2014): 1048-1055.

[47] Huang, Yimeng, et al. "Lithium manganese spinel cathodes for lithium-ion batteries." *Advanced Energy Materials* 11.2 (2021): 2000997.

[48] Macklin, W. J., R. J. Neat, and R. J. Powell. "Performance of lithium manganese oxide spinel electrodes in a lithium polymer electrolyte cell." *Journal of power sources* 34.1 (1991): 39-49.

[49] Momchilov, A., et al. "Rechargeable lithium battery with spinel-related MnO2 II. Optimization of the LiMn2O4 synthesis conditions." *Journal of power sources* 41.3 (1993): 305-314.

[50] Buzanov, G. A., et al. "Phase equilibria involving solid solutions in the Li–Mn–O system." *Russian Journal of Inorganic Chemistry* 62 (2017): 551-557.

[51] Lee, Jinhyuk, et al. "Reversible Mn2+/Mn4+ double redox in lithium-excess cathode materials." *Nature* 556.7700 (2018): 185-190.

[52] Sharma, Aayush, et al. "Atomistic clustering-ordering and high-strain deformation of an Al0. 1CrCoFeNi high-entropy alloy." *Scientific reports* 6.1 (2016): 31028.

[53] Qiu, Yao, et al. "Corrosion of high entropy alloys." *npj Materials degradation* 1.1 (2017): 15.

[54] Chen, Ganlin, et al. "Stability and growth kinetics of {112} twin embryos in β-Ti alloys." *Acta Materialia* 263 (2024): 119520.

[55] Agustianingrum, Maya Putri, Unhae Lee, and Nokeun Park. "High-temperature oxidation behaviour of CoCrNi medium-entropy alloy." *Corrosion Science* 173 (2020): 108755.

[56] Stephan-Scherb, Christiane, et al. "High-temperature oxidation in dry and humid atmospheres of the equiatomic CrMnFeCoNi and CrCoNi high-and medium-entropy alloys." *Oxidation of Metals* 95 (2021): 105-133.

[57] Evans, Daniel, et al. "Visualizing temperature-dependent phase stability in high entropy alloys." *npj Computational Materials* 7.1 (2021): 151.

[58] Kai, W., et al. "High-temperature air-oxidation of NiCoCrAlx medium-entropy alloys." *Corrosion Science* 192 (2021): 109858.

[59] Jiang, Dong, et al. "High-temperature oxidation behaviors of an equiatomic CrMnFeCoNi high entropy alloy." *Materials Today Communications* 32 (2022): 104185.

[60] Butler, Todd M., and Mark L. Weaver. "Oxidation behavior of arc melted AlCoCrFeNi multi-component high-entropy alloys." *Journal of Alloys and Compounds* 674 (2016): 229-244.

[61] Schaefer, Seth C. *Electrochemical determination of thermodynamic properties of NiCr2O4 and CoCr2O4*. No. 9043. US Department of the Interior, Bureau of Mines, 1986.

[62] Chen, Jiadong, Matthew J. Powell-Palm, and Wenhao Sun. "The geometry of high-dimensional phase diagrams: III. Engineering relative stability in four dimensions." *arXiv preprint arXiv:2404.05201* (2024).

Chapter 3 Generalized Clausius Clapeyron Equations and Pourbaix Diagrams

3.1 Represent relative stability at phase boundary

A primary goal in materials thermodynamics is to construct phase diagrams with accurate and precise phase boundaries for all known phases in a chemical system. However, the 'thermodynamic assessments' required to construct accurate phase diagrams[1,2,3,4] can be very time-consuming. This process involves compiling all calorimetric and DFT-computed thermochemical data, constructing free-energy models for the solids, solid-solutions and liquid phases, then critically evaluating the resulting phase diagrams against experimentally-observed phase boundaries, while adhering to Gibbs Phase Rule and other thermodynamic considerations of phase coexistence.[5] Because thermodynamic assessments can be such a laborious process, phase diagrams do not exist in many materials engineering contexts, despite their obvious importance and utility.

It would be valuable to develop a simpler and more agile framework to explore the stability conditions of materials. We propose that in many materials engineering situations, it may not actually be necessary to map out the full phase diagram. Instead, it may be enough to just characterize the stability of a desired target phase *relative* to its competing phases. For example, perhaps we aim to synthesize a target phase α, but experimentally we observe that α transforms to an undesired β phase, or that formation of α is blocked by the undesired nucleation of γ, *etc*. The salient question then becomes: How do we modify our experimental conditions to promote the stability of α, while destabilizing all other competing phases? In other words, how do I engineer

the *relative stability* between a desired target phase versus an experimentally-obtained undesired phase?

High-dimensional phase diagrams become increasingly difficult to navigate when there are multiple operative forms of thermodynamic work being considered. To engineer stability in multi-parameter thermodynamic space, materials scientists have often turned to statistical approaches, such as Design of Experiments (DoE), Bayesian optimization with Gaussian processes, or other recent AI approaches in sequential learning.[6,7,8,9,10,11] These sequential learning algorithms are usually physics-agnostic, however, their efficiency and efficacy can be greatly improved by augmenting them with stronger thermodynamic priors on how to engineer relative stability.[12]

When considering relative stability, the most important feature of a thermodynamic phase diagram is the gradient of the phase boundary between the target phase and its competing phase(s). This is formulated in the Clausius-Clapeyron relation, which on a 2D temperature-pressure diagram is derived from $dG_\alpha = dG_\beta$; such that $-S_\alpha dT + V_\alpha dP = -S_\beta dT + V_\beta dP$; resulting in $dP/dT = \Delta S / \Delta V$. As shown in **Figure 3.1**, isothermally pressurizing a fluid usually enhances the relative stability of the solid—as $dP/dT > 0$, and $\Delta S_{S \rightarrow L} > 0$ while usually $\Delta V_{S \rightarrow L} > 0$. However, isothermally pressurizing H_2O preferences the stability of water over ice, as $\Delta V_{I \rightarrow W} < 0$, as water is denser than ice.

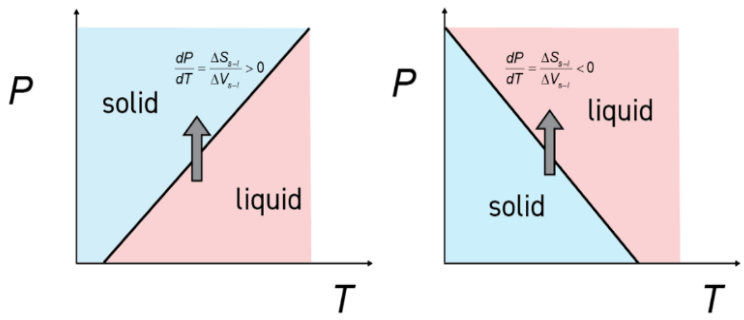

Figure 3.1: The gradient of a phase boundary determines the relative stability between two or more phases under changing thermodynamic conditions. **Left** shows an example where the solid is denser than liquid; whereas **Right** shows then liquid is denser than solid (like H_2O).

Beyond temperature and pressure considerations, a generalized Clausius-Clapeyron relation can be derived from a thermodynamic potential $dZ = -X_1 \mathrm{d}Y_1 - X_2 dY_2$, where Y_1 and Y_2 are intensive thermodynamic variables, which yields the equation $dY_1/dY_2 = -\Delta X_2/\Delta X_1$. Generalized Clausius-Clapeyron relations have been used to determine $\mathrm{d}T/\mathrm{d}H$ for magnetic materials,[13] dF/dT for shape-memory alloys,[14] and even $\mathrm{d}(p\mathrm{H})/\mathrm{d}\sigma$ for martensitic actuators in viruses.[15] The derivative form of the Clausius-Clapeyron equation also serves as a starting point to more complicated thermodynamic relations—for example by combining with Maxwell's relations or Bridgman's relations[16] to derive new thermodynamic partial derivatives for a variety of materials engineering applications.

Unfortunately, the derivative form of the Clausius-Clapeyron equation dY_1/dY_2 is not readily generalizable to higher-dimensional phase diagrams, as the phase-coexistence regions become higher-dimensional than a 1D line. For example, on a 4-dimensional phase diagram, one can have phase boundaries that are 0-, 1-, 2-, or 3-dimensional; corresponding to 5-, 4-, 3-, or 2-phase coexistence, respectively. For higher dimensional phase boundaries, it is not meaningful to write derivative-like expressions for gradients between three or more variables (such as dT/dP/dH/…/*etc.*); nor is it straightforward to arrive at such a ratio starting from $\mathrm{d}G_\alpha = \mathrm{d}G_\beta = \mathrm{d}G_\gamma = \ldots$ *etc.*

Here, we derive a vector representation of the Clausius-Clapeyron relation, which is readily generalizable to high-dimensional phase boundaries. We develop two representations of this relation: 1) a parametric representation for "bottom-up" construction of high-dimensional phase boundaries, where the phase boundaries are constructed from known or measured extensive variables of the competing phases; and 2) a Cartesian representation for "top-down" half-space intersections of high-dimensional free energy surfaces. Note that Clausius-Clapeyron analyses

only work on phase diagrams with all-intensive variables, which can be generally derived using the duality approach discussed in Part II of this three-part series. Because we are concerned with only the stability of a single target phase, phase diagrams with intensive natural variables are ideal to engineer relative stability while avoiding the complexities of heterogeneous equilibrium.

First, we demonstrate the bottom-up approach to the high-dimensional Clausius-Clapeyron relation by calculating the 2D phase boundary on a 3D temperature-pressure-magnetic field (*T*-*P*-*H*) phase diagram between BCC and FCC iron, using their known entropies, molar volumes, and magnetic moments. A major advantage of the Clausius-Clapeyron equation is that it does not require free energies, it only needs the extensive quantities of the two phases, which can often be easier to obtain than the temperature- and pressure-dependent Gibbs free energies of each phase. By knowing the high-dimensional gradient of the phase boundary, along with a single multi-phase coexistence point, the entire phase boundary can be constructed parametrically.

Next, we demonstrate the 'top-down' approach by calculating, visualizing, and interpreting a full 4D phase diagram. Specifically, we build a 4D Pourbaix diagram to examine the acid stability of manganese oxides, which have applications as earth-abundant oxygen evolution catalysts.[17,18] We extend the traditional *p*H and *E* axes in two additional dimensions to further account for nanoparticle size (1/R) and impurity ion concentration (μ_{K^+}). We focus our discussion on how to leverage the generalized Clausius-Clapeyron relation to navigate non-intuitive aspects of high-dimensional phase diagrams, from which we can derive meaningful insights to engineer relative materials stability.

3.2 Vector representation of the Clausius-Clapeyron Relation

We begin by rederiving the classic 2D Clausius-Clapeyron relation from a vector representation. On a *T*-*P* phase diagram, the Gibbs free-energy surface of a phase is $G = H' + PV$

– *TS*; where *H′* is the standard-state formation enthalpy of a phase, and *P′* = *P* – 1 atm (since *P* = 1 atm at standard state). This can be rewritten in Cartesian form such that *ax* + *by* + *cz* – *d* = *0* has a 1-to-1 mapping to the expression *ST* – *VP′* + *G* – *H′* = *0*. In our goal of calculating gradients, we treat *S* and *V* as constant at a given *T* and *P*, which linearizes the free-energy plane in the vicinity of a given phase coexistence point.

On the *T*–*P*–*G* axes, the normal vector of the free-energy plane can be expressed as $\langle S_i, -V_i, 1 \rangle$ where *i* represents the phase. **Figure 3.2** illustrates an example of the ice/water phase boundary at 273K and 2.16 MPa, with a table showing their corresponding entropies and molar volumes.[19] Between two phases, α and β, the normal vectors of their free-energy planes are n_α and n_β, and their cross product $n_\alpha \times n_\beta$ produces the differential vector for the phase coexistence line in *T*–*P*–*G* space:

$$\begin{vmatrix} T & P & G \\ S_\alpha & -V_\alpha & 1 \\ S_\beta & -V_\beta & 1 \end{vmatrix} = \langle V_\beta - V_\alpha,\ S_\beta - S_\alpha,\ V_\alpha S_\beta - S_\alpha V_\beta \rangle$$

where T, P, and G are unit vectors in the temperature, pressure and Gibbs free energy direction with their appropriate corresponding units. The parametric form of the 1D phase-coexistence line, *L*, in *G*(*T*,*P*) space can therefore be expressed as:

$$L_{Coexistence} = \langle T_0, P_0, G_0 \rangle + \langle \Delta V,\ \Delta S,\ V_\alpha S_\beta - S_\alpha V_\beta \rangle \lambda$$

where λ is the parameter, $\langle T_0, P_0, G_0 \rangle$ is an initial condition point. This form also produces an expression for $dG = V_\alpha S_\beta - S_\alpha V_\beta$ along the coexistence line, which does not appear in the traditional Clausius-Clapeyron relation.

By projecting this vector onto the *T*–*P* axes (in other words, eliminating the G term) and expressing this coexistence line in a parametric differential form, we recover the classical

Clausius-Clapeyron relation, $dT/dP = \Delta V/\Delta S$, rewritten in differential vector form as $\langle dT, dP \rangle = \langle \Delta V, \Delta S \rangle_{T,P} d\lambda$ where λ is the parameter. Importantly, to preserve the units of the T, P and G axes, λ must have units of [Temperature / Volume], which ensures for example that dT and λΔV both have units of temperature. More generally, the parameter λ has units of [Energy / ($[X_1][X_2]$)], where $[X_1]$ and $[X_2]$ are the units of the conjugate extensive variables X_1 and X_2.

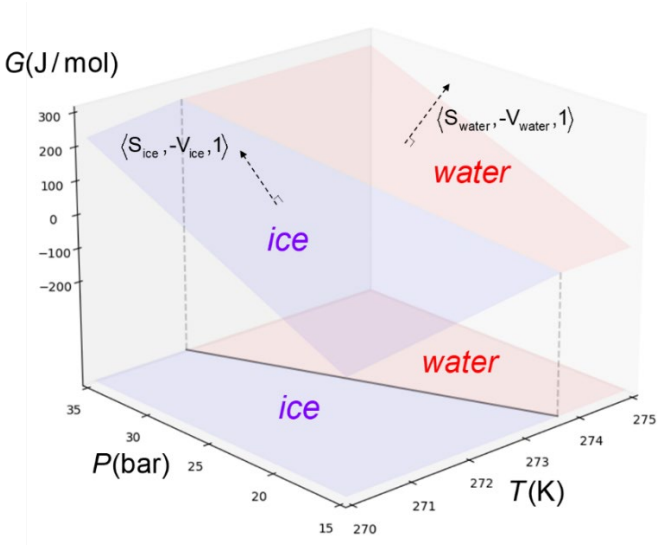

	T_0	P_0
Condition	273 K	2.16 MPa
	S (J/mol/K)	**V** (cm^3/mol)
Water	-2.558	17.19
Ice	-23.55	19.39
$\Delta X_{Water-Ice}$	20.99	-2.2

Figure 3.2: Vector representation of Clausius-Clapeyron relation for the ice-water coexistence boundary. The coexistence vector is given by the cross product of the normal vectors to each free-energy plane in $G(T,P)$ space.
Table 3.1: Molar entropies and volumes between water and ice at a given T_0, P_0 condition.

To construct a phase diagram, one generally requires the free-energies of all phases in a chemical system. However, obtaining free-energies may not always be possible or convenient. In a 'bottom-up' approach to the Clausius-Clapeyron relation, one can parametrically construct the entire phase boundary with just the extensive variables for all competing phases, plus one point of coexistence to anchor the phase boundary. The gradient of a phase boundary can be linearized by assuming the extensive variables are constant—this will apply for small perturbations in intensive conditions, but for curved phase boundaries one should recalculate the ΔX at other coexistence points.

3.2.1 3D phase diagram of temperature-pressure-magnetic field

On a high-dimensional phase diagram with all intensive axes, phase boundaries can be up to k-dimensional for any integer $k < d$, where d is the dimensionality of the phase diagram. This k-dimensional phase boundary represents phase coexistence between $(d - k)$ phases, and can be spanned by a linear combination of k one-dimensional Clausius-Clapeyron vectors, built from any two intensive variables. Here we offer an example of Vector representation of Clausius-Clapeyron relationships.

Consider the allotropic phase transformation between BCC and FCC iron. In addition to the temperature and pressure driven phases transformations between these two phases, BCC iron also has a higher magnetic moment than FCC Fe (2.2 μ_B vs 1.5 μ_B), so their phase boundary should also vary with the applied magnetic field. The thermodynamic potential for a single-component material with temperature, pressure, and magnetic field as natural variables is $dZ = -SdT + VdP - MdH$. This is a 4-dimensional free-energy space (1 energy axis and 3 work axes). By Generalized Gibbs' Phase Rule[20], $F = W - P + 1$. With 3 thermodynamic axes ($W = 3$) and two-phase coexistence ($P = 2$), the phase boundary between BCC and FCC iron has 2 intensive degrees-of-freedom ($F = 2$), meaning it is a 2-dimensional surface on the 3D T-P-H phase diagram.

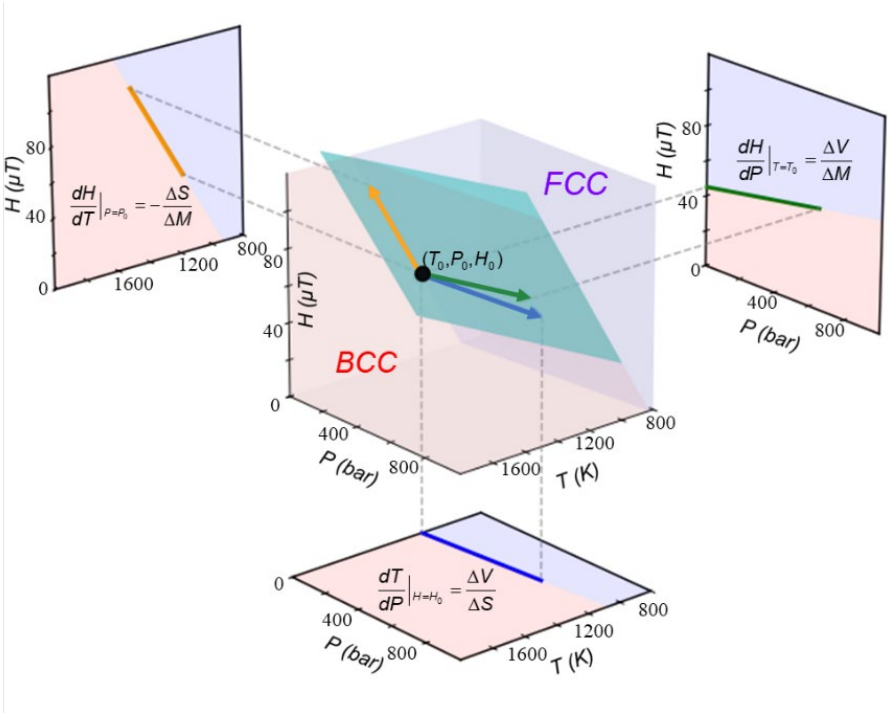

Figure 3.3: Clausius-Clapeyron relation on 3D phase diagram of temperature-pressure-magnetic field, showing a 2D phase boundary between ferromagnetic α-Fe (BCC) and paramagnetic γ-Fe (FCC). The gradient of this 2D phase boundary is constructed parametrically, taken from the linear combination of 2D Clausius-Clapeyron relations between *H*-*T*, *T*-*P*, or *H*-*P* axes. Blue is α-Fe (BCC) and red is γ-Fe (FCC).

Table 3.2: Molar entropies, volumes, and magnetic moments between BCC and FCC iron at a given T_0, P_0, H_0 condition.[21,22]

	T_0	P_0	H_0
Condition	1183 K	1 atm	0.45 μT
	S (J/mol/K)	**V** (cm^3/mol)	**M** (μ_B)
α-Fe (BCC)	27.28	7.37	2.2
γ-Fe (FCC)	27.97	7.30	1.5
$\Delta X_{FCC-BCC}$	0.69	-0.07	-0.7

Figure 3.3 illustrates the 2D phase boundary between FCC and BCC iron on the 3D *T*-*P*-*H* phase diagram. There are three possible 1D vectors for the 2D Clausius-Clapeyron relation:

$$\langle dT, dP, dZ \rangle_{dH=0} = \langle \Delta V, \Delta S, V_\alpha S_\beta - S_\alpha V_\beta \rangle_{T,P,H} \, d\lambda$$

$$\langle dT, dH, dZ \rangle_{dP=0} = \langle -\Delta M, \Delta S, S_\alpha M_\beta - M_\alpha S_\beta \rangle_{T,P,H} \, d\mu$$

$$\langle dP, dH, dZ \rangle_{dT=0} = \langle -\Delta M, -\Delta V, M_\alpha V_\beta - M_\beta V_\alpha \rangle_{T,P,H} \, d\nu$$

Where the units of the parameters are $\lambda \equiv$ [Temperature / Volume], $\mu \equiv$ [Temperature / Magnetic Moment], and $v \equiv$ [Energy / Volume / Magnetic Moment]. The 2-dimensional boundary between BCC and FCC Fe can be spanned by a linear combination of any two of these 1D vectors within this 4D space, such that the plane is expressed $P = P_0 + \alpha \mathbf{v}_1 + \beta \mathbf{v}_2$, where α and β are arbitrary parametric terms. As shown in the *T-P-H* phase diagram, only 2 of 3 possible Clausius-Clapeyron vectors are needed to span the 2D phase boundary. In higher dimensions, the number of required 1D vectors diminishes combinatorically.

3.3 Cartesian representation of Clausius-Clapeyron relationships

Thus far we have described a parametric vector approach to building high-dimensional phase boundaries, which are spanned by linear combinations of 1-dimensional Clausius-Clapeyron vectors. In this approach, we need as many 1D vectors as there are dimensions of the phase boundary. This approach is most applicable in experimental contexts with limited materials properties or phase equilibria data, or when rigorous free-energy descriptions of the relevant phases are unavailable. However, in the era of high-throughput computational materials science, the free energy surfaces of phases can be calculated computationally. The opportunity arises then to leverage these free energies to better understand phase equilibria in complex thermodynamic environments.

To this end, we next present an alternative "top-down" approach to analyze high-dimensional phase boundaries, which assumes the availability of free-energy data. This approach, which arrives at mathematically-equivalent descriptions of the phase boundary compared to the vector approach, identifies high-dimensional phase boundaries by calculating the half-space intersections of high-dimensional free-energy hyperplanes.

In an N-dimensional thermodynamic space (including the energy axis), the free-energy, Z, of a single phase can be represented in Cartesian form by

$$\sum_{i,d} X_i Y_i - Z = 0$$

In this case, a k-dimensional phase boundary can be calculated from the intersection of (N–k) hyperplanes from the N-dimensional thermodynamic space. For example, in a three-dimensional $G(T,P)$ space, the free-energy planes are two-dimensional, and a two-phase coexistence 1D line is given by the intersection of 2 hyperplanes. A three-phase coexistence 0D point is given by the intersection of 3 hyperplanes. This argument extends to higher-dimensions; e.g. two-phase coexistence is given by the intersection of two 4D hyperplanes, which results in a 3-dimensional phase boundary.

One can express these intersections by equating the hyperplane equations, for example, on a 4D phase diagram, three-phase coexistence between the phases α, β, γ is given on a 2D phase boundary, which can be written as $Z_\alpha = Z_\beta = Z_\gamma$:

$$\sum_i X_{i,\alpha} Y_i = \sum_i X_{i,\beta} Y_i = \sum_i X_{i,\gamma} Y_i$$

One major benefit of this Cartesian representation is that the Clausius-Clapeyron relationship for two-phase coexistence becomes simple to compute in high dimensions. In parametric form, a k-dimensional phase boundary needs to be spanned by k one-dimensional vectors, meaning for two-phase coexistence one needs (d–1) individual 1D Clausius-Clapeyron vectors. However, if one has the free-energy surfaces, one can directly compute any Clausius-Clapeyron derivative simply by calculating $dY_1/dY_2 = -\Delta X_2/\Delta X_1$, where the extensive variables X are parameters in the Cartesian free-energy expression.

The Cartesian representation of the generalized Clausius-Clapeyron relationship helps determine how one natural variable will change in relation to others in situations of multi-phase

coexistence and in higher dimensions. In **Chapter 3.4 – 3.6**, we demonstrate the coexistence of 1 to 5 phases within the *p*H-*E*-1/*R*-μ_K 4D Pourbaix diagram. All calculations are conducted using this Cartesian form. One of the key advantages of employing the Clausius-Clapeyron equation in this form is our ability to precisely calculate the dynamic relationships between different natural variables. By utilizing the materials' formation energies and extensive molar quantities, we are equipped to compute changes in an intensive natural variable relative to others under varying conditions at different number of phase coexistence. Here we offer some examples.

3.3.1 Single phase

As discussed in **Chapter II**, each single phase is characterized through a Legendre transformation, which is resolved by the intersection of half-spaces. We present the Pourbaix potential (Ψ) for each single phase, in relation to the four natural variables: *p*H, electrode potential (E), inverse temperature ($1/R$), and the chemical potential of potassium (μ_K). Within the *p*H-*E*-1/*R*-μ_K space, each phase is represented as a four-dimensional (4D) polytope:

$$\Psi = \frac{1}{N_m}\left((G_{bulk} - N_O\mu_{H_2O}) - RT\ln(10)(2N_O - N_H)\,p\mathrm{H} - (2N_O - N_H + Q)E + (\frac{A}{V})\gamma\eta\rho - N_K\mu_K \right)$$

3.3.2 2-phase coexistence

A 2-phase coexistence region in a 3D space is a 2D surface shared by two 3D polytopes, as shown in the chemical potential diagram of **Figure 3.4**. Similarly, a 2-phase coexistence region in a 4D space is a 3D interface shared by two 4D polytopes. Just as we are accustomed to presenting the equation of a 2D plane ($ax + by + cz + d = 0$) within a 3D space (defined by the coordinates x, y, and z), we can represent a 3D 2-phase coexistence region within a 4D space through a linear combination of the four natural variables:

$$[X_{pH}]_{\alpha-\beta} \cdot pH + [X_{\mu_K}]_{\alpha-\beta} \cdot \mu_K + [X_E]_{\alpha-\beta} \cdot E + [X_{1/R}]_{\alpha-\beta} \cdot \frac{1}{R} + [C]_{\alpha-\beta} = 0 \qquad \textbf{Eq. 3.1}$$

where $[X_{pH}]_{\alpha\text{-}\beta}$, $[X_{\mu K}]_{\alpha\text{-}\beta}$, $[X_E]_{\alpha\text{-}\beta}$, $[X_{1/R}]_{\alpha\text{-}\beta}$, $[C]_{\alpha\text{-}\beta}$ represent coefficient vectors – the conjugated variables of the four natural variables and a constant, their physical form is represented in **Table 3.6**. This approach simplifies the complex task of delineating phase coexistence in higher-dimensional spaces, making it more accessible for analysis and interpretation.

Thus, a vector of coefficients $[X_{pH}]_{\alpha\text{-}\beta}$, $[X_{\mu K}]_{\alpha\text{-}\beta}$, $[X_E]_{\alpha\text{-}\beta}$, $[X_{1/R}]_{\alpha\text{-}\beta}$, $[C]_{\alpha\text{-}\beta}$] can represent a 3D 2-phase coexistence in the 4D *p*H-*E*-1/*R*-μ_K space. Their values can be calculated by employing the condition $\Psi_\alpha = \Psi_\beta$ at the *α*-*β* phase coexistence. Consequently, the partial derivative between any two natural variables can be expressed as the ratio of the negative reciprocal of the corresponding two coefficients, such as $\partial \mu_K / \partial pH = -[X_{pH}]_{\alpha-\beta} / [X_{\mu_K}]_{\alpha-\beta}$.

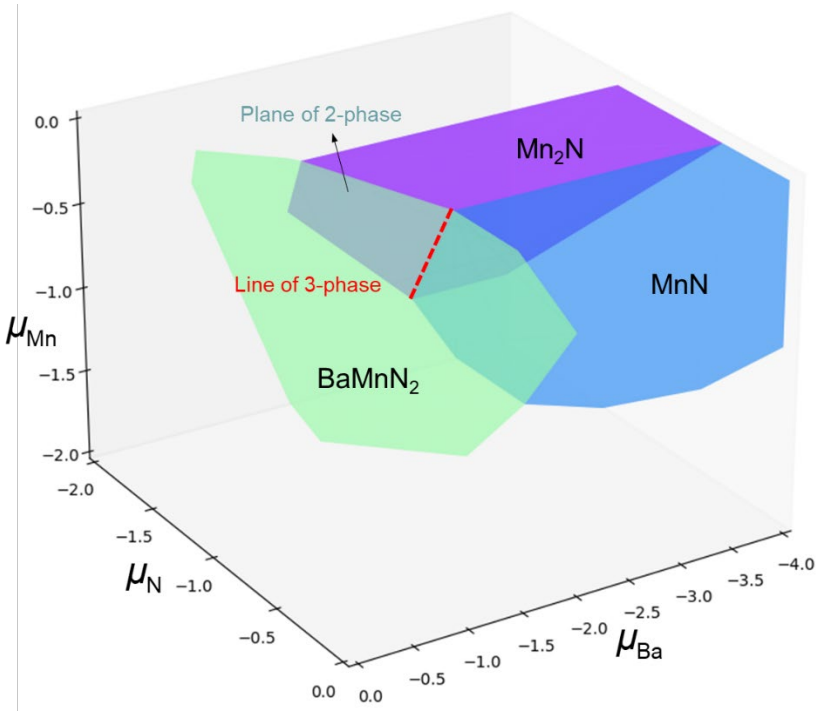

Figure 3.4: Chemical potential diagram of $BaMnN_2$, Mn_2N and MnN. The red dashed line represents the 3-phase coexistence region. The shared planes by two single phases are the 2-phase coexistence regions.

3.3.3 3-phase coexistence

For a ternary system in a 3D space, a 3-phase coexistence region is 1D, as shown as the red dashed line in **Figure 3.4**. Mathematically, a 2D 2-phase coexistence plane in this 3D space is $A \cdot \mu_{Ba} + B \cdot \mu_{Mn} + C \cdot \mu_N + D = 0$. We can use the Eq.3.2 and Eq.3.3 to represent the phase coexistence between $BaMnN_2 + Mn_2N$ and $MnN + Mn_2N$, respectively.

$$[X_{\mu Ba}]_1 \cdot \mu_{Ba} + [X_{\mu Mn}]_1 \cdot \mu_{Mn} + [X_{\mu N}]_1 \cdot \mu_N + [C]_1 = 0 \quad \textbf{Eq. 3.2}$$

$$[X_{\mu Ba}]_2 \cdot \mu_{Ba} + [X_{\mu Mn}]_2 \cdot \mu_{Mn} + [X_{\mu N}]_2 \cdot \mu_N + [C]_2 = 0 \quad \textbf{Eq. 3.3}$$

A 1D 3-phase coexistence line, is the intersection of two 2D 2-phase coexistence planes. So, the $BaMnN_2 + Mn_2N + MnN$ 3-phase coexistence line must simultaneously satisfy Eq.3.2 and Eq.3.3 simultaneously. Here, any variable can be eliminated by forming a linear combination of Eq.3.2 and Eq.3.3. For instance, by multiplying Eq.3.3 by $-[X_{\mu N}]_1/[X_{\mu N}]_2$ and adding it to Eq.3.2, we establish a linear relationship between μ_{Ba} and μ_{Mn}. Therefore, a line in a 3D space indicates that any two among the three natural variables share a linear relationship.

Similar statements are also valid for the 4D *p*H-*E*-1/*R*-μ_K space. Just like a 3-phase coexistence region in a 3D space is a 1D line; a 3-phase coexistence region in a 4D space is a 2D plane – the intersection of two 3D 2-phase coexistence polytopes (Eq.3.4 and Eq.3.5).

$$[X_{pH}]_1 \cdot pH + [X_{\mu_K}]_1 \cdot \mu_K + [X_E]_1 \cdot E + [X_{1/R}]_1 \cdot \frac{1}{R} + [C]_1 = 0 \quad \textbf{Eq. 3.4}$$

$$[X_{pH}]_2 \cdot pH + [X_{\mu_K}]_2 \cdot \mu_K + [X_E]_2 \cdot E + [X_{1/R}]_2 \cdot \frac{1}{R} + [C]_2 = 0 \quad \textbf{Eq. 3.5}$$

Again, any variable can be eliminated by linear combination of Eq.3.4 and Eq.3.5.Therefore, a 2D plane in a 4D space means any three among four natural variables has a linear relationship, which can be expressed by:

$$
\begin{aligned}
&[X_{p\mathrm{H}}]_1 \cdot p\mathrm{H} + [X_{\mu_K}]_1 \cdot \mu_K + [X_E]_1 \cdot E + [C]_1 = 0 \\
&[X_{p\mathrm{H}}]_2 \cdot p\mathrm{H} + [X_{\mu_K}]_2 \cdot \mu_K + [X_{1/R}]_2 \cdot {}^{1}\!/_{R} + [C]_2 = 0 \\
&[X_{p\mathrm{H}}]_3 \cdot p\mathrm{H} + [X_{1/R}]_3 \cdot {}^{1}\!/_{R} + [X_E]_3 \cdot E + [C]_3 = 0 \\
&[X_{1/R}]_4 \cdot {}^{1}\!/_{R} + [X_{\mu_K}]_4 \cdot \mu_K + [X_E]_4 \cdot E + [C]_4 = 0
\end{aligned}
\qquad \textbf{Eq. 3.6}
$$

Eq. 3.6 gives us four sets of coefficient vectors, where an example for Mn^{2+}+α-$K_{0.11}MnO_{1.94}$+δ-$K_{0.21}MnO_{1.87}$ 3-phase coexistence is shown in **Table 3.3**. From a Clausius-Clapeyron perspective, the four sets of coefficients can help us determine the change of an intensive variable as the change of another intensive variable under different fixed conditions. For example, under a fixed redox potential *E*, the relationship of pH and μ_K is $\partial\mu_K / \partial p\mathrm{H}\big|_E = -[X_{p\mathrm{H}}]_1 / [X_{\mu_K}]_1$ by Eq 6.1. And if particle radius R is assumed fixed, $\partial\mu_K / \partial p\mathrm{H}\big|_R = -[X_{p\mathrm{H}}]_2 / [X_{\mu_K}]_2$ by Eq 6.2. And if *R* and *E* are both fixed, based on Eq 6.3 and 6.4 pH and μ_K are fixed too. This means there are only two degrees of freedom for a 3-phase coexistence in a 4D phase diagram.

Table 3.3: Coefficient vectors of 3-phase coexistence among Mn^{2+}, α-$K_{0.11}MnO_{1.94}$ and δ-$K_{0.21}MnO_{1.87}$.

	A	**B**	**C**	**D**	**F**
Mn^{2+} + α-$K_{0.11}MnO_{1.94}$ + δ-$K_{0.21}MnO_{1.87}$	0	0.058	-0.040	0.506	0.297
	-0.120	0	-1.023	1.209	1.099
	0.005	0.060	0	0.478	0.265
	0.086	0.099	0.669	0	-0.280

3.3.4 4-phase and 5-phase coexistence

Similarly, a 4-phase (α, β, γ, δ) coexistence region is the intersection of three 3D 2-phase (α-β, β-γ, γ-δ) coexistence regions, which is a line. So, any two variables can be eliminated by linear combination of three 2-phase equations (Eq.3.1). Therefore, a 1D line in a 4D space means any two among four natural variables has a linear relationship. This requires $^2C_4$=6 equations to

represent this line. But we only need two vertices to represent this 4-phase coexistence line by using parametric for.

For a 5-phase coexistence region, it is a 0D point. Any three variables can be eliminated by linear combination of four 2-phase equations (Eq.3.1). It means any natural variables has a fixed value (the coefficients of other variables are 0).

3.4 Clausius-Clapeyron Analysis of a 4D Pourbaix Diagram

We conclude this work with a Clausius-Clapeyron analysis of a full 4-dimensional phase diagram. Our goal is to illustrate how the simultaneous consideration of multiple thermodynamic variables enables a more comprehensive approach to materials design and engineering. Although a 4D phase diagram stretches our imagination, it is still conceptually accessible by imagining the fourth dimension as time. While examining this 4D diagram, we will develop tools and intuition to mathematically conduct dimensional analogy to even higher-dimensional phase diagrams.

In particular, here we analyze the stability of manganese oxides under acidic conditions, with a goal to increase the stability of a solid manganese oxide relative to its dissolved Mn^{2+} aqueous ion. Energy storage and transformation technologies require new catalysts[23,24] for the oxygen reduction reaction (ORR) and oxygen evolution reaction (OER) [25,26], ideally without using expensive noble metal catalysts like platinum[27,28,29]. One candidate system is manganese oxide-based catalysts, however manganese oxides are generally not stable in acid electrochemical environments, where they easily decompose during changes in redox potential during cyclic voltammetry.[30,31,32]

There is a great diversity of manganese-based oxide materials, with various polymorphs and manganese oxidation states.[33,34,35] This raises the question of whether or not there exists a candidate manganese oxide phase that has good stability in acidic solutions. As illustrated on a

Pourbaix diagram, the relative stabilities of different manganese oxides vary as a function of aqueous *p*H and *E*. Furthermore, different surface energies between manganese oxide phases can drive nanoscale crossovers in polymorph stability,[33,36,37] and intercalation of impurity ions from solution such as K^+, Na^+, Ca^{2+}, *etc,* can also affect the bulk stability of various polymorphs.[33]

To capture all of these effects simultaneously, we construct here a four-dimensional Pourbaix diagram for the Mn-H_2O system with axes of *p*H, redox potential, nanoparticle size, and [K^+] impurity ion concentration. The composition- and size-dependent Pourbaix potential for each phase can be written as:

$$\Psi = \frac{1}{N_m}\left((G_{bulk} - N_O\mu_{H_2O}) - RT\ln(10)(2N_O - N_H)\,p\mathrm{H} - (2N_O - N_H + Q)E + (\frac{A}{V})\gamma\eta\rho - N_K\mu_K \right)$$

The derivation of this potential is provided in our previous works.[36,37] Here, Ψ is the Pourbaix potential, with respect to *p*H; redox potential, E; surface area to volume ratio, A/V; chemical potential of potassium, μ_K, under a constraint of water-oxygen equilibrium. N, is the number of atoms of a certain element; Q, is the number of charges; ρ, is volume density; η, is shape factor; μ_{H2O}, is water energy; μ_K, is surface energy. The number of Mn atoms are conserved in the phase transformations between Mn-based oxides with different compositions, thus Ψ is normalized by the number of Mn atoms, N_m. The molar Gibbs free energy of a phase, G_{bulk}, is its chemical potential, $\mu_i = \mu_i^o + RT\ln[a_i]$, where μ_i^o is given by the standard-state Gibbs formation free-energy, ΔG_f^o, and the activity ideally scales with the natural log of the metal ion concentration in solution.

In our analysis, we consider the phases: Mn^{2+}, MnO_4^-, Mn_3O_4, α-Mn_2O_3, *α*-MnOOH, *γ*-MnOOH, *α*-$K_{0.11}MnO_{1.94}$, *δ*-$K_{0.21}MnO_{1.87}$, *γ*-MnO_2 and *β*-MnO_2. The thermochemical data for these phases, including surface energies and K^+-intercalated energies, were calculated in our previous publications from DFT using the SCAN metaGGA functional.[38,39,40] Our thermochemical data used here is tabulated in the **Table 3.4.**

Table 3.4: Bulk Formation Energies, Surface Energies, Shape factors, Volume/Metal of K-Mn-O-H Phases

Phase	Formation energy	Surface energy	Shape factor	Volume/metal
Unit	eV/ formula	J/m^2	--	$Å^3/Mn$
R-MnO_2	-4.783	1.33	3.53	29.7
α-$K_{0.0625}MnO_2$	-5.03	1.19	5.35	33.8
α-$K_{0.11}MnO_{1.94}$	-5.6	1.19	5.35	33.8
α-$K_{0.125}MnO_2$	-5.364	1.19	5.35	33.8
α-$K_{0.166}MnO_2$	-5.52	1.19	5.35	33.8
α-$K_{0.25}MnO_2$	-5.764	1.19	5.35	33.8
α-Mn_2O_3	-9.132	1.19	5.35	33.8
α-MnO_2	-4.767	1.19	5.35	33.8
α-MnOOH	-5.763	1.19	5.35	33.8
β-MnO_2	-4.837	1.54	3.85	27.5
β-MnOOH	-5.629	1.54	3.85	27.5
δ-$K_{0.21}MnO_{1.87}$	-6.02	0.14	9.79	44.4
δ-$K_{0.33}MnO_2$	-5.988	0.14	9.79	44.4
δ-$K_{0.5}MnO_2$	-6.469	0.14	9.79	44.4
δ-$K_{0.75}MnO_2$	-6.894	0.14	9.79	44.4
δ-MnO_2	-4.558	0.14	9.79	44.4
γ-MnOOH	-5.964	0.84	6.09	33.5
γ-MnO_2	-4.787	0.84	6.09	33.5
Mn	0	--	--	--
MnO	-3.762	--	--	--
Mn_2O_3	-9.132	--	--	--
Mn_3O_4	-13.346	1.43	5.44	26.2
$Mn(OH)_2$	-6.198	0.47	5.69	43.5
$KMnO_2$	-7.313	--	--	--
Mn^{2+} (aq)	-2.363	--	--	--
MnO_4^- (aq)	-4.634	--	--	--
K^+ (aq)	-2.926	--	--	--
Mn^{3+} (aq)	-0.85	--	--	--
MnO_4^{2-} (aq)	-5.222	--	--	--

$Mn(OH)_3^-$ (aq)	-7.714	--	--	--
$MnOH^+$ (aq)	-4.198	--	--	--
$HMnO_2^-$ (aq)	-5.243	--	--	--

Because we are investigating the acid stability of solid manganese oxides, the relevant phase boundary is between each solid manganese oxide phase and its dissolved state, the Mn^{2+}(aq) ion. From a Clausius-Clapeyron perspective, we aim to increase the relative stability of the solid manganese oxide, meaning we need to determine how varying these 4 thermodynamic variables will shift the phase boundary of a manganese oxide solid into and towards the Mn^{2+}(aq) region, thereby enlarging the stability region of the solid. The relative stability analysis is then to find conditions where the Clausius-Clapeyron relation $dpH/dY < 0$; such that a change in Y shifts the phase boundary between Mn^{2+}(aq) vs. MnO_x(solid) to lower pH values, indicating increased acid stability.

3.4.1 Phase Coexistence on a High-Dimensional Phase Diagram

All the variables in the size-dependent Pourbaix potential are intensive, meaning that phase stability regions are all 4-dimensional stability polytopes—in other words, single-phase regions all have four intensive degrees of freedom. Phase coexistence boundaries all have $F = 5 - P$ degrees of freedom, where F is the dimensionality of the phase boundary and P is the number of coexisting phases, as summarized in **Table 3.5**. Some non-intuitive aspects of high-dimensional geometry emerge—for example, it is possible for three 4D single-phase regions to coexist on a 2D phase boundary; also, the phase boundary between two phases is 3-dimensional. These facts are difficult to visualize in our three-dimensional universe, but they are direct consequences of generalized Gibbs' phase rule.

Table 3.5: Formulas of Coexisting Phases and their Dimensionality of Phase Boundary.

P-phase coexistence	Dimensionality of Phase Boundary	Coexisting Phases
5	0 (vertex)	β-MnO_2, α-$K_{0.11}MnO_{1.94}$, δ-$K_{0.21}MnO_{1.87}$, Mn^{2+}, α-MnOOH
4	1 (line)	β-MnO_2, α-$K_{0.11}MnO_{1.94}$, δ-$K_{0.21}MnO_{1.87}$, Mn^{2+}
3	2 (polygon)	α-$K_{0.11}MnO_{1.94}$, δ-$K_{0.21}MnO_{1.87}$, Mn^{2+}
2	3 (polytope)	δ-$K_{0.21}MnO_{1.87}$, Mn^{2+}
1	4 (polytope)	δ-$K_{0.21}MnO_{1.87}$

To facilitate the visualization of these 4D phase stability regions and their corresponding phase boundaries, here we introduce the concepts of *slice* and *projection*, illustrated in **Figure 3.5**, which are two different approaches to dimensionality reduction for 2D or 3D visualization. To make a slice, an intensive variable is set to a constant value and the rest of the thermodynamic potential is evaluated. Slices essentially remove one dimension from the phase diagram. The other dimensionality reduction method is *projection*, which shows a 'shadow' of the phase on the thermodynamic axes, constructed by projecting all the vertices of the stability region onto the axes, and taking the geometric convex hull of the vertices. One limitation of the projection approach is that when projecting multiple phases, the 'shadows' of various phases can overlap. However, the advantage of the projection is that it reveals all the possible thermodynamic conditions a phase can exist; whereas one would typically have to construct slices sequentially over a thermodynamic axis to survey all the possible stability conditions of a phase. Once the domain of stability for a desired phase is determined from a projection approach, one can further apply slices to study materials stability to construct interpretable phase diagrams.

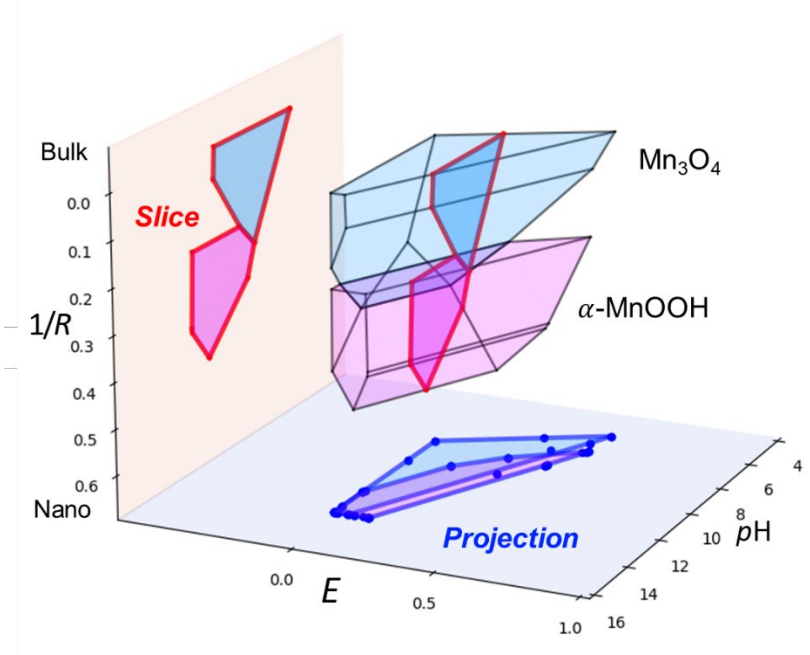

Figure 3.5: Phase stability region of Mn_3O_4 in 1/*R*, *E*, *p*H space. The plane bounded by red lines is a slice when E is fixed at 0.2V. The plane bounded by blue lines is a projection to *p*H -*E* space.

3.4.2 4D Pourbaix Diagram with pH, redox potential E, particle size 1/R, and impurity concentration μ_K

Figure 3.6 shows several different perspectives of our 4-dimensional Pourbaix diagram. Because we want to improve the acid stability of manganese oxides, we focus our diagrams on the solid manganese oxide phases that border the Mn^{2+}(aq) ion, which is the undesired dissolution product of solid manganese oxides in acid. **Figure 3.6a** shows the traditional 2D Pourbaix diagram for the Mn-H_2O system, which visualizes the bulk equilibrium phases under a given *E* and *p*H. The bulk equilibrium phase β-MnO_2 is only stable at low *p*H in a small range of high redox potentials.

For catalysts, it is often valuable to maximize the surface area to volume ratio. This provides the greatest amount of active catalytic area for a given mass of catalytic material. Not only does a high surface area to volume ratio promote the functional performance of a catalyst, a

variety of metastable manganese oxide phases can be stabilized at high surface-area-to-volume ratios—as demonstrated in previous experimental investigations[41,42,43,44], as well as our previous computational studies.[36] These metastable manganese oxides phases have lower surface energy than the bulk equilibrium phases, so at the nanoscale where surface-area-to-volume ratio is large, these bulk metastable phases can in fact become the nanoscale equilibrium phase.

In our previous work, we visualized nanoscale Pourbaix diagrams[36] using 2D slices of the (1/R) axis at fixed *E* or fixed *p*H. In this work, **Figure 3.6b** shows the full 3D nanoscale Pourbaix diagram, along with the competing nanoscale crossovers in polymorph stability. Size-stabilized bulk metastable manganese oxides include α-MnOOH, γ-MnOOH, δ-MnO_2 and R-MnO_2.

However, adding surface energy contributions to the free energy of a material always reduces its acid stability. This is because surface energy is always positive, meaning that a high (1/R) increases the free-energy of a solid; whereas the free energy of the Mn^{2+}(aq) ion does not change with (1/R). From a Clausius-Clapeyron formulation, this is written as

$$\frac{\partial p\mathrm{H}}{\partial(1/R)} = \frac{\Delta(\gamma\eta\rho)}{\Delta RT\ln(10)(2N_O - N_H)}$$

Because $\gamma_{solid} > 0$ and $\gamma_{Mn2+(aq)} = 0$, the phase boundary as a function of acid stability always destabilizes the solid phase.

As defined by the Pourbaix potential, each single phase is a 4D polytope in the *p*H-*E*-1/*R*-μ_K space. Within this framework, a 2-phase coexistence region, designated as α and β phase, is characterized by the condition $\Psi_\alpha = \Psi_\beta$, or equivalently, $\Delta\Psi_{\alpha-\beta} = 0$. **Table 3.6** shows for each intensive variable the difference in their conjugate extensive variables; for example, for *p*H this term would be $\Delta[-RT\ln(10)(2N_O-N_H)]$. From these coefficients, one can directly calculate the partial derivatives between any two natural variables, offering quantitative insight into how to

affect relative stability. An in-depth discussion on how to represent coexistence from 2 to 5 phases using the Cartesian form of the Clausius-Clapeyron relations is presented in **Chapter 3.3.2**.

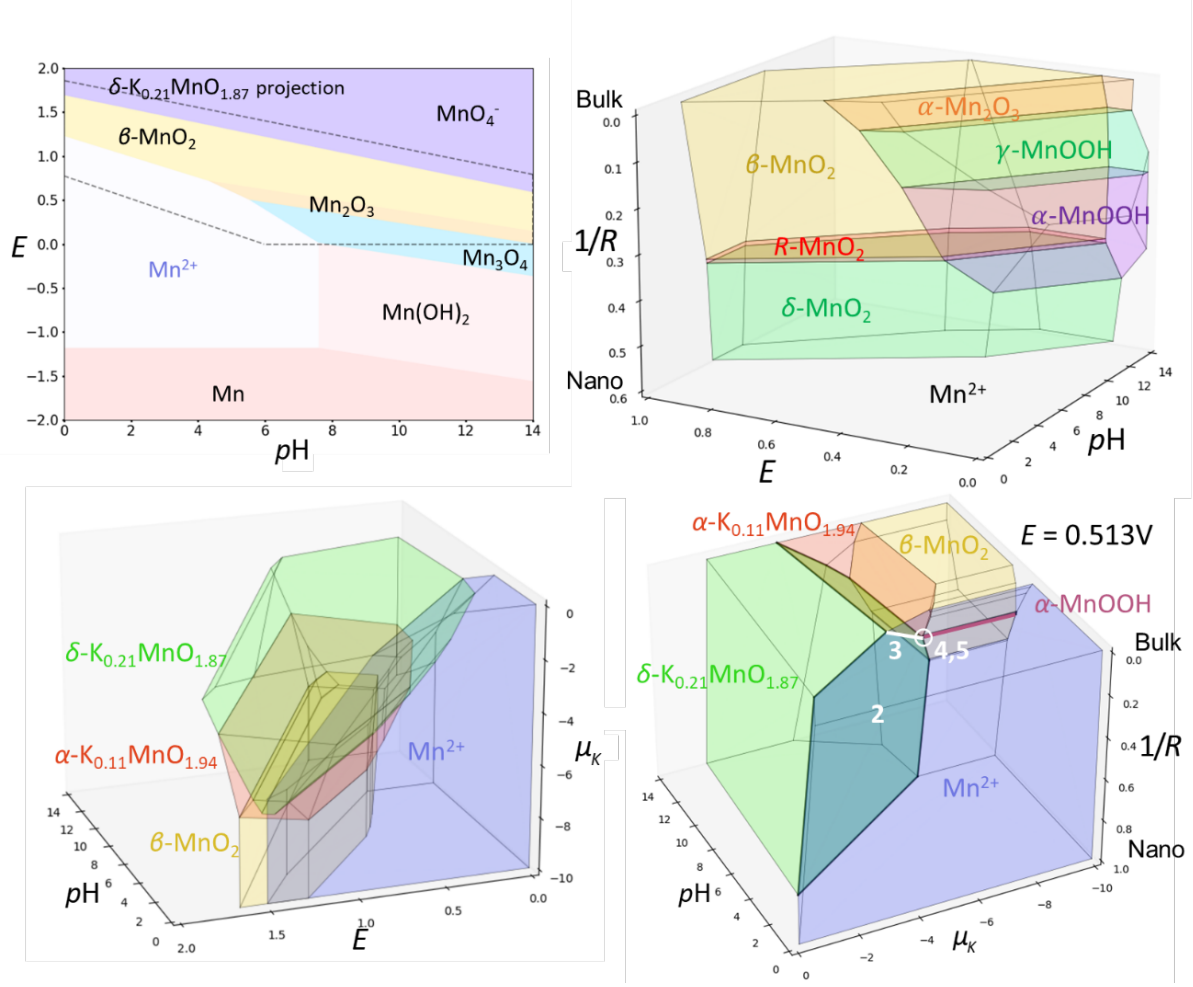

Figure 3.6: Projections and slices of a high dimensional Pourbaix diagram in *p*H-*E*-μ_K-1/*R* space of K-Mn-O-H system into lower dimensions. (a) Traditional Pourbaix diagram with E and *p*H as axis. (b) A slice of α-$K_{0.11}MnO_{1.94}$, δ-$K_{0.21}MnO_{1.87}$, β-MnO_2, Mn^{2+} when fixing E = 0.2 V. (c) A projection of δ-$K_{0.21}MnO_{1.87}$, δ-MnO_2, Mn^{2+} in pH-*E*-μ_K space. (d) A slice of α-$K_{0.11}MnO_{1.94}$, δ-$K_{0.21}MnO_{1.87}$, β-MnO_2, Mn^{2+} when fixing E = 1.2V. 2-phase coexistence regions are bounded by bold black lines.

Table 3.6: Coefficient vectors of 2-phase coexistence among Mn^{2+} and β-MnO_2, α-$K_{0.11}MnO_{1.94}$, δ-$K_{0.21}MnO_{1.87}$, α-MnOOH

Intensive variable	pH	μ_K	E	$1/R$	-
Conjugated extensive quantity	$\Delta[-RT\ln(10)(2N_O-N_H)]$	$-\Delta N_K$	$\Delta[-(2N_O-N_H+Q)]$	$\Delta(\gamma\eta\rho)$	$\Delta(G_{bulk}-N_O\mu_{H2O})$
Units	eV/Mn	eV/K_{atom}/Mn	eV/V/Mn	eV·nm/Mn	eV/Mn
β-MnO_2 + Mn^{2+}	0.105	0	0.886	-0.451	-1.090
α-$K_{0.11}MnO_{1.94}$ + Mn^{2+}	0.099	0.047	0.809	-0.578	-0.659
δ-$K_{0.21}MnO_{1.87}$ + Mn^{2+}	0.122	0.116	0.963	-0.210	-0.520
α-MnOOH + Mn^{2+}	0.125	0	0.707	-0.696	-1.139

On the other hand, when increasing the aqueous $[K^+]$ concentration in the system—which increases μ_K by $\mu_K = \mu^0_K + RT\ln([K^+])$—the phases cryptomelane, α-$K_{0.11}MnO_{1.94}$, and birnessite δ-$K_{0.21}MnO_{1.87}$ appear on the phase diagram, with a much larger stability region relative to pyrolusite β-MnO_2. This can be rationalized by the open crystal structures of α-MnO_2 and δ-MnO_2 phases, as α-MnO_2 Hollandite has 2×2 tunnel structures where intercalation of large K+ ions is energetically favorable, and similarly the δ-MnO_2 phase is a layered phase that also readily uptakes K^+. Intercalation of K^+ ions therefore stabilizes and lowers the bulk free energy of α- and δ- MnO_2, enlarging their stability windows. From a Clausius-Clapeyron formulation, this is written as

$$\frac{\partial pH}{\partial \mu_K} = -\frac{\Delta(N_K)}{\Delta RT\ln(10)(2N_O - N_H)}$$

The relative stability regions are visualized in the pH-E-μ_K space in **Figure 3.6c**. Notably, δ-$K_{0.21}MnO_{1.87}$ is stable within a relatively large redox potential window at low pH.

As an aside; if we were performing experiments to solve for the Clausius-Clapeyron relations, even if our ultimate goal were to understand the derivatives dpH/dY, we do not strictly

need to do this measurement. As discussed previously, by choosing 3 of the 6 possible ratios: $dp\mathrm{H}/dE$, $dp\mathrm{H}/d(1/\mathrm{R})$, $dp\mathrm{H}/d\mu_K$, $dE/d(1/\mathrm{R})$, $dE/d\mu_K$, or $d(1/\mathrm{R})/d\mu_K$—so long as all 4 variables are included—we can solve for the other three ratios.

3.4.3 Engineering relative stability in four dimensions

With the full four-dimensional Clausius-Clapeyron relation from **Table 3.6**, we can make holistic assessments on how to engineer relative materials stability along four thermodynamic axes dimensions. From the perspective of an acid-stable manganese oxide catalyst, there are two primary considerations: First, the material should be the equilibrium phase under operation conditions, which can be affected by all four variables E, *p*H, 1/R and μ_K. The second design consideration is from the perspective of acid-stability, where the phase boundary between the solid compound and Mn^{2+} should have a $dp\mathrm{H}/dY$ as negative as possible, for all considered intensive variables.

From these considerations, and from the manganese oxides in our dataset, the best acid-stable manganese oxide phase should be birnessite δ-K_xMnO_2. Of all the possible manganese oxide phases, δ-MnO_2 has the lowest surface energy due to its easily exfoliable 2D layered structure. This low surface energy means that the acid stability of δ-MnO_2 is least affected when increasing the surface area to volume ratio, for example by making low-dimensional nanoscale catalysts. From a functional perspective, catalysts rely on high surface area to volume ratios to maximize catalytic area, and δ-MnO_2 solubility increases the least at the nanoscale, compared to the other candidate MnO_x phases.

Moreover, under a high aqueous concentration of K^+ ions, both α-MnO_2 and δ-MnO_2 can favorably intercalate K+ and reduce their bulk free-energies, which further increases their acid stability. Although $dp\mathrm{H}/d\mu_K+$ is higher for α-MnO_2 than δ-MnO_2, α-MnO_2 is only stable in a

narrow [K^+] concentration, whereas at higher [K^+] concentrations δ-MnO_2 is the stable phase. Therefore, it is more robust to simply use a high excess concentration of [K^+] to stabilize the δ-MnO_2 polymorph, which increases the reliability and operational stability of this functional compound.

3.4.4 Three-, Four- and Five-Phase Coexistence

Gibbs' prediction of the triple-point on the temperature-pressure phase diagram; where solid, liquid and gas all coexist simultaneously; played a historical role in the adoption and establishment of chemical thermodynamics[45,46]. On higher-dimensional phase diagrams, three-phase coexistence is not only common, but an even greater number of possible coexisting phases is possible.

Designing conditions for multi-phase coexistence is promising in various functional devices. For example, photoelectrochemical water splitting[47], solid-state lithium-ion batteries[48], core-shell nanoparticle architectures[49] all rely on composite materials with hierarchical structures where there are multiple phases interacting with one another. Finding thermodynamic conditions for multiphase heterogeneous equilibrium can establish the long-term operational stability of such devices, which may otherwise degrade by undesired chemical reactions. In technologies that rely on phase transitions, such as multiferroric switching materials for transducers and information storage, finding a high-dimensional phase coexistence point may enable switching between more than two-states,[50] which could result in exciting new materials functionality.[51]

To illustrate 3- and 4-phase coexistence, we begin by analyzing **Figure 3.6d** as a representative 3D phase diagram. Here, with a fixed redox potential, Gibbs' Phase Rule is effectively the same as a diagram with just 3 intensive axes. In this case, two-phase coexistence is represented by 2D planes. The intersection of two planes (say, α+β and β+γ) produces a three-

phase coexistence line ($\alpha + \beta + \gamma$). The intersection of two three-phase coexistence lines then leads to a 4-phase coexistence point.

However, **Figure 3.6d** is not a 3D phase diagram, but rather, is a 3D slice of a 4D phase diagram at a fixed redox potential. When we vary the value of the redox potential slice, the 4-phase coexistence point moves in the *p*H, 1/R and μ_K directions; this represents a 1D line on the 4D phase diagram. An animation of the 4D phase diagram is provided in Supplementary Movie 1, where we use time to illustrate the fourth dimension. There is one special point in 4D space, where the 4D line terminates in conjunction with another 4D coexistence line. At this specific vertex, there is 5-phase coexistence. We can in fact visualize this special point by finding the precise redox potential where this 5-phase coexistence happens, which is at $E = 0.513$ V, which is the condition illustrated in Figure 4d. Therefore, the visualized 4D phase coexistence point on **Figure 3.6d** is in fact also a 5-phase coexistence point.

In **Table 3.7**, we provide explicit conditions for this 3-, 4- and 5-phase coexistence. These conditions are represented as vertices in 4D space. The 2-dimensional 3-phase coexistence boundary is fully defined by 3 vertices; and is spanned by any two of the 1D vectors that connect these 3 vertices. Similarly, the 1-dimensional 4-phase coexistence line is given by 2 vertices, and the 5-phase coexistence point is simply provided by its coordinates in 4D space.

Table 3.7: Three vertices of 3-phase coexistence among α-$K_{0.11}MnO_{1.94}$, δ-$K_{0.21}MnO_{1.87}$ and Mn^{2+}. Two vertices of 4-phase coexistence among β-MnO_2, α-$K_{0.11}MnO_{1.94}$, δ-$K_{0.21}MnO_{1.87}$ and Mn^{2+}. One vertex of 5-phase coexistence among β-MnO_2, α-$K_{0.11}MnO_{1.94}$,δ-$K_{0.21}MnO_{1.87}$, Mn^{2+} and γ-MnOOH.

	***p*H**	**μ_K**	***E***	**1/*R***
Three-phase coexistence Mn^{2+} +α-$K_{0.11}MnO_{1.94}$ + δ-$K_{0.21}MnO_{1.87}$	0	4.353	-1.120	0
	6.801	-4.906	0.323	0
	7.368	-6.763	0.513	0.211
Four-phase coexistence β-MnO_2 + α-$K_{0.11}MnO_{1.94}$ + δ-$K_{0.21}MnO_{1.87}$ + Mn^{2+}	-1.394	-6.170	1.513	0.234
	6.680	-6.732	0.553	0.222
Five-phase coexistence β-MnO_2 + α-$K_{0.11}MnO_{1.94}$ + δ-$K_{0.21}MnO_{1.87}$ + Mn^{2+} + α-MnOOH	7.368	-6.763	0.513	0.211

3.5 Evolution of Pourbaix diagrams

In this study, we employ a 4D Pourbaix diagram to analyze the relative stability utilizing Generalized Clausius-Clapeyron equations. Here, we will comprehensively explore Pourbaix diagrams, encompassing their four increasingly sophisticated derivations, with the final one being proposed for the first time in this dissertation. The Pourbaix diagram, named after Marcel Pourbaix, is a significant type of phase diagram illustrating the thermodynamic stability of different chemical species in an aqueous solution as a function of *p*H and redox potential *E*. Pourbaix diagrams find common applications in electrochemistry and corrosion science, aiding in predicting the stability of solid and ion phases in electrochemical aqueous environments. Essentially, they offer valuable insights into the electrochemical behavior of materials, facilitating understanding of their corrosion resistance, precipitation, and redox reactions.

3.5.1 Pourbaix diagrams from the Nernst equation

The genesis of Pourbaix diagrams can be attributed to the pioneering work of Marcel Pourbaix during the 1960s.[52,53] He laid the groundwork by employing the Nernst equation as a foundational principle. When a solid phase, *R*, is introduced into an electrochemical environment within an aqueous solution under controlled *p*H and redox potential *E* conditions, interactions at the interface between the solid phase and the surrounding solution occur. These interactions can initiate redox reactions, resulting in the generation of hydrogen ions and electrons and transformation of the solid phase *R* to product *P*. This process can be expressed as:

$$rR + w\mathrm{H_2O} \rightarrow pP + h\mathrm{H^+} + n\mathrm{e^-}$$

The Nernst equation serves as a powerful tool for relating each redox reaction, expressing the redox potential *E* as the sum of the standard potential E^0 and the logarithmic term of the reaction quotient, as shown in **Eq. 3.5.1**. The standard potential E^0 is determined from the reaction energy ΔG^0, the number of free electrons n, and Faraday's constant *F,* while the activity of products (a_p) and reactants (a_R) can be chosen based on the experimental setting.

$$\begin{aligned} E &= E^0 + \frac{0.0591}{n}\log\frac{(a_p)^p(a_{\mathrm{H^+}})^h}{(a_R)^r(a_{\mathrm{H_2O}})^w} \\ &= \frac{\Delta G^0}{nF} + \frac{0.0591}{n}\log\frac{(a_p)^p}{(a_R)^r} + \frac{[-0.0591h]}{n}\,p\mathrm{H} \end{aligned} \qquad \text{Eq. 3.5.1}$$

Therefore, the first two terms $\Delta G^0/nF$, $\frac{0.0591}{n}\log\frac{(a_p)^p}{(a_R)^r}$ in the **Eq. 3.5.1** become constants, thereby transforming each redox reaction into a linear function between the redox potential *E* and *p*H. Consequently, by identifying all relevant redox reactions for a given system, a Pourbaix diagram can be constructed. In a Pourbaix diagram, each line represents a distinct redox reaction, while the surrounding regions by lines represent the shared phase among corresponding reactions.

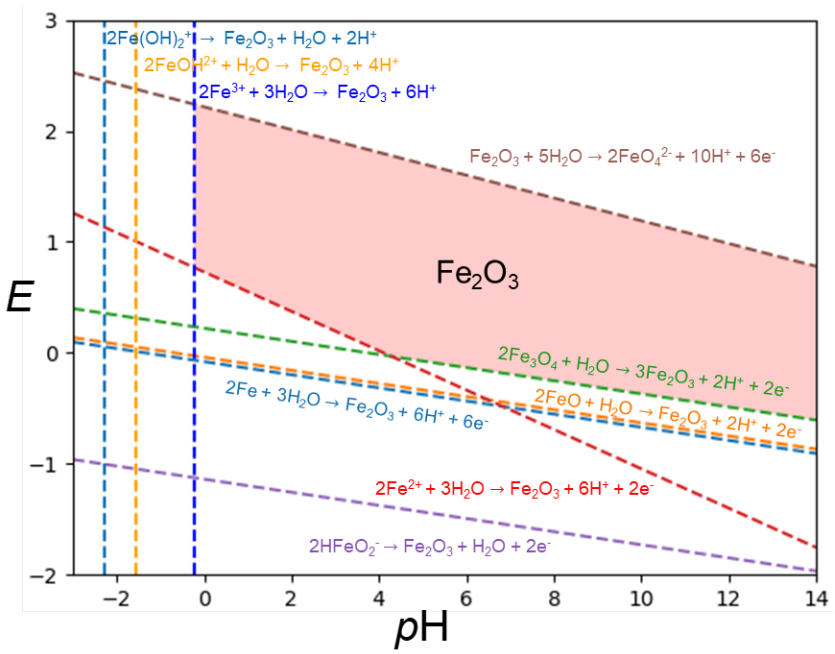

Figure 3.7: Fe_2O_3 stability region in a Pourbaix diagram constructed by the Nernst equation. Each colored line represents a redox reaction involving Fe_2O_3 either as a reactant or a product.

Figure 3.7 illustrates an example where we demonstrate the stability region of Fe_2O_3 by analyzing all feasible redox reactions involving Fe_2O_3 as either a reactant or a product. The reaction energies are sourced from Marcel Pourbaix's paper, with all ion activities assumed to be 1M. By extending this analysis to encompass all solid and ion phases within the Fe-O-H system, a comprehensive Fe-O-H Pourbaix diagram can be constructed.

This method presents a fundamental approach to constructing a Pourbaix diagram by leveraging various redox reactions within a system. This marks the first instance where scientists had the opportunity to observe a Pourbaix diagram, allowing for a thorough exploration of the material behavior under varying conditions of *p*H and *E*. However, its utilization is accompanied by certain disadvantages.

A notable drawback arises from the potential for an extensive number of redox reactions occurring in the system, particularly when dealing with multiple phases. For instance, Verink et al. incorporated only 3 solid phases in the development of the iron system's Pourbaix diagram, yet

encountered 28 redox reactions. Even with a limited number of phases, the number of possible redox reactions can be considerable, posing a significant challenge. When accounting for a larger number of phases, enumerating all stoichiometric redox reactions between reactants and products (${}_NC_2$ reactions) becomes laborious and time-consuming, particularly when scaling up to multicomponent systems. This complexity not only increases computational demands but also hampers the interpretation of the resulting diagram.

Furthermore, as shown by **Figure 3.7**, while not all redox reaction lines contribute to the final stability region of a specific phase, accurately identifying the relevant stability conditions requires a meticulous analysis of each redox reaction concerning the phase of interest. This manual identification process can be cumbersome and inefficient, relying heavily on visual inspection.

In summary, while the Nernst equation method offers a framework for constructing Pourbaix diagrams, its advantages are counterbalanced by the complexities associated with handling numerous redox reactions, making it challenging to apply efficiently in multicomponent systems.

3.5.2 Pourbaix diagrams from Grid-based free energy minimization

Recognizing the challenges associated with enumerating all redox reactions, developing a new approach to constructing Pourbaix diagrams based on materials, rather than reactions, is a promising direction. Huang et al.[54] introduced a methodology that involves the work of *p*H (W_{pH}) and *E* (W_E) applied on the material, $G = G^0 + W_{pH} + W_E$. This formulation facilitates the calculation of a new free energy value for each phase, allowing for direct manipulation of materials. Subsequently, a grid-based energy minimization technique is employed. This technique entails generating a dense numerical grid within a specified range of *E* and *p*H values. For each small grid, the phase with

the lowest free energy under the given electrochemical conditions is determined. This process is repeated for all grids to systematically construct the entire Pourbaix diagram.

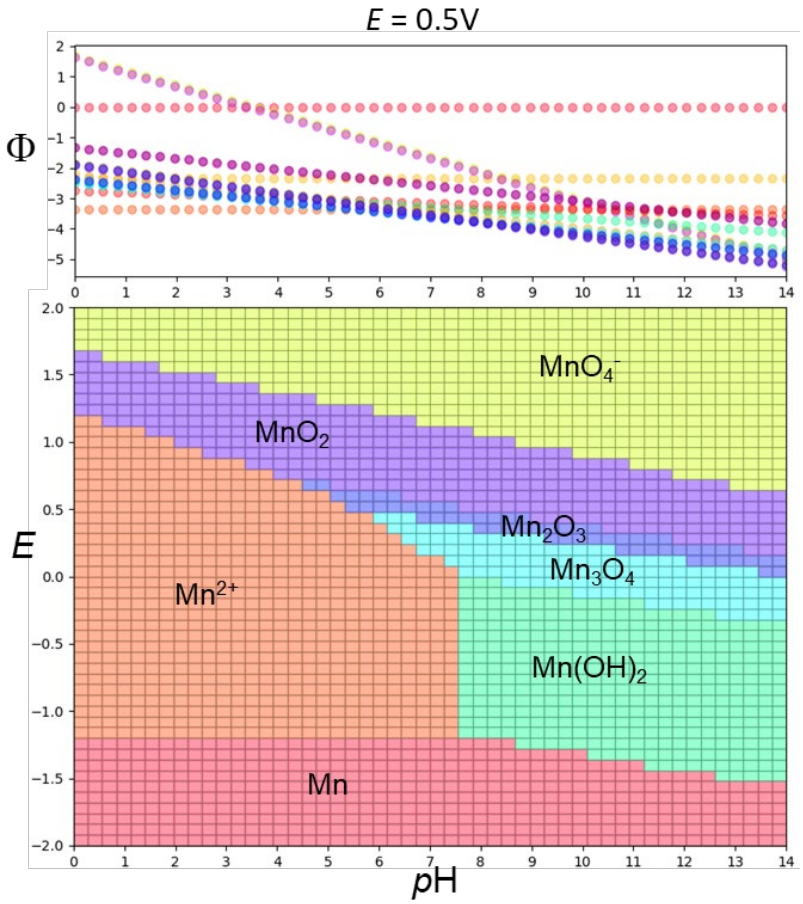

Figure 3.8: Pourbaix diagram for the Mn-O-H system obtained through a grid-based free energy minimization approach. a) Free energy of various phases across *p*H values when $E = 0.5$V. Dots of the same color represent identical phases. The final Pourbaix diagram highlights phases with the lowest free energy. b) the corresponding E-pH Pourbaix diagram.

Figure 3.8 shows the Pourbaix diagram of the Mn-O-H system constructed using the grid-based approach. The E – *p*H space, spanning a range of E from -2 to 2 V and pH from 0 to 14, is divided into a 50 * 50 grid. Within each grid, the free energy of various Mn phases is computed, with the phase possessing the lowest free energy representing the corresponding equilibrium phase. For example, **Figure 3.8a** illustrates the free energy of each grid at a fixed E value. Through

iterative calculations of the free energy across all grids for different phases, we generate the Pourbaix diagram as shown in **Figure 3.8b**.

Compared to Pourbaix diagrams from the Nernst equation, this method provides several advantages. Firstly, researchers can directly assess the stability of materials under varying electrochemical conditions, bypassing the need to enumerate individual redox reactions, which simplifies computations to some extent. Additionally, it allows for the estimation of the metastability of materials within the system, offering valuable insights into their stability by comparing to the equilibrium phases under the given electrochemical conditions.

However, despite these advantages, this method still presents challenges. The computational demands of material-based free energy minimization do not easily scale with the size of the grid, particularly when additional natural variables, controlled in experiments besides *p*H and *E*, are considered. As the system complexity increases, the number of grids grows exponentially, leading to longer computation times and increased resource requirements. For example, when considering an additional axis such as particle radius (1/R), the grid size increases from 50*50 to 50*50*50. In addition, at each grid point, the energies for all materials must be calculated, also resulting in a significant computational burden.

Furthermore, accurately determining phase boundaries can pose a challenge, as demonstrated by the phase boundary in **Figure 3.8b**. Despite the potential improvement in accuracy with an increased number of grids, achieving perfect calculation of a phase boundary using the grid approach is unattainable. Consequently, this method becomes progressively more laborious and resource-intensive, particularly in high-dimensional systems.

In summary, while the material-based free energy minimization approach offers advantages such as versatility and simplified conceptualization, its computational demands and

scalability limitations pose significant challenges, particularly in complex systems. Further advancements in computational techniques and algorithms may help mitigate these challenges and unlock the full potential for constructing Pourbaix diagrams.

3.5.3 Pourbaix diagrams from the Half-space intersection method

To extend the Pourbaix diagram to high-dimensional systems, efficient computational algorithms have been deployed to expedite the calculation process, often by introducing simplified assumptions. As discussed in **Chapter 2**, when traditional thermodynamic potentials become less convenient, the Legendre Transformation can be employed to consider additional forms of work and define a new thermodynamic potential. Sun et al.[36] have implemented Legendre Transformation to define a new Pourbaix potential, denoted as Ψ, which incorporates both chemical and electrical work:

$$\Psi = G^0 - \mu_H N_H - \mu_O N_O - EQ \qquad \text{Eq. 3.5.2}$$

Here, μ represents the chemical potential, Q is the charge number, and N is the particle number. Considering the aqueous nature of the system, the authors accounted for the hydrogen dissociation reaction ($H \leftrightarrow H^+ + e^-$) and the water-oxygen equilibrium ($H_2O \leftrightarrow 2H^+ + 1/2\ O_2 + 2e^-$). By incorporating these reactions, the relationship between μ_H, μ_O, pH, and E can be established as follows: $\mu_H = \mu_{H^+} - E$, $\mu_O = G_{H2O} - 2\mu_{H^+} + 2E$, where μ_{H^+} is related to pH by $\mu_{H^+} = -RT\cdot\ln(10)\cdot p\text{H}$, and G_{H2O} is the formation energy of water.

Substituting the aforementioned equations into the **Eq. 3.5.2**, the free energy Ψ can be expressed as a function of pH and E, resulting in a planar equation in Ψ-pH-E space for each phase:

$$\Psi = \frac{1}{N_m}\left((G_{bulk} - N_O\mu_{H_2O}) - RT\ln(10)(2N_O - N_H)\,p\text{H} - (2N_O - N_H + Q)E\right)$$

where *N* is the number of atom of certain element, G_{bulk} is the formation energy of the phase of interet. By plotting all the phase planes in this space, a lower envelope is formed, known as the half-space intersection. This envelope reveals the phases with the lowest free energy, thereby indicating their stability at the corresponding pH and E values. **Figure 3.9** illustrates a Pourbaix diagram in the Ψ-pH-E space for the Mn-O-H system. The upper free energy surface displays the half-space intersection, depicting phases with the lowest grand potential formed by different energy planes of phases.

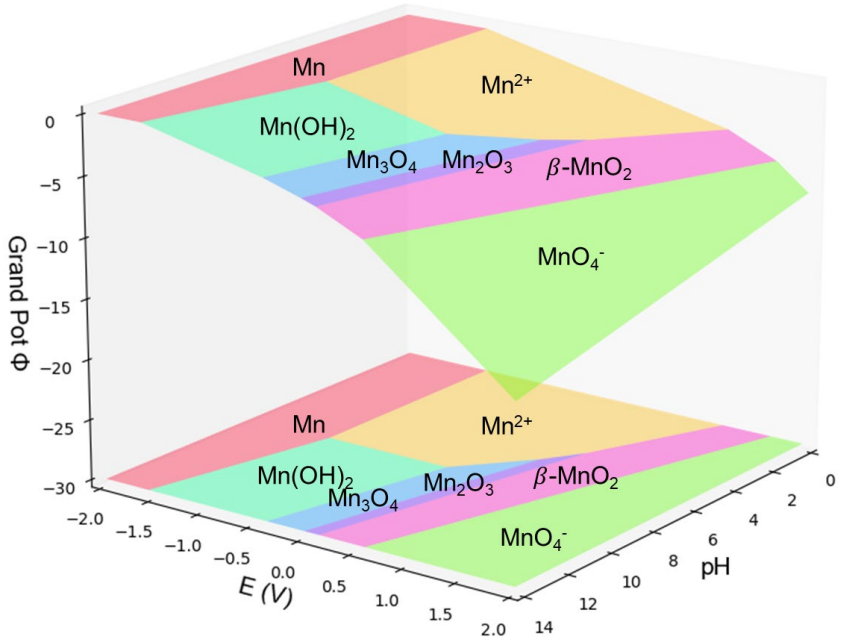

Figure 3.9: Pourbaix diagram of Ψ-*p*H-*E* space for Mn-O-H space using Half-space intersection method.

Similarly, Patel et al.[55] also utilized half-space intersection method. They employed the duality relationship between extensive and intensive space to construct a Pourbaix diagram for binary metal element systems. Their approach involved defining boundary conditions that account for closure versus metal element exchange and fixing the metal composition ratio. Subsequently, the half-space intersection method was utilized to generate the Pourbaix diagram.

Compared to the previous grid-based method, the half-space intersection technique represents a more efficient optimization approach, as it circumvents the computationally intensive task of comparing the energies of every material at each grid (**Figure 3.8a**). Instead, it traverses through each phase only once and utilizes a linear programming algorithm to identify the half-space intersection – identifying the phases with the lowest free energy, thereby significantly reducing the computational burden. This approach expedites the construction of high dimensional Pourbaix diagrams with additional natural variables, preparing for a more thorough exploration of electrochemical behavior in complex systems.

When the Half-space intersection method computationally enables the existence of high-dimensional Pourbaix diagrams, the Legendre Transformation provides a physically grounded thermodynamic foundation for effectively incorporating additional thermodynamic works into the Pourbaix potential, Ψ. While the conventional interpretation of the Pourbaix potential views it solely as a function of pH and E, its scope can be broadened by integrating other thermodynamic works, such as surface energy multiplied by surface area or chemical work in **Chapter 3.4**. This expansion enables the construction of size-dependent or composition dependent Pourbaix diagrams, offering valuable insights into materials' electrochemical behavior under diverse conditions.

Although the efficiency of Half-space intersection method, it operates under the linearization assumption (**Chapter 2.3.4.1**) that the free-energy of substances is usually modeled as stoichiometric line-compounds, whereas in reality, individual phases may exhibit their own composition domain and free energy curve. Another important drawback is that, the current derivation is limited to aqueous systems due to its reliance on the water-oxygen equilibrium, thereby restricting its applicability to other solvent systems, such as supercritical ammonia, or

organic solvents. Despite these limitations, leveraging the Legendre Transformation and integrating additional thermodynamic works into the Pourbaix potential can significantly enhance our understanding of electrochemical behavior across various materials and systems. Numerous studies have also demonstrated that linearization assumption is still possible to simulate real-life synthesis conditions and predict the stability of materials.

3.5.4 Pourbaix diagram as a slice of chemical potential diagram

Certain materials exhibit limited solubility or reactivity in aqueous environments, necessitating the use of alternative solvents for their synthesis. Inorganic syntheses often require organic solvents like ethanol, ether, dimethylformamide, etc. The choice of solvent can profoundly influence reaction kinetics and thermodynamics, leading to variations in the resulting products. For example, altering the solvent composition or polarity can affect the solvation of reactants and intermediates, thereby modulating the energy landscape of the reaction pathway. Furthermore, solvent environments can serve as reactive media, participating directly in chemical transformations to facilitate product formation. The synthesis of technologically important materials, such as gallium nitride (GaN) semiconductors, often relies on specialized solvent systems like supercritical ammonia, where the high chemical potential environment of ammonia enhances the growth and crystallization processes. Despite the extensive utilization of complex solvent systems in modern synthesis strategies, the lack of comprehensive phase diagrams or Pourbaix diagrams tailored to these solvent environments poses a challenge in effectively guiding and optimizing material synthesis. Integrating solvent-specific thermodynamic data and computational phase diagram framework could provide valuable insights into solvent-mediated reactions, enabling more informed design and control of material synthesis processes.

In this fourth derivation of Pourbaix diagram, we present a novel approach for deriving the Pourbaix diagram as a cross-section slice of the broader chemical potential landscape, a perspective not previously explored in literature. By leveraging the Legendre transformation equation in **Eq. 3.5.2**, with respect to chemical potentials and redox potential, we are able to construct a comprehensive 3D chemical potential diagram. This diagram, defined by axes representing the chemical potentials of oxygen (μ_O), hydrogen ions (μ_{H^+} or *p*H), and redox potential (*E*), a distinct chemical potential perspective on electrochemical reactions compared to the Pourbaix diagram (**Figure 3.10a**). Each material is represented as a 3D polytope in this diagram, offering a visual encapsulation of its energetic state within the given conditions.

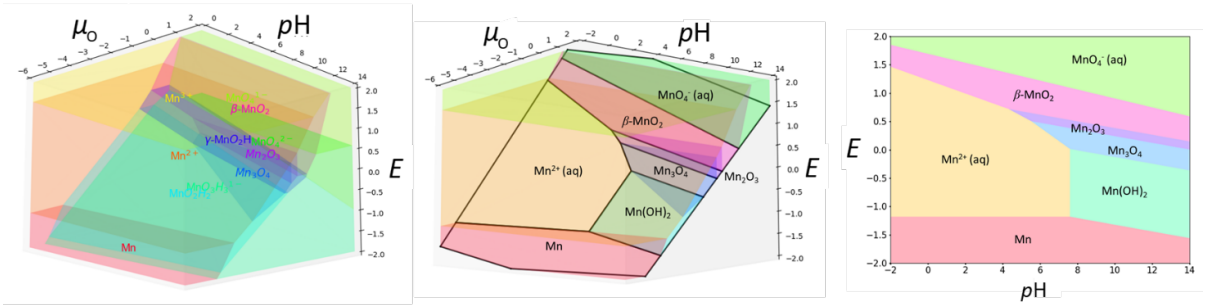

Figure 3.10: a) Chemical potential diagram of Mn system with μ_O, *p*H, *E* as axis. b) Water oxygen equilibrium slice on the chemical potential diagram. c) Projection of the slice information into *E* and *p*H dimension – the traditional Pourbaix diagram.

Then in aqueous solutions, we delve into the equilibrium between water and oxygen, a fundamental aspect of many electrochemical processes. Expressing this equilibrium relationship as $\mu_O = G_{H2O} - 2\mu_{H^+} + 2E$ elucidates a planar function within the μ_O-*p*H-*E* space. This function serves as a pivotal construct, delineating a slice of the chemical potential diagram that characterizes the water-oxygen equilibrium (**Figure 3.10b**). Furthermore, projecting this equilibrium slice onto the *E*-*p*H space extracts the traditional Pourbaix diagram in **Figure 3.10c**.

This fourth derivation, which involves constructing the Pourbaix diagram as a slice of the chemical potential diagram, inherits all the advantages of the half-space intersection method. By

embedding it within the broader context of the chemical potential landscape, we gain deeper insights into the thermodynamic underpinnings of electrochemical reactions. More importantly, another significant advantage of this approach lies in its adaptability to diverse solvent systems beyond aqueous environments. While the traditional Pourbaix diagram primarily addresses aqueous electrochemistry, our method extends its applicability to organic solvents and beyond. By incorporating the redox reactions of different solvents – the different slices within the chemical potential diagram, we can systematically derive other solvothermal Pourbaix diagrams.

3.5.5 Ethanol Pourbaix diagram

The fourth derivation of the Pourbaix diagram offers a method for constructing the Pourbaix diagram in various solvents. The key requirements encompass two aspects: a) the ability to identify a suitable equilibrium reaction within the respective solvent to derive a slice from the chemical potential diagram, and b) familiarity with the ion energies and solvent energies specific to the corresponding solvent. In this study, our objective is to analyze and present potential equilibrium reactions for the construction of phase diagram framework, deferring the calculation of thermodynamic data in different solvents to be addressed by others.

3.5.5.1 Identifying electrochemical equilibrium reaction for ethanol

Most literature on ethanol electrolysis focuses on aqueous ethanol solutions, typically with a 0.1M ethanol concentration. As demonstrated in Ahmed's[56] and Rakan's[57] paper, major products in the electrolysis of ethanol include CO_2, acetic acid, and acetaldehyde. The yield of these three products can be adjusted by varying the metal concentration in catalysts or by altering the redox potential E. CO_2 can become the major product with a high concentration of Pt catalyst, while acetic acid can dominate when PtRu is used as the catalyst. Acetaldehyde is rarely the major product, because in the presence of H_2O, CH_3CHO is easily oxidized to CH_3COOH. **Table 3.8**

below presents the electrochemical reactions and the corresponding chemical potential equilibrium for these three products.

Table 3.8: Electrochemical reactions of ethanol and corresponding chemical potential equilibrium.

Electrochemical reaction	Chemical potential equilibrium
$CH_3CH_2OH + 3H_2O \rightarrow 2CO_2 + 12e^- + 12\ H^+$	$G_{C2H5OH} + 3G_{H2O} = 2G_{CO2} - 12E + 12\mu_{H+}$
$CH_3CH_2OH \rightarrow CH_3CHO + 2e^- + 2H^+$	$G_{C2H5OH} = G_{CH3CHO} - 2E + 2\mu_{H+}$
$CH_3CH_2OH + H_2O \rightarrow CH_3COOH + 4e^- + 4H^+$	$G_{C2H5OH} + G_{H2O} = G_{CH3COOH} - 4E + 4\mu_{H+}$

In a pure ethanol solvent, there is no influence from water, rendering the electrochemical reaction singular. In Daisuke's[58] paper, 1,1-diethoxyethane (DEE) is selectively synthesized through the electrolysis of pure ethanol in a proton-exchange membrane (PEM) reactor. The synthesis mechanism includes electrochemical and non-electrochemical components. The electrochemical part involves the oxidation of ethanol to acetaldehyde, while the non-electrochemical part entails the reaction between acetaldehyde and ethanol to form DEE. Consequently, when choosing the electrochemical reaction for pure ethanol, it's essential to consider using $CH_3CH_2OH \rightarrow CH_3CHO + 2e^- + 2H^+$, with the corresponding chemical potential equilibrium expressed as $G_{C2H5OH} = G_{CH3CHO} - 2E + 2\mu_{H+}$. This choice is made because the subsequent non-electrochemical part is not influenced by the redox potential and *p*H.

Using this electrochemical equilibrium of ethanol, we construct an ethanol Pourbaix diagram. Our aim is to compare it to the aqueous Pourbaix diagram to glean insights into the experimental results of the solvothermal synthesis of Cu- and Co-oxide.

In the aqueous Pourbaix diagram, the associated equilibrium is the water-oxygen equilibrium, defined by $\Delta G_{H2O} = 1/2\ \mu_O - 2E + 2\mu_{H+}$. The formation energy of water, ΔG_{H2O}, is -2.4583 eV/atom under standard atmospheric conditions and room temperature (298.15K), as reported by Sun[36] and Persson[59]. Similarly, in ethanol, the electrochemical potential equilibrium

equation is expressed as $\Delta G_{C2H5OH} = \Delta G_{CH3CHO} - 2E + 2\mu_{H+}$. This necessitates the calculation of the formation energies of C_2H_5OH and CH_3CHO at the same temperature and pressure conditions. However, formation energy data for C_2H_5OH and CH_3CHO directly from the literature is not available.

Table 3.9: Formation enthalpy, absolute entropy and calculated formation energy of H_2O, C_2H_5OH, CH_3CHO.

	ΔH (KJ/mol)	S (J/mol*K)	ΔG (KJ/mol) at 298.15 K	ΔG (eV/atom) at 298.15 K
H_2O	-285.83	69.95	-237.14	-2.458
C_2H_5OH	-276	159.86	-172.71	-1.790
CH_3CHO	-196.4	117.3	-198.99	-2.062
C	0	5.833	–	–
H_2	0	130.68	–	–
O_2	0	205.152	–	–

ΔG_{H2O} can be calculated using the equation $\Delta G = \Delta H - T\Delta S$, where ΔH represents the formation enthalpy and ΔS represents the formation entropy, which refers to the change in enthalpy or entropy of the product relative to elemental reference states. If the $\Delta H - T\Delta S$ calculation yields the accurate value for ΔG_{H2O}, then we can utilize the same source data to compute ΔG_{C2H5OH} and ΔG_{CH3CHO}. The formation enthalpy (ΔH) and absolute entropy (S) data are accessible on the NIST website. **Table 3.9** shows the corresponding ΔH, S, and ΔG values for various materials. Notably, the calculated ΔG_{H2O} using data from the NIST website aligns closely with the reported value of -2.458 eV/atom. Therefore, I posit that it is reasonable to utilize the values of ΔG_{C2H5OH} = -1.790 eV/atom and ΔG_{CH3CHO} = -2.062 eV/atom.

3.5.5.2 Ethanol Pourbaix Diagram for Cu- and Co- oxides

The comparison between the aqueous and ethanol Pourbaix diagrams aims to elucidate the synthesis pathways of Cu- and Co- oxides. To streamline the analysis, the assumption is made that

the energy of solid in ethanol equals that in aqueous systems. Given the current constraints in calculating ion energies within organic solvents, the adoption of aqueous ion energies is chosen for simplicity. The consideration is restricted to simple ions such as Cu^{+}, Cu^{2+}, Co^{2+}, Co^{3+}. It is assumed that in organic solvents, the reduced solubility of metal oxides leads to the absence of complex off-stoichiometric ions. For the aqueous Pourbaix diagram, all ions, including complex ones (CuO_2^{2-}, $CuHO_2^{-}$, $CuOH^{+}$, $CoHO_2^{-}$), are still considered.

It is observed that copper-containing nitrate precursors in water yield CuO, while in ethanol, they result in the formation of $Cu_2(OH)_3NO_3$, Cu_2O, and ultimately Cu.[60] Comparing these findings to the aqueous Pourbaix diagram depicted in **Figure 3.11a**, it becomes evident that the stability region of CuO is considerably diminished in the ethanol Pourbaix diagram shown in **Figure 3.11b**. Conversely, Cu_2O exhibits a larger stability region across a broader pH range in ethanol. This disparity elucidates why CuO, which is observed to form in aqueous solutions, does not manifest in ethanol, with Cu_2O emerging instead. Notably, the Cu stability region (depicted in yellow) in **Figure 3.11b** predominates, indicating that Cu_2O formed in ethanol ultimately transitions to Cu.

For Co system, it forms Co_3O_4 in aqueous solution, whereas in ethanol, Co_3O_4 initially forms and eventually undergoes transformation to CoO at higher temperatures.[60] Despite Co_3O_4 not being represented in either the aqueous Pourbaix or ethanol Pourbaix diagrams (**Figure 3.11c** and **3.11d**), the distance of a phase from the Pourbaix slice plane serves as a crucial indicator of the feasibility of its synthesis. Remarkably, the aqueous Pourbaix slice exhibits a much closer proximity to the Co_3O_4 region compared to the ethanol Pourbaix slice. This observation explains the experimental transformation of Co_3O_4 to CoO in ethanol, but the stable existence of Co_3O_4 in aqueous solutions.

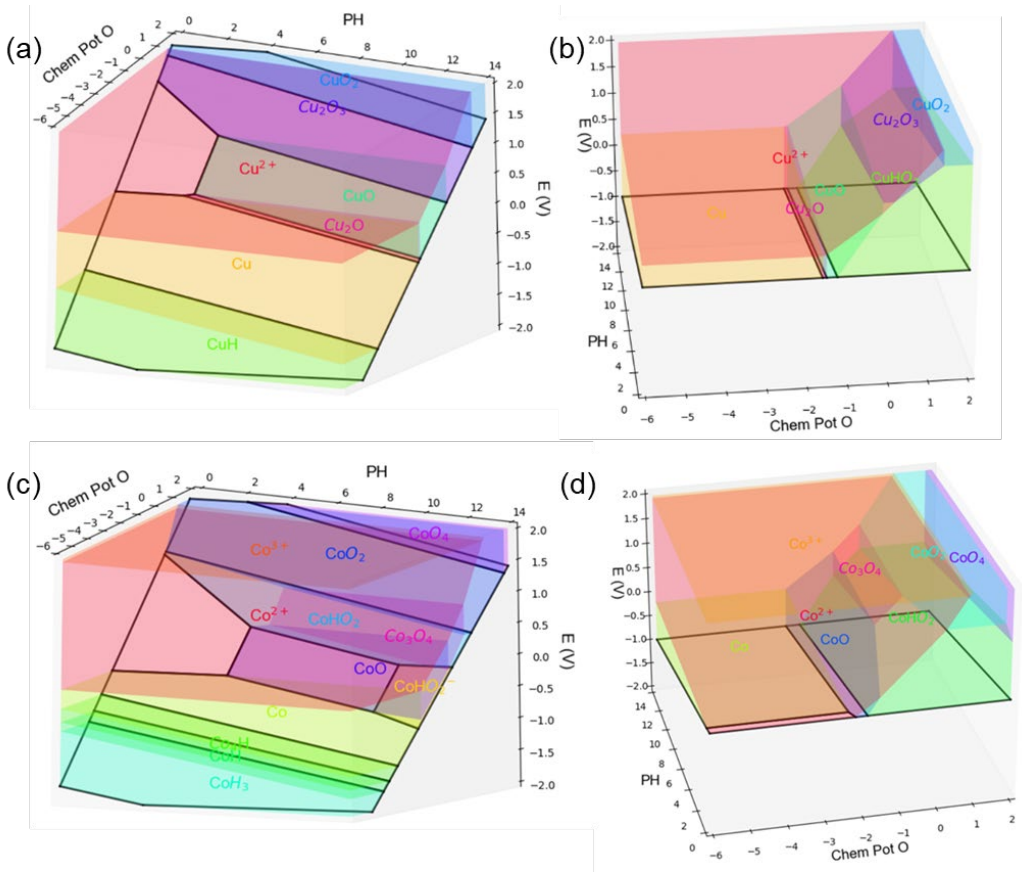

Figure 3.11: Comparison between aqueous and ethanol Pourbaix diagram. a) Cu aqueous Pourbaix diagram. b) Cu ethanol Pourbaix diagram. c) Co aqueous Pourbaix diagram. d) Co ethanol Pourbaix diagram.

3.5.6 Ammonia Pourbaix diagram

The synthesis of GaN in supercritical ammonia has garnered significant attention, because it offers advantages such as improved mass transport, reduced defect density, and enhanced control over crystal morphology, leading to the production of high-quality GaN materials.[61] While the synthesis of gallium nitride (GaN) in supercritical ammonia holds promise for advanced semiconductor development, it also presents significant challenges. One of the primary obstacles is the complex interplay of parameters required to achieve optimal crystal growth and quality under supercritical conditions. Balancing factors such as temperature, pressure, precursor concentration, and reaction kinetics is crucial for controlling nucleation and growth processes. However, the

literature lacks phase diagram tools to provide a deeper understanding of the chemical processes involved in GaN synthesis.

To overcome this challenge, we construct an ammonia Pourbaix diagram using our fourth derivation. Similar with the ethanol Pourbaix diagram, we operate under the assumption that the solid energy remains consistent across different solvents. Collaborating with my lab-mate, Joonsoo Kim, we can calculate the ion energy based on solubility and the Born model. In this dissertation, we present ion thermodynamic data in tabular form without delving into specific calculation details (**Table 3.10**). Then, the equilibrium between ammonia and nitrogen can be represented in a manner similar with the water-oxygen equilibrium. **Table 3.11** illustrates the electrochemical reactions and the corresponding chemical potential equilibrium.

Table 3.10: Formation energies of Ga^{3+} in different temperature of 100MPa supercritical ammonia. The energies are referenced to solid DFT energies in Materials Project

Temperature (K)	$\Delta G_f^\circ{}_{Ga^{3+}}$ [kJ/mol], pK offset = -14
693	-172.714
743	-195.935
793	-261.986
803	-273.642
848	-307.135
873	-324.023

Table 3.11: Electrochemical reactions of water and ammonia and corresponding chemical potential equilibrium.

Electrochemical reaction	Chemical potential equilibrium
$H_2O \rightleftharpoons 2H^+ + ½\ O_2 + 2e^-$	$G_{H2O} = 2\mu_{H+} + \mu_O - 2E$
$NH_3 \rightleftharpoons 3H^+ + ½\ N_2 + 3e^-$	$G_{NH3} = 3\mu_{H+} + \mu_N - 3E$

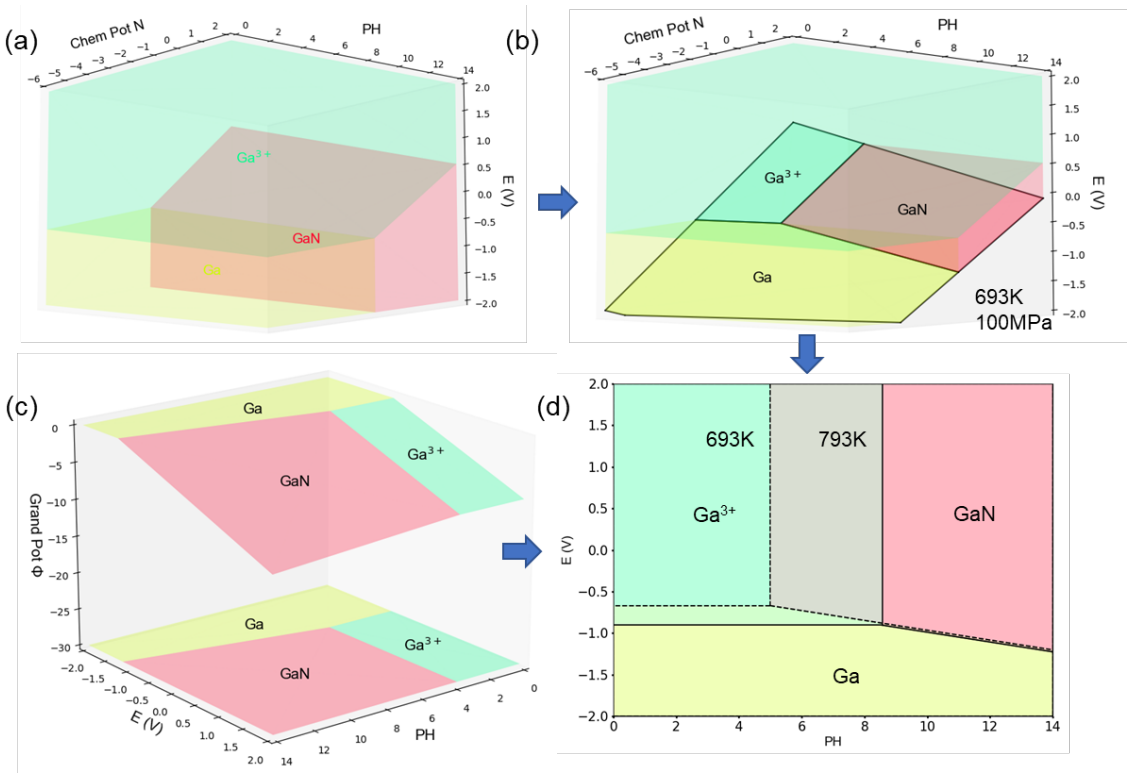

Figure 3.12: Ammonia Pourbaix diagram. a) Chemical potential diagram of Ga system with μ_N, *p*H, *E* as axis. b) Ammonia nitrogen equilibrium slice on the chemical potential diagram. c) Ammonia Pourbaix diagram with grand Pourbaix potential Ψ. d) Projection of the slice information into *E* and *p*H dimension – ammonia Pourbaix diagram.

By leveraging the Legendre transformation, we can define a ammonia Pourbaix potential Ψ, with respect to chemical potentials and redox potential, where

$$\overline{\psi} = \frac{1}{N_{Ga}}(G - \mu_N N_N - \mu_H N_H - Eq)$$

Figure 3.12a depicts the corresponding μ_N-*p*H-*E* chemical potential diagram, with GaN, Ga^{3+}, and Ga represented as 3D stability regions within the specified conditions. Based on the equilibrium between ammonia and nitrogen in supercritical ammonia, $\mu_N = G_{NH3} - 3\mu_{H+} + 3E$, providing the slice of the chemical potential diagram in **Figure 3.12b**. **Figure 3.12c** presents the slice information along with additional Pourbaix potential, illustrating the lower half-space intersection in free energy space. In **Figure 3.12d**, the projection of the slice into *E*-*p*H space reveals that with an increase in temperature from 693K to 793K, the relative stability of GaN decreases while the

stability region of Ga^{3+} expands. This observation aligns with the finding that GaN will dissolve at higher temperatures.

3.6 Outlook

In **Chapter 2**, we construct high dimensional diagrams with axes of intensive variables.[62,63] Since high-dimensional objects are so far removed from our everyday experience, phase diagram can be difficult to navigate even when they are constructed. It can also be laborious and expensive to build high-dimensional phase diagrams in full, as for each axis we need all the thermochemical properties of each phase.[64]

Our goal here was to explore more the properties of phase boundaries, which again, are the key geometric objects on a phase diagram. Importantly, the gradient of a phase boundary is enough to evaluate relative stability, such that one does not necessarily need to characterize all the thermochemical data in a system. This transforms us from a 'thermodynamic assessment' process, where we construct the full phase diagram at once, to a more flexible framework that is quicker to implement in real-world engineering situations. One only has to characterize the experimentally-obtained phase, and then use concepts of relative stability to shift the applied experimental conditions towards the direction of the phase we desire. As more undesired phases are observed, one can iteratively build towards a full description of the high-dimensional phase boundaries between a target phase and all its competing phases. This offers a practical (and practicable) pathway to optimize the synthesis or operation conditions of target functional materials.

Additionally, while **Chapter 2** delves into solid-state systems, this chapter concentrates on the solvothermal synthesis of inorganic materials, thoroughly exploring Pourbaix diagrams. We discuss four derivations of Pourbaix diagrams, illustrating how they become progressively more powerful by leveraging the advantages of previous derivations and overcoming their limitations.

Finally, we extend Pourbaix diagram exploration to non-aqueous environments, enabling researchers, for the first time, to utilize phase diagrams tailored specifically for supercritical ammonia and ethanol to guide their synthesis endeavors.

[1] Liu, Zi-Kui. "Computational thermodynamics and its applications." *Acta Materialia* 200 (2020): 745-792.

[2] Parakhonskiy, Gleb, et al. "Experimental pressure-temperature phase diagram of boron: resolving the long-standing enigma." *Scientific reports* 1.1 (2011): 96.

[3] Ansara, Ibrahim, et al. "Thermodynamic assessment of the Al-Ni system." *Journal of Alloys and Compounds* 247.1-2 (1997): 20-30.

[4] Chen, Ming, Bengt Hallstedt, and Ludwig J. Gauckler. "Thermodynamic assessment of the Co-O system." *Journal of Phase Equilibria* 24 (2003): 212-227.

[5] Okamoto, Hiroaki, and T. B. Massalski. "Thermodynamically improbable phase diagrams." *Journal of phase equilibria* 12 (1991): 148-168.

[6] Kusne, A. Gilad, et al. "On-the-fly closed-loop materials discovery via Bayesian active learning." *Nature communications* 11.1 (2020): 5966.

[7] Shields, Benjamin J., et al. "Bayesian reaction optimization as a tool for chemical synthesis." *Nature* 590.7844 (2021): 89-96.

[8] Szymanski, Nathan J., et al. "An autonomous laboratory for the accelerated synthesis of novel materials." *Nature* 624.7990 (2023): 86-91.

[9] MacLeod, Benjamin P., et al. "Self-driving laboratory for accelerated discovery of thin-film materials." *Science Advances* 6.20 (2020): eaaz8867.

[10] Ament, Sebastian, et al. "Autonomous materials synthesis via hierarchical active learning of nonequilibrium phase diagrams." *Science Advances* 7.51 (2021): eabg4930.

[11] Rohr, Brian, et al. "Benchmarking the acceleration of materials discovery by sequential learning." *Chemical science* 11.10 (2020): 2696-2706.

[12] Ghiringhelli, Luca M., et al. "Big data of materials science: critical role of the descriptor." *Physical review letters* 114.10 (2015): 105503.

[13] Yüzüak, Ercüment, et al. "Magnetic Energy Conversion." (2018).

[14] Liu, Yinong. "Thermodynamics of the shape memory effect in Ti–Ni alloys." *Shape memory alloys for biomedical applications*. Woodhead Publishing, 2009. 37-68.

[15] Olson, G. B., and H. Hartman. "Martensite and life: displacive transformations as biological processes." *Le Journal de Physique Colloques* 43.C4 (1982): C4-855.

[16] Bridgman, Percy W. "A complete collection of thermodynamic formulas." *Physical Review* 3.4 (1914): 273.

[17] Hong, Wesley T., et al. "Toward the rational design of non-precious transition metal oxides for oxygen electrocatalysis." *Energy & Environmental Science* 8.5 (2015): 1404-1427.

[18] Peng, Jiayu, et al. "Stability Design Principles of Manganese-Based Oxides in Acid." *Chemistry of Materials* 34.17 (2022): 7774-7787.

[19] Journaux, Baptiste, et al. "Holistic approach for studying planetary hydrospheres: Gibbs representation of ices thermodynamics, elasticity, and the water phase diagram to 2,300 MPa." *Journal of Geophysical Research: Planets* 125.1 (2020): e2019JE006176.

[20] Sun, Wenhao, and Matthew J. Powell-Palm. "Generalized Gibbs' Phase Rule." *arXiv preprint arXiv:2105.01337* (2021).

[21] Magomedov, Makhach Nasrutdinovich. "Changes in the properties of iron during BCC–FCC phase transition." *Physics of the Solid State* 63 (2021): 215-222.

[22] Ruban, Andrei V., Anatoly B. Belonoshko, and Natalia V. Skorodumova. "Impact of magnetism on Fe under Earth's core conditions." *Physical Review B* 87.1 (2013): 014405.

[23] Seh, Zhi Wei, et al. "Combining theory and experiment in electrocatalysis: Insights into materials design." *Science* 355.6321 (2017): eaad4998.

[24] Hwang, Jonathan, et al. "Perovskites in catalysis and electrocatalysis." *Science* 358.6364 (2017): 751-756.

[25] Bullock, R. Morris, et al. "Using nature's blueprint to expand catalysis with Earth-abundant metals." *Science* 369.6505 (2020): eabc3183.

[26] Wei, Chao, et al. "Recommended practices and benchmark activity for hydrogen and oxygen electrocatalysis in water splitting and fuel cells." *Advanced Materials* 31.31 (2019): 1806296.

[2727] Seh, Zhi Wei, et al. "Combining theory and experiment in electrocatalysis: Insights into materials design." *Science* 355.6321 (2017): eaad4998.

[28] Hwang, Jonathan, et al. "Perovskites in catalysis and electrocatalysis." *Science* 358.6364 (2017): 751-756.

[29] Rao, Karun K., et al. "Overcoming Hurdles in Oxygen Evolution Catalyst Discovery via Codesign." *Chemistry of Materials* 34.3 (2022): 899-910.

[30] Huynh, Michael, D. Kwabena Bediako, and Daniel G. Nocera. "A functionally stable manganese oxide oxygen evolution catalyst in acid." *Journal of the American Chemical Society* 136.16 (2014): 6002-6010.

[31] Li, Ailong, et al. "Stable potential windows for long-term electrocatalysis by manganese oxides under acidic conditions." *Angewandte Chemie* 131.15 (2019): 5108-5112.

[32] Moreno-Hernandez, Ivan A., et al. "Crystalline nickel manganese antimonate as a stable water-oxidation catalyst in aqueous 1.0 MH 2 SO 4." *Energy & Environmental Science* 10.10 (2017): 2103-2108.

[33] Kitchaev, Daniil A., et al. "Thermodynamics of phase selection in MnO2 framework structures through alkali intercalation and hydration." *Journal of the American Chemical Society* 139.7 (2017): 2672-2681.

[34] Robinson, David M., et al. "Photochemical water oxidation by crystalline polymorphs of manganese oxides: structural requirements for catalysis." *Journal of the American chemical Society* 135.9 (2013): 3494-3501.

[35] Stobbe, ER D., B. A. De Boer, and J. W. Geus. "The reduction and oxidation behaviour of manganese oxides." *Catalysis Today* 47.1-4 (1999): 161-167.

[36] Sun, Wenhao, et al. "Non-equilibrium crystallization pathways of manganese oxides in aqueous solution." *Nature communications* 10.1 (2019): 1-9.

[37] Chen, Bor-Rong, et al. "Understanding crystallization pathways leading to manganese oxide polymorph formation." *Nature communications* 9.1 (2018): 1-9.

[38] Sun, Jianwei, Adrienn Ruzsinszky, and John P. Perdew. "Strongly constrained and appropriately normed semilocal density functional." *Physical review letters* 115.3 (2015): 036402.

[39] Kitchaev, Daniil A., et al. "Energetics of MnO 2 polymorphs in density functional theory." *Physical Review B* 93.4 (2016): 045132.

[40] Yang, Julia H., Daniil A. Kitchaev, and Gerbrand Ceder. "Rationalizing accurate structure prediction in the meta-GGA SCAN functional." *Physical Review B* 100.3 (2019): 035132.

[41] Birkner, Nancy, and Alexandra Navrotsky. "Rapidly reversible redox transformation in nanophase manganese oxides at room temperature triggered by changes in hydration." *Proceedings of the National Academy of Sciences* 111.17 (2014): 6209-6214.

[42] Navrotsky, Alexandra, et al. "Nanophase transition metal oxides show large thermodynamically driven shifts in oxidation-reduction equilibria." *Science* 330.6001 (2010): 199-201.

[43] Birkner, Nancy, and Alexandra Navrotsky. "Thermodynamics of manganese oxides: Sodium, potassium, and calcium birnessite and cryptomelane." *Proceedings of the National Academy of Sciences* 114.7 (2017): E1046-E1053.

[44] Birkner, Nancy, and Alexandra Navrotsky. "Thermodynamics of manganese oxides: Effects of particle size and hydration on oxidation-reduction equilibria among hausmannite, bixbyite, and pyrolusite." *American Mineralogist* 97.8-9 (2012): 1291-1298.

[45] Van Klooster, H. S. "Bakhuis Roozeboom and the phase rule." *Journal of Chemical Education* 31.11 (1954): 594.

[46] Caldi, Daniel G., and George D. Mostow, eds. *Proceedings of the Gibbs Symposium: Yale University, May 15-17, 1989*. American Mathematical Soc., 1990.

[47] Liu, Jiao, et al. "Surface-phase junctions of branched TiO2 nanorod arrays for efficient photoelectrochemical water splitting." *Applied Catalysis B: Environmental* 158 (2014): 296-300.

[48] Richards, William D., et al. "Interface stability in solid-state batteries." *Chemistry of Materials* 28.1 (2016): 266-273.

[49] Chu, Fukai, et al. "Hierarchical core–shell TiO2@ LDH@ Ni (OH) 2 architecture with regularly-oriented nanocatalyst shells: Towards improving the mechanical performance, flame retardancy and toxic smoke suppression of unsaturated polyester resin." *Chemical Engineering Journal* 405 (2021): 126650.

[50] Liu, Z. K., Xinyu Li, and Q. M. Zhang. "Maximizing the number of coexisting phases near invariant critical points for giant electrocaloric and electromechanical responses in ferroelectrics." *Applied Physics Letters* 101.8 (2012): 082904.

[51] Wei, Yanping, et al. "Four-state memory based on a giant and non-volatile converse magnetoelectric effect in FeAl/PIN-PMN-PT structure." *Scientific Reports* 6.1 (2016): 30002.

[52] Pourbaix, M., Zhang, H. & Pourbaix, A. Presentation of an Atlas of chemical and electrochemical equilibria in the presence of a gaseous phase. *Mater. Sci. Forum* 251–254, 143–148 (1997).

[53] VERINK, E. D. Simplified Procedure for Constructing Pourbaix Diagrams. *Corrosion* 23, 371–373 (1967).

[54] Huang, L. F. & Rondinelli, J. M. Electrochemical phase diagrams for Ti oxides from density functional calculations. *Phys. Rev. B - Condens. Matter Mater. Phys.* 92, 1–13 (2015).

[55] Patel, A. M., Nørskov, J. K., Persson, K. A. & Montoya, J. H. Efficient Pourbaix diagrams of many-element compounds. *Phys. Chem. Chem. Phys.* 21, 25323–25327 (2019).

[56] Ali, Ahmed H., and Peter G. Pickup. "Electrolysis of Ethanol and Methanol at PtRu@ Pt Catalysts." *Journal of The Electrochemical Society* 169.3 (2022): 034523.

[57] Altarawneh, Rakan M., and Peter G. Pickup. "Product distributions and efficiencies for ethanol oxidation in a proton exchange membrane electrolysis cell." *Journal of The Electrochemical Society* 164.7 (2017): F861.

[58] Kawaguchi, Daisuke, Hitoshi Ogihara, and Hideki Kurokawa. "Upgrading of Ethanol to 1, 1-Diethoxyethane by Proton-Exchange Membrane Electrolysis." *ChemSusChem* 14.20 (2021): 4431-4438.

[59] Persson, Kristin A., et al. "Prediction of solid-aqueous equilibria: Scheme to combine first-principles calculations of solids with experimental aqueous states." *Physical Review B* 85.23 (2012): 235438.

[60] Broge, Nils Lau Nyborg, et al. "Mapping the redox chemistry of common solvents in solvothermal synthesis through in situ X-ray diffraction." *Nanoscale* 12.15 (2020): 8511-8518.

[61] Dwiliński, R., et al. "GaN synthesis by ammonothermal method." *Acta Physica Polonica A* 88.5 (1995): 833-836.

[62] Sun, Wenhao, and Matthew J. Powell-Palm. "Generalized Gibbs' Phase Rule." arXiv preprint arXiv:2105.01337 (2021).

[63] Chen, Jiadong, Matthew J. Powell-Palm, and Wenhao Sun. "The geometry of high-dimensional phase diagrams: II. The duality between closed and open chemical systems." *arXiv preprint arXiv:2404.05197* (2024).

[64] Chen, Jiadong, Matthew J. Powell-Palm, and Wenhao Sun. "The geometry of high-dimensional phase diagrams: III. Engineering relative stability in four dimensions." *arXiv preprint arXiv:2404.05201* (2024).

Chapter 4 Navigating Phase Diagram Complexity to Guide Robotic Synthesis

4.1 Challenges in designing efficient synthesis recipes

There is currently a poor scientific understanding of how to design effective and efficient synthesis recipes to target inorganic materials.[1,2,3] As a result, synthesis often becomes a bottleneck in the scalable manufacturing of functional materials,[4] as well as in the laboratory realization of computationally-predicted materials.[5,6] DFT-calculated thermodynamic stability or metastability can often approximate materials synthesizability,[7,8,9] but finding an optimal synthesis recipe—including temperatures, times and precursors—still requires extensive trial-and-error experimentation. The recent emergence of robotic laboratories[10-12] presents an exciting opportunity for high-throughput experiments and sequential-learning algorithms to autonomously optimize materials synthesis recipes.[13-21] However, there remains a poor fundamental understanding of how changing a synthesis recipe affects the underlying thermodynamics and kinetics of a solid-state reaction. Without this scientific foundation, it is difficult to build physics-informed synthesis planning algorithms to guide robotic laboratories,[22] meaning that parameter optimization via high-throughput experiments can end up being unnecessarily resource-intensive and wasteful.

Multicomponent oxides represent an important and challenging space for targeted synthesis. These high-component materials are key to various device technologies—including battery cathodes ($Li(Co,Mn,Ni)O_2$), oxygen evolution catalysts ($Bi_2Sr_2Ca_{n-1}Cu_nO_{2n+4+x}$), high-temperature superconductors ($HgBa_2Ca_2Cu_3O_8$), solid-oxide fuel cells ($La_3SrCr_2Mn_2O_{12}$), and

more.[23] Multicomponent oxides are usually synthesized by combining and firing the constituent binary oxide precursors in a furnace. However, this often yields impurity byproduct phases, which arise from incomplete solid-state reactions. From a phase diagram perspective, precursors start at the corners of a phase diagram and combine together towards a target phase in the interior of the phase diagram. If the phase diagram is complicated, *i.e.* with many competing phases between the precursors and the target, undesired phases may form, consuming thermodynamic driving force and kinetically trapping the reaction in an incomplete non-equilibrium state.

High-component oxides reside in high-dimensional phase diagrams and can be synthesized from many possible precursor combinations. Here we present a thermodynamic strategy to navigate these multidimensional phase diagrams—identifying precursor compositions that circumvent kinetically-competitive byproducts while maximizing the thermodynamic driving force for fast reaction kinetics. We test our principles of precursor selection using a robotic inorganic materials synthesis laboratory, which automates many tedious aspects of the inorganic materials synthesis workflow—such as powder precursor preparation, ball milling, oven firing, and X-ray characterization of reaction products. With our robotic platform, a single human experimentalist can conduct powder inorganic materials synthesis in both a high-throughput and reproducible manner. Using a diverse target set of 35 quaternary Li-, Na- and K- based oxides, phosphates and borates, which are relevant chemistries for intercalation battery cathodes[24,25] and solid-state electrolytes,[26] we show that precursors identified by our thermodynamic strategy frequently outperform traditional precursors in synthesizing high-purity multicomponent oxides. Our work demonstrates the utility of robotic laboratories not only for advanced materials synthesis and manufacturing, but also as a platform for large-scale hypothesis validation over a broad and diverse chemical space.

4.2 Principles of precursor selection

Recently, we showed that solid-state reactions between three or more precursors initiate at the interfaces between only two precursors at a time.[27] The first pair of precursors to react will usually form an intermediate byproduct, which can consume much of the total reaction energy and leave insufficient driving force to complete a reaction.[28] **Figure 4.1** illustrates this multi-step reaction progression for an example target compound $LiBaBO_3$, whose simple oxide precursors are B_2O_3, BaO, and Li_2CO_3. Because Li_2CO_3 decomposes to Li_2O upon heating, we can examine the competing chemical reactions[29] geometrically upon a pseudo-ternary Li_2O-B_2O_3-BaO convex hull. Although the overall reaction energy for $Li_2O + BaO + B_2O_3 \rightarrow LiBaBO_3$ is large at ΔE = -336 meV/atom, there are many low-energy ternary phases along the binary slices Li_2O-B_2O_3 (**Figure 4.1b**, blue) and BaO-B_2O_3 (**Figure 4.1b**, green). In the initial pairwise reactions between $Li_2O + BaO + B_2O_3$, we anticipate that stable ternary Li-B-O and Ba-B-O oxides–such as Li_3BO_3, $Ba_3(BO_3)_2$ or others—will form rapidly due to large thermodynamic driving forces of $\Delta E \sim -300$ meV/atom. Should these low-energy intermediates form, the ensuing reaction energies to the target become miniscule, *e.g.* $Li_3BO_3 + Ba_3(BO_3)_2 \rightarrow LiBaBO_3$ has only $\Delta E = -22$ meV/atom, (**Figure 4.1e,** orange).

Instead of allowing the reactions to proceed between the three precursors all at once, we suggest to first synthesize $LiBO_2$, which can serve as a high-energy starting precursor for the reaction. **Figure 4.1g** (purple) shows that $LiBaBO_3$ can be formed directly in the pairwise reaction $LiBO_2 + BaO \rightarrow LiBaBO_3$ with a substantial reaction energy of ΔE = -192 meV/atom. Moreover, along this reaction isopleth there is a low likelihood of forming impurity phases, as the competing kink of $Li_6B_4O_9 + Ba_2Li(BO_2)_5$ has relatively small formation energy (ΔE = -55 meV/atom) compared to $LiBaBO_3$. Finally, the inverse hull energy of $LiBaBO_3$, which we define as the energy

below the neighboring stable phases on the convex hull[30], is substantial at ΔE_{inv} = -153 meV/atom, suggesting that the selectivity of the target $LiBaBO_3$ phase should be much greater than any potential impurity byproducts along the $LiBO_2$-BaO slice.

Figure 4.1i compares the energy progression between these two precursor pathways. Although both pathways share the same total reaction energy, synthesizing $LiBaBO_3$ from three precursors is likely to first produce low-energy ternary oxide intermediates (**Figure 4.1a**), leaving little reaction energy to drive the reaction kinetics to the target phase.[28] By first synthesizing a high-energy intermediate ($LiBO_2$), we retain a large fraction of overall reaction energy for the last step of the reaction, promoting the rapid and efficient synthesis of the target phase. We confirm this hypothesis experimentally (**Figure 4.1j**), where we find that solid-state synthesis of $LiBaBO_3$ from the traditional precursors Li_2CO_3, B_2O_3 and BaO do not result in any XRD signal of the target phase, whereas $LiBO_2$ + BaO produces $LiBaBO_3$ with high phase purity.

From this instructive $LiBaBO_3$ example, we propose five principles to select effective precursors from a multicomponent convex hull: **1**) Reactions should initiate between only 2 precursors if possible, minimizing the chances of simultaneous pairwise reactions between 3 or more precursors. **2**) Precursors should be relatively high-energy (unstable), maximizing the thermodynamic driving force and thereby the reaction kinetics to the target phase. **3**) The target material should be the deepest point in the reaction convex hull, such that the thermodynamic driving force for nucleating the target phase is greater than all its competing phases. **4**) The composition slice formed between the two precursors should intersect as few other competing phases as possible, minimizing the opportunity to form undesired reaction byproducts, and **5**) If byproduct phases are unavoidable, the target phase should have a relatively large inverse hull

energy—in other words, the target phase should be substantially lower in energy than its neighboring stable phases in composition space.

When there were multiple precursor pairs that could be used to synthesize the target compound, we ranked the 'best' precursor pair by first prioritizing **Principle 3**, where the target compound was at the deepest point of the convex hull. This ensures that the thermodynamic driving force for nucleation of the target compound is greater than the driving forces to all other competing phases. We next prioritized **Principle 5,** where the target compound has the largest inverse hull energy. A reaction having a large inverse hull energy supersedes both **Principle 2**, as a large reaction driving force is not a sufficient criterion for synthesis; for example, in **Figure 4.2b**, where the magnitude of the driving force of $Li_2O + Zn_2P_2O_7 \rightarrow LiZnPO_4$ is large but selectivity may be weak compared to $ZnO + Li_3PO_4$. A large inverse hull energy also supersedes **Principle 4**, as a large inverse hull energy means that even if intermediate phases form, there would still be a large driving force for a secondary reaction to form the target compound.

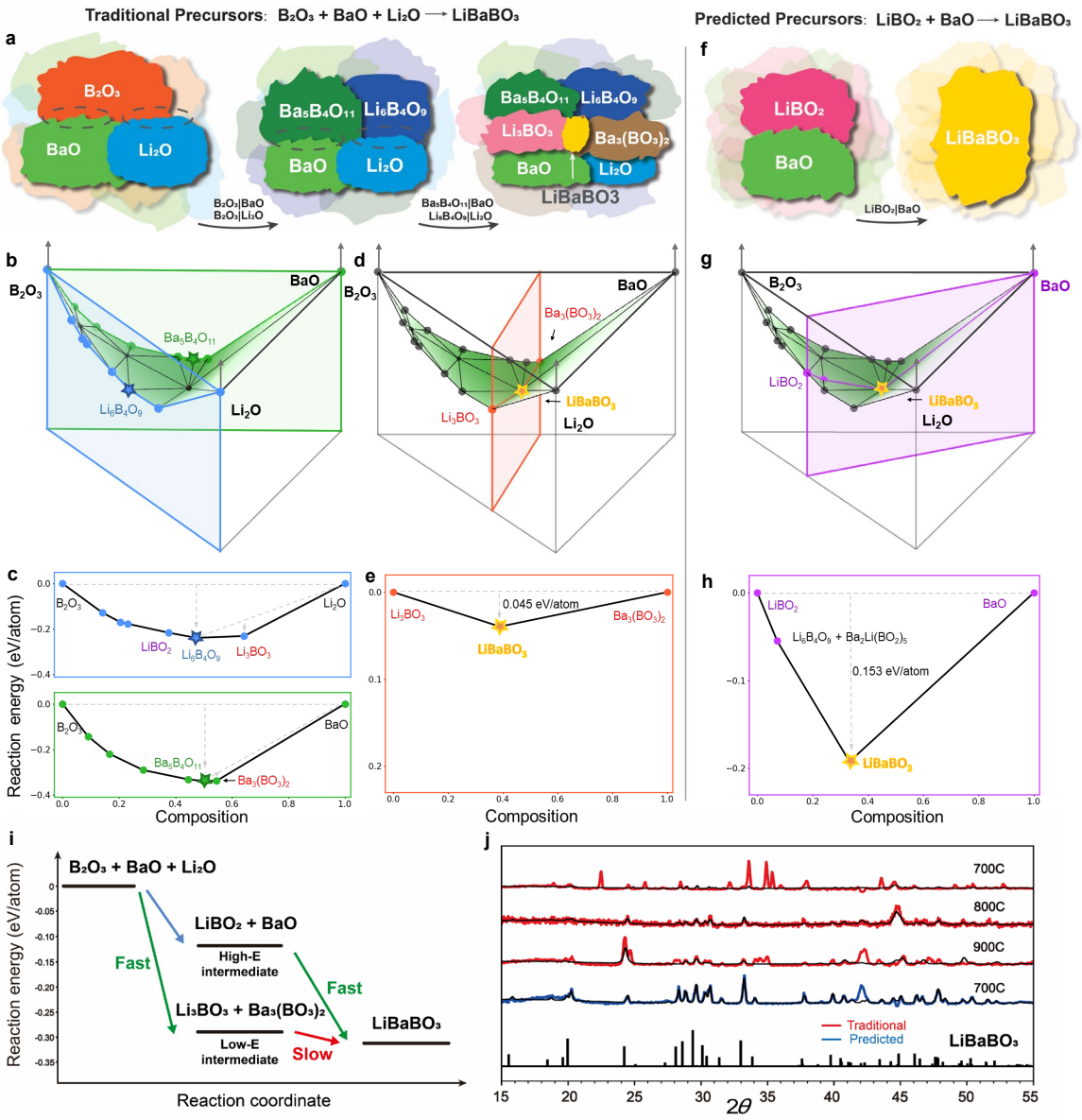

Figure 4.1: Comparison between the traditional reaction (Li_2O, B_2O_3, and BaO) process and our designed reaction ($LiBO_2$ and BaO) process for $LiBaBO_3$. a–e) are for the traditional reaction. f–h) are for the predicted reaction. a,f) Schematic of pairwise reactions process, showing the phase evolution from precursors to the target. b,d,g) are pseudo-ternary Li_2O-B_2O_3-BaO convex hulls, where reaction convex hulls between precursor pairs are illustrated by colored slices. c,e,h) 2-dimensional slices of the binary reaction convex hulls. Grey arrows show the reaction energy of the corresponding reaction. i) Free energy change in a reaction progress, where a relatively high-energy intermediate state saves more energy for the final step in forming the target. j) XRD of the solid-state synthesis of $LiBaBO_3$, where red and blue curves are raw XRD data for traditional and predicted precursors, respectively, and the black curve is the fit produced by the Rietveld refinement.

On **Figure 4.2**, we interpret these precursor design principles for an example $LiZnPO_4$ target in the pseudo-ternary Li_2O-P_2O_5-ZnO phase diagram. If we first synthesize $Zn_2P_2O_7$ to combine with Li_2O (**Figure 4.2a,b** blue), the deepest point in the reaction convex hull is not

$LiZnPO_4$ but rather is ZnO + Li_3PO_4, suggesting a kinetic propensity to form these undesired byproducts. If we start from $Zn_3(PO_4)_2$ + Li_3PO_4 (**Figure 4.2c,d**, orange), $LiZnPO_4$ is located at the deepest point along the convex hull; however Li_3PO_4 is a low-energy starting precursor, meaning there is a small driving force (ΔE = -40 meV/atom) left to form $LiZnPO_4$, likely leading to slow reaction kinetics. We suggest that $LiPO_3$ + ZnO (**Figure 4.2e,f**, purple) are the ideal precursors for $LiZnPO_4$. $LiPO_3$ has a relatively high energy along the Li_2O-P_2O_5 binary hull, resulting in a large driving force to the target phase of ΔE = -106 meV/atom. Additionally, there are no competing phases along the $LiPO_3$ + ZnO slice, minimizing the possibility of impurity byproduct phases.

In **Chapter 4.2.2,** we further interpret our precursor selection principles from the dual perspective of chemical potential diagrams, and interpret the inverse hull energy with respect to the 'chemical potential distance' as proposed by Todd *et al.*[31] Here, we chose a convex hull approach since it graphically constrains stoichiometrically-balanced pairwise reactions better than chemical potential diagrams. Additionally, in **Chapter 4.2.3** we show that our predicted precursors generally differ from those predicted by the algorithms of McDermott *et al.*,[29] and Muratahan *et al.*[32] Although all our works share the same goal of predicting inorganic synthesis recipes, the 5 principles that guide our precursor selection algorithm are based on our recent insights into the importance of pairwise reactions,[27,28] which was not considered in the PIRO algorithm by Muratahan *et al*. PIRO therefore predicts the optimal precursors for $BaLiBO_3$ to be 0.5 Ba + 0.5 $Ba(BO_2)_2$ + Li + 0.5 O_2 → $BaLiBO_3$—which likely proceeds through intermediates in this multi-precursor reaction. Our approach of maximizing driving force also differs slightly than the cost function of McDermott *et al*, whose ideal predicted reaction is $Ba_3(BO_3)_2$ + Li_3BO_3 → $BaLiBO_3$, which as we discussed earlier, has a small driving force. As deeper fundamental understanding of

solid-state reactions is achieved, we anticipate that new principles will be need to be developed and included into our algorithms for the overarching ambition of predictive solid-state synthesis.

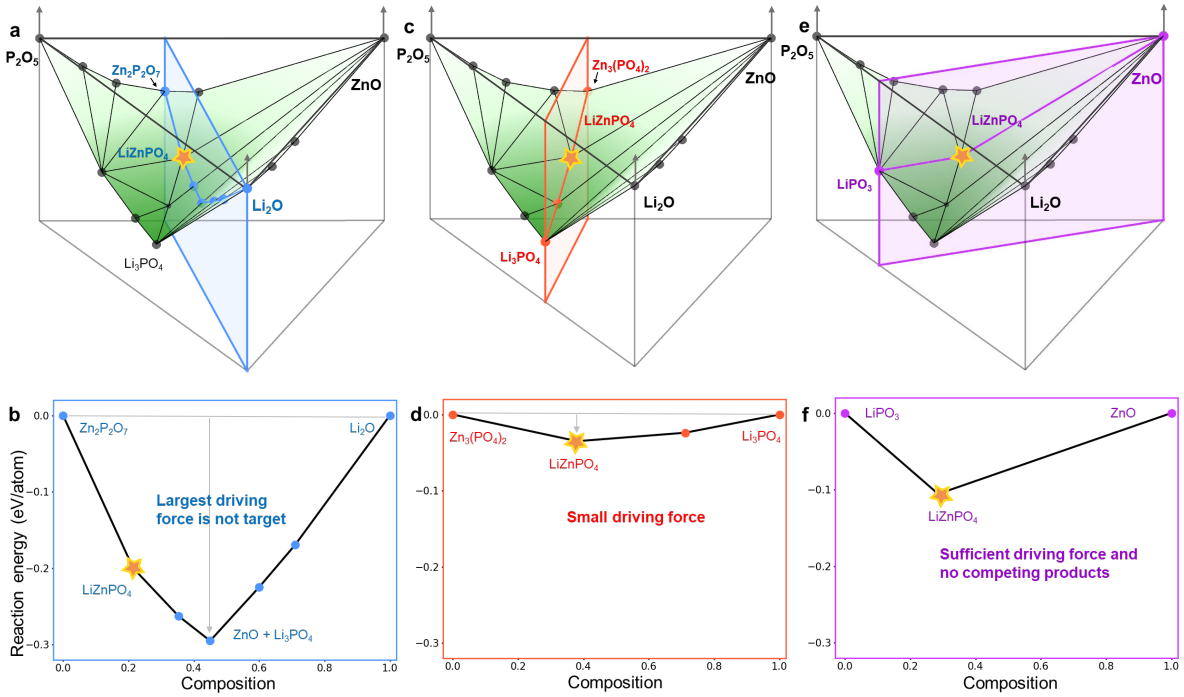

Figure 4.2: Comparison of three pairwise reactions for the synthesis of $LiZnPO_4$ on the pseudo-ternary Li_2O-P_2O_5-ZnO convex hull. **a**,**c**,**e** The blue, red, and purple slice planes correspond to $Zn_2P_2O_7 + Li_2O$, $Zn_3(PO_4)_2 + Li_3PO_4$, and $LiPO_3 + ZnO$ binary reaction convex hulls, respectively. **b**,**d**,**e** are the corresponding 2-dimensional slices.

When there were multiple precursor pairs that could be used to synthesize the target compound, we ranked the 'best' precursor pair by first prioritizing **Principle 3**, where the target compound was at the deepest point of the convex hull. This ensures that the thermodynamic driving force for nucleation of the target compound is greater than the driving forces to all other competing phases. We next prioritized **Principle 5,** where the target compound has the largest inverse hull energy. A reaction having a large inverse hull energy supersedes both Principle 2, as a large reaction driving force is not a sufficient criterion for synthesis; for example, in **Figure 4.2b**, where the magnitude of the driving force of $Li_2O + Zn_2P_2O_7 \rightarrow LiZnPO_4$ is large but selectivity may be weak compared to $ZnO + Li_3PO_4$. A large inverse hull energy also supersedes **Principle 4**, as a

large inverse hull energy means that even if intermediate phases form, there would still be a large driving force for a secondary reaction to form the target compound.

In **Chapter 4.2.2,** we further interpret our precursor selection principles from the dual perspective of chemical potential diagrams, and interpret the inverse hull energy with respect to the 'chemical potential distance' as proposed by Todd *et al.*[33] The main advantage for a convex hull approach is that it geometrically constrains stoichiometrically-balanced pairwise reactions better than chemical potential diagrams. Additionally, in **Chapter 4.2.3** we show that our predicted precursors generally differ from those predicted by the algorithms of McDermott *et al.*,[29] and Muratahan *et al*.[34] Although all our works share the same goal of predicting inorganic synthesis recipes, the 5 principles that guide our precursor selection algorithm are based on our recent insights into the importance of pairwise reactions,[27,28] which was not considered in the PIRO algorithm by Muratahan *et al*. PIRO therefore predicts the optimal precursors for $BaLiBO_3$ to be 0.5 Ba + 0.5 $Ba(BO_2)_2$ + Li + 0.5 O_2 → $BaLiBO_3$—which likely proceeds through intermediates in this multi-precursor reaction. Our approach of maximizing driving force also differs slightly than the cost function of McDermott *et al*, whose ideal predicted reaction is $Ba_3(BO_3)_2$ + Li_3BO_3 → $BaLiBO_3$, which as we discussed earlier, has a small driving force. As deeper fundamental understanding of solid-state reactions is achieved, we anticipate that new principles will be need to be developed and included into our algorithms for the overarching ambition of predictive solid-state synthesis.

4.2.1 Computation of precursor selection algorithm

The code used to predict precursors for more efficient synthesis is open-sourced at https://github.com/dd-debug/synthesis_planning_algorithm. The code is built in python, and leverages the Materials Project Application Programming Interface (API) and the pymatgen code base, specifically, pymatgen.analysis.phase_diagram and pymatgen.analysis.interface_reactions modules. Compositions and energies of various materials systems were retrieved from the Materials Project using the REST API in December 2020.

To determine the precursors predicted using our design principles, we first collect all quaternary oxides with Li-, Na-, and K- cations, including quaternary oxides that have complex phosphate $(PO_4)^{3-}$ and borate $(BO_3)^{3-}$ anions. For a given *A*-*B*-*C*-O quaternary oxide convex hull, for each quaternary oxide, we enumerate all pairwise precursor combinations that can form these candidate target phases. In this study, we only considered candidate targets that fall on an isopleth between a pair of precursors. It is not generally the case that two precursors will be available for each target oxide. We exclude reactions that consider elemental O_2 as a precursor. In the convex hull, each pairwise reaction corresponds to the slice plane between the pairwise precursors, which intersects the target. This approach determines all compositionally feasible pairwise reactions for the formation of all candidate quaternary oxide targets.

The list is the further sieved by identifying reactions where the target material is the deepest point in the reaction convex hull (as calculated from the interface_reactions module). We also evaluate the *inverse hull energy* of each phase, defined as the energetic extent by which the target phase is below its neighboring stable phases in the convex hull. The Inverse Hull Energy is illustrated in **Figure 4.3** for the target $Li_3Sc_2(PO4)_3$ phase from the precursors $LiPO_3$ + Sc_2O_3. Of the two possible reactions that could form $Li_3Sc_2(PO4)_3$, which are $3LiPO_3 + Sc_2O_3 \rightarrow Li_3Sc(PO_4)_3$

and $2ScPO_4 + Li_3PO_4 \rightarrow Li_3Sc_2(PO_4)_3$, we hypothesize that $3LiPO_3 + Sc_2O_3$ will be the best precursors, due to its large inverse hull energy.

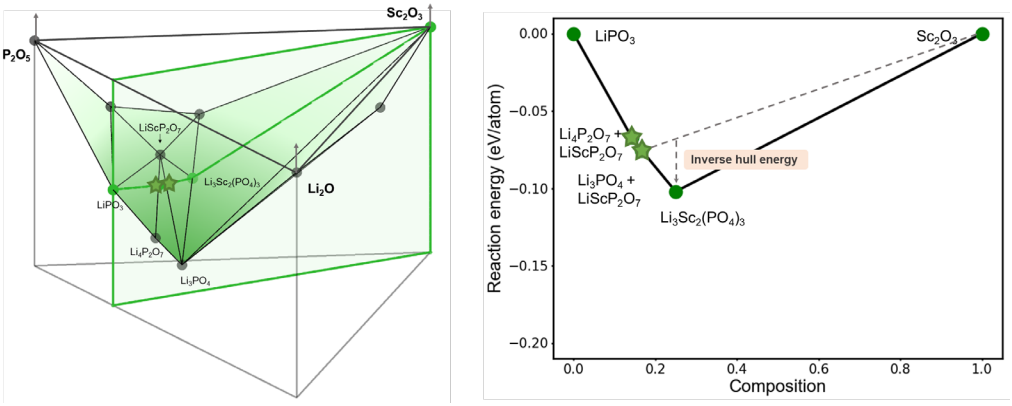

Figure 4.3: Reaction compound convex hull of $Li_3Sc_2(PO_4)_3$. **Left.)** the convex hull of P_2O_5, Sc_2O_3, and Li_2O, where two kinks (green stars) represent the decomposition reactions that might happen at given compositions. The equilibrium phase is a 2-phase coexistence. The green slice plane corresponds to **Right.)** $LiPO_3|Sc_2O_3$ convex hull.

The inverse hull energy is computed using the reaction convex hull from interface_reactions, where we identify the kinks in the convex hull that compete with the target compound. Because this is a 1-dimensional compositional intersection with a 3-dimensional quaternary phase diagram, the intersection can include critical compositions that correspond to single phases, or tie lines between 2 phases. If the intersected tie line is the deepest point in the reaction convex hull, we anticipate the reaction will form the terminal phases of the tie line, such as green stars will decompose to $Li_4P_2O_7 + LiScP_2O_7$ and $Li_3PO_4 + LiScP_2O_7$ in **Figure 4.3**.

In executing this algorithm over the Li-, Na- and K- containing quaternary oxides, borates and phosphates, we identified 3104 reactions. We then determined the minimum set of precursors that would maximize the number of potential candidate reactions, whilst also considering the available precursors available on hand at Samsung. This process led to the target materials and precursor selections presented in this work. When there were multiple precursor pairs that could be used to synthesize the target compound, we chose the final precursor pair by first prioritizing Principle 3, where the target compound was at the deepest point of the convex hull—this ensures

that the thermodynamic driving force for nucleation of the target compound is greater than the driving forces to all other competing phases. We next prioritized Principle 5, where the target compound has the largest inverse hull energy. A reaction having a large inverse hull energy supersedes both Principle 2, the reaction energy (as illustrated by the discussion around Figure 2a) and Principle 4, number of competing phases – as the number of competing phases may not matter so much if the driving force to the target was much more significant than to the competing phases.

When there were multiple precursor pairs that could be used to synthesize the target compound, we chose the final precursor pair by first prioritizing Principle **3**, where the target compound was at the deepest point of the convex hull. This ensures that the thermodynamic driving force for nucleation of the target compound is greater than the driving forces to all other competing phases. We next prioritized Principle **5**, where the target compound has the largest inverse hull energy. A reaction having a large inverse hull energy supersedes both Principle **2,** the reaction energy and Principle **4,** number of competing phases. A large reaction driving force is not a sufficient criterion for synthesis; for example, in **Figure 4.2b** where the magnitude of the driving force of $Li_2O + Zn_2P_2O_7 \rightarrow LiZnPO_4$ is large but selectivity may be weak compared to $ZnO + Li_3PO_4$. On the other hand, a large inverse hull energy means that the driving force from the competing phases to the target phase would be large, meaning that the *relative* driving force to the target phase is large, and even if competing phases did form, there would be a large driving force for a secondary reaction to form the target compound from any intermediate phases.

4.2.2 Precursor selection principles using chemical potential diagrams

In Todd *et al.*,[33] chemical potential diagrams are used to assess the selectivity of phases during solid-state synthesis. Here, we interpret our precursor selection principles, which are built from a convex hull representation, from the perspective of a chemical potential diagram, which was also discussed in **Chapter 2 and 3**. [35,36,37]

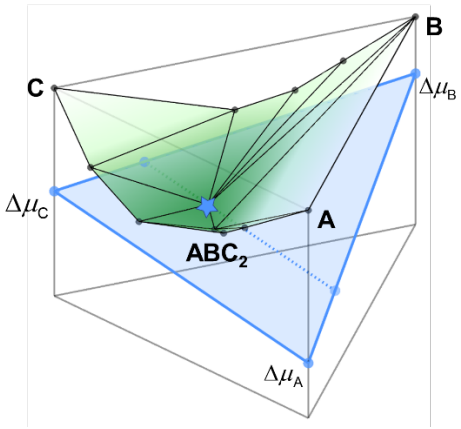

Figure 4.4: Schematic figure illustrating how to determine the elemental chemical potential domain for a target material through intercepts of the corresponding tangent plane.

The chemical potential diagram is a dual representation of the convex hull, meaning it offers an alternative perspective on the same geometric object (similar to how real space and reciprocal space are dual of each other). The chemical potential diagram can be built from the convex hull using the intercept rule, produced by tilting a tangent plane underneath a ternary convex hull, as illustrated in **Figure 4.4**. **Figure 4.5** shows for the Li-Zn-P-O system the convex hull, as well as its corresponding chemical potential diagram on μ_{Li}, μ_{Zn}, μ_P axes (with fixed $\mu_O = 0$, corresponding to oxygen gas at ambient conditions). The phases that appear on the convex hull exactly correspond to the phases on the chemical potential diagrams. The three-phase coexistence *triangles* on the convex hull correspond to the three-phase coexistence *points* on the chemical potential diagram, while the single-phase *points* on the convex hull correspond to the single-phase *polygons* in the chemical potential diagram.

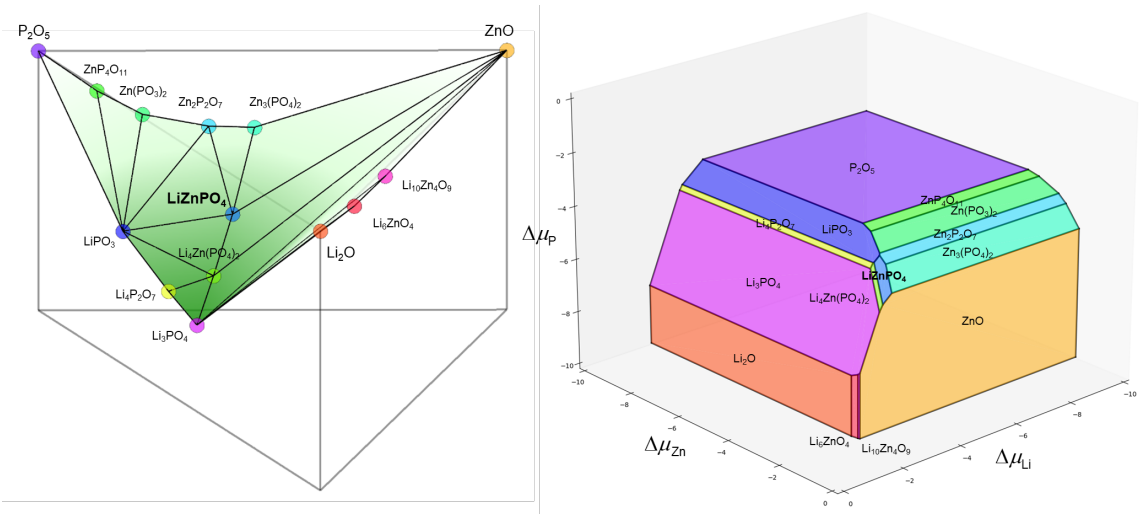

Figure 4.5: Comparison between convex hull and chemical potential diagram. Same phase is marked in the same color. Left) ZnO-P_2O_5-Li_2O compound convex hull. Right) P-Zn-Al chemical potential diagram when μ_O is fixed at -2 eV/atom.

Figure 4.6 uses a model A-B system to show that the inverse hull energy of a phase is directly proportional to the size of its stability window on a chemical potential diagram. In **Figure 4.6a** we constructed a convex hull with a relatively deep inverse hull energy for A_3B_4, and a smaller inverse hull energy in **Figure 4.6c**; with the formation energies of all other phases held the same. This larger inverse hull energy from **4.6a** corresponds to a wider chemical potential stability window for A_3B_4 in both μ_A and μ_B, as shown by the intercept rule. In Figures **4.6b,d** we show the size of the stability domain for A_3B_4 on a chemical potential diagram. For the large inverse hull energy in **4.6a**, we see a correspondingly larger chemical potential stability window for A_3B_4 in **4.6b**; and vice versa a smaller inverse hull energy in **4.6c** results in a smaller chemical potential window in **4.6d.** This size of the chemical potential window is similar to the 'chemical potential distance' metric presented in Todd *et al.*[1] In this sense, our selection of the inverse hull energy metric is comparable to the arguments from Todd et al., in that both approaches indicate a stronger tendency for the target phase to form.

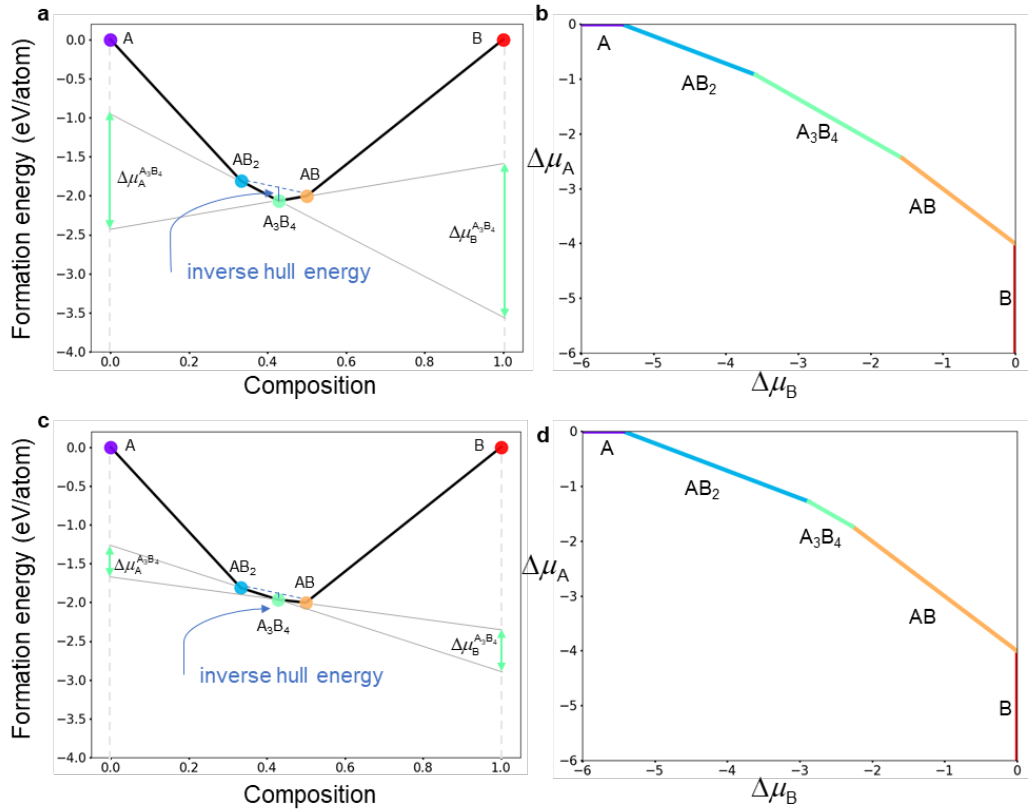

Figure 4.6: The relationship between inverse hull energy and chemical potential stability window of A_3B_4. The convex hull of A-B system with a) large, c) small inverse hull energy of A_3B_4, and the corresponding chemical potential diagram of A-B system with b) large, d) small inverse hull energy of A_3B_4. Larger inverse hull energy corresponds to larger size of chemical potential window.

One disadvantage of chemical potential diagrams is that it is not straightforward to graphically illustrate stoichiometrically-balanced pairwise reactions on a chemical potential diagram. Take for example the $Li_2O + Zn_2P_2O_7 \rightarrow LiZnPO_4$ reaction from **Figures 4.2a** and **4.2b**. It is very clear on the convex hull that there are 5 stoichiometrically-balanced reaction products on the Li_2O | $Zn_2P_2O_7$ isopleth, including the phase-separated products $ZnO + Li_3PO_4$—which is in fact the product pair with the largest reaction energy. This fact is not very obvious on the chemical potential diagram from **Figure 4.5** above—where even though ZnO and Li_3PO_4 have very large stability regions by themselves, on the chemical potential diagram their 2-phase coexistence is represented only by a phase boundary line, which looks like any other phase-boundary line on the chemical potential diagram.

For this reason, we elected to conduct our analyses from the convex hull perspective. By using the inverse hull energy metric, we capture the size of a stability region from a chemical potential diagram, however we also have the advantage of directly visualizing stoichiometrically-balanced reactions, as well as the driving force to form multi-phase mixtures.

4.2.3 Comparison against other synthesis prediction algorithms

Recently, Muratahan *et al*. [32] devised a synthesis route prediction algorithm named PIRO, which is grounded in the principles of nucleation barrier assessment for the target phase on reactant surfaces, as well as the enumeration of competing phase occurrences. A lower nucleation barrier coupled with a reduced number of competing phases signifies an increased likelihood of the formation of the target phase. PIRO addresses a Pareto optimization problem to minimize the nucleation barrier and mitigate the competition from parasitic phases. In the case of $BaLiBO_3$, PIRO suggests the best following reaction: $0.5\ Ba + 0.5\ Ba(BO_2)_2 + Li + 0.5\ O_2 \rightarrow BaLiBO_3$. Our predicted precursors, $BaO + LiBO_2 \rightarrow BaLiBO_3$, is ranked as the 72nd best option in PIRO, and is accompanied by a nucleation barrier of 2.37 atomic units (64.49 eV) which is relatively large compared to other precursors. The main qualitative difference between PIRO and our algorithm is we impose a constraint on pairwise reactions, since reactions from multiple elementary precursors can often get kinetically trapped in low-energy intermediate reaction products.

McDermott *et al.*[29] developed a graph-based network for the prediction of chemical reactions, where the graph data structure was constructed using a combination of phases within the convex hull as nodes, and reaction-energy-based descriptors as the weights of edges. Subsequently, pathfinding algorithms were employed to identify the lowest 'cost' from precursor nodes to target nodes, thereby predicting reaction pathways. For $BaLiBO_3$, the optimal reaction recommended by McDermott *et al.*, is $Ba_3(BO_3)_2$ + Li_3BO_3 → $BaLiBO_3$, (green slice in **Figure 4.7**). The reaction energy and inverse hull energy values for this reaction is $\Delta G_{rxn} = \Delta G_{inv}$ = -0.04 eV/atom. On the other hand, our predicted reaction BaO + $LiBO_2$ → $BaLiBO_3$ has reaction energy and inverse hull energy values of ΔG_{rxn} = -0.192 eV/atom, ΔG_{inv} = -0.153 eV/atom.

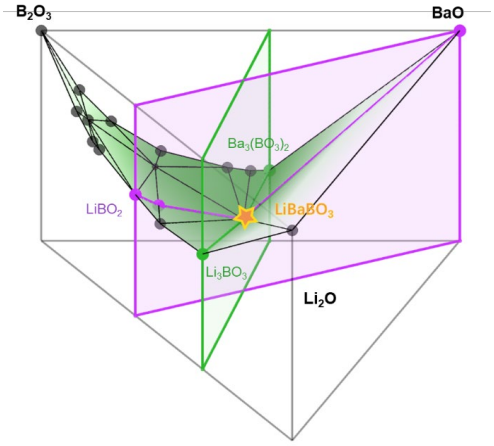

Figure 4.7: Ternary compound convex hull of Li_2O, B_2O_3, and BaO. The green and purple slices show two different reactions to the target phase $LiBaBO_3$

4.3 Validation with a robotic ceramic synthesis laboratory

To test our precursor selection hypotheses, we designed a large-scale experimental validation effort based in the quaternary Li-, Na-, and K-based oxides, phosphates and borates, which are representative chemistries for intercalation battery materials.[24,26] We survey the Materials Project[38] for all known quaternary compounds in this space, then we use our selection principles to predict optimal precursors from the DFT-calculated convex hulls. We also determine the traditional precursors for these reactions, which we previously text-mined from the solid-state synthesis literature.[39] To efficiently maximize the coverage of our experimental validation, we Pareto-optimized our reaction list to select the fewest number of precursors that maximize the

number of candidate reactions—resulting in 28 unique precursors for 35 target materials that span 27 elements.

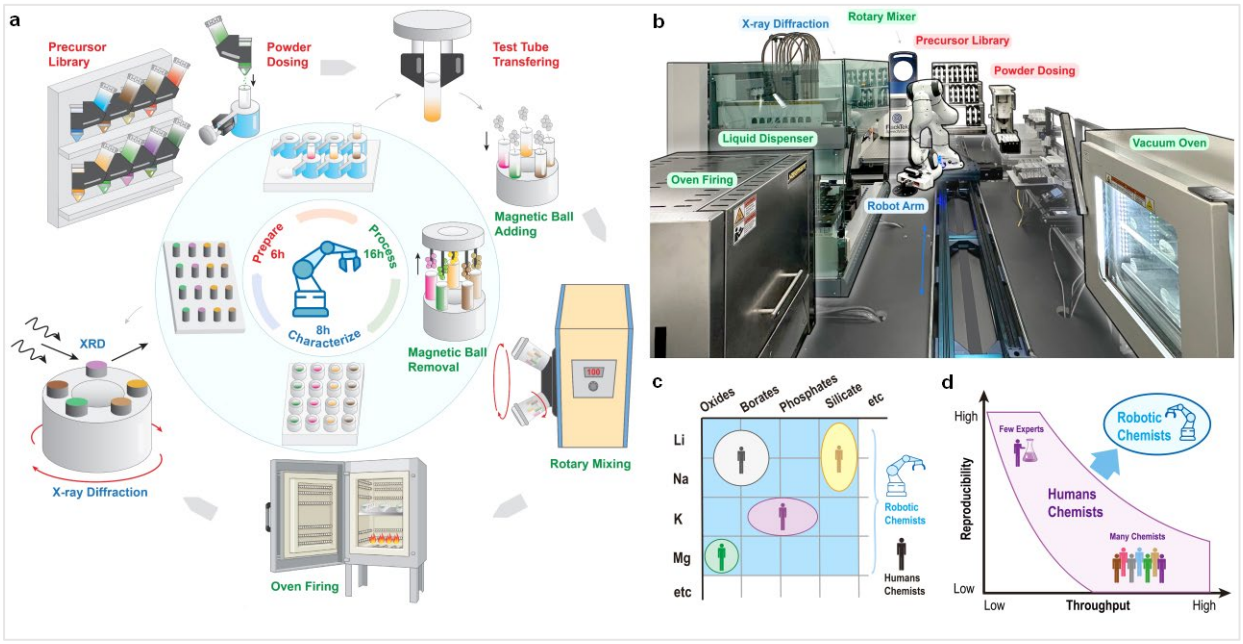

Figure 4.8: Automated Synthesis Testing and Research Augmentation (ASTRAL) Lab at Samsung's Advanced Materials Lab in Cambridge, Massachusetts. a) A robot-enabled inorganic materials synthesis workflow—from powder precursor preparation to ball milling, to oven firing, to X-ray characterization of reaction products; b) picture of the ASTRAL Lab c) Robotic chemists enable a paradigm of large-scale exploration of synthesis hypotheses over a broad chemical space, which normally would have to be undertaken by multiple experimentalist groups. d) Human experimentalists have a trade-off between throughput and reproducibility, whereas robotic chemists can achieve both high reproducibility and throughput simultaneously.

We then compare the phase purity of target materials synthesized from our predicted precursors versus from traditional precursors. We perform this large-scale validation effort using a robotic inorganic materials synthesis laboratory named ASTRAL (Automated Synthesis Testing and Research Augmentation Lab), located at the Samsung Advanced Institute of Technology in Cambridge, Massachusetts. As shown in **Figure 4.8**, ASTRAL uses a robotic arm to automate sample handling throughout a full ceramic synthesis workflow—from powder precursor preparation to ball milling, to oven firing, to X-ray characterization of reaction products. Three trays of 24 samples can pass sequentially through the ASTRAL workflow every 72 hours. The throughput of ASTRAL is bottlenecked by powder dispensing and processing, as each 24-sample

tray is prepared serially, whereas the firing and characterization steps can, in principle, be run in parallel.

ASTRAL automates inorganic materials synthesis from powder precursors, as opposed to previous robotic laboratories that rely on solution-based precursors,[15,16,17,40] inkjet printing[18] or combinatorial thin-film deposition.[14,19] Although it is easier to dose precursor concentrations using these other methods, the resulting products are typically only produced at milligram scale. Powder synthesis, on the other hand, can yield grams of material, which is needed to create ceramic pellets or electrodes for functional property characterization. Moreover, high-temperature powder synthesis is the primary synthesis method of ceramic oxides, so recipes determined from ASTRAL can be upscaled for industrial manufacturing. We overcame major practical challenges in powder precursor processing, which arise primarily from flowability differences between different powders due to varying particle sizes, hardness, hygroscopicity, and compaction. In **Table 4.1** we summarize the challenges in working with powder precursors, as well as our solutions to these challenges.

In total, we conducted 224 synthesis reactions over 35 target materials, calcined at temperatures from 600°-1000°C. For a target space this diverse, traditional validation of our precursor selection principles would likely have required an extensive experimental effort, comprised of multiple human experimentalists working over many years. Once the robotic laboratory is set up, we can comprehensively survey this broad crystal chemistry space in a single experimental campaign (**Figure 4.8c**). Moreover, a large-scale human effort will inevitably require trade-offs between throughput and reproducibility. Meanwhile, a robotic laboratory produces single-source experimental data with high reproducibility, meaning we can systematically compare synthesis results while minimizing human variability and error (**Figure 4.8d**). Altogether,

the robotic laboratory offers a new platform for data-driven empirical synthesis science, where hypotheses can be investigated rapidly, reproducibly, and comprehensively over diverse crystal chemistries.

Table 4.1: Problems of powder ceramic synthesis for automated laboratory and our solutions.

Challenges	Solutions
Powders are difficult to handle for automated dispensing due to varying size and physical properties	The ASTRAL platform using a Quantos powder dispenser supplied by Mettler Toledo, which uses gravimetric dispensing to dose precursor powders with high accuracy. To accommodate broad variety of powder types needed for synthesis experiments, each precursor powder is assigned one of three models of dosing heads for reliable dispensing.
Hygroscopic precursors	For handling hygroscopic precursors, we use the Quantos dosing heads for short-term storage, tightly sealed to minimize moisture infiltration. Hygroscopic powders are replaced on a schedule to maintain the quality of the dispensed precursors.
Powders are much more difficult to mix than liquid precursors	Successful synthesis requires that precursors are mixing intimately and homogeneously before heat treatment to produce a uniform and consistent product. The ASTRAL platform accomplishes mixing of powders using a high-throughput ball milling system, consisting of the following components: • High-throughput dispensing of mixing balls • Automated addition of milling solvent • High-throughput milling holders • Magnetic mixing ball extraction • High-throughput powder transfer to crucibles using funnel plate
Powders react and/or fuse with crucibles during high temperature heat treatment	During high-temperature calcination, many precursors or reaction products may become molten, and react with the alumina crucible, resulting in contamination with aluminum and/or fusing of the sample to the crucible walls. We apply a boron nitride coating to the alumina crucibles for materials that are susceptible to this behavior. The boron nitride coating is highly non-reactive and resists wetting by most molten oxides, minimizing reactivity and fusing between the samples and crucibles.
Difficulties in preparing and mounting powders for XRD characterization	It is challenging to automate preparation of powders for characterization, due to varying physical properties and lack of a solvent to assist with dispersal. To address this, the ASTRAL platform performs characterization using a high-throughput system for XRD measurement, consisting of: • Custom magnetic sample stubs for XRD measurements • High-throughput mounting of powders onto XRD stubs by full plate • Fully automated robotic XRD loading and measurement execution

4.3.1 Robotic laboratory setup and procedures

ASTRAL employs a comprehensive robotic system, consisting of a 7-axis Panda robotic arm (Franka Emika) and a linear rail (Vention.io), to facilitate the transportation of samples between various stations. The integration of the Panda arm with the linear rail extends the system's

manipulation capabilities, enabling precise laboratory operations over a sizable 1.7m × 4m area. The central rail system is surrounded by specialized stations dedicated to inorganic materials synthesis tasks.

These stations include mechanisms for dispensing solid powder precursor chemicals and liquid dispersants, a mechanical ball mill for effective mixing, a furnace for the calcination and reaction of precursors, and X-ray diffraction for characterizing synthesis outcomes. The synergy between these stations enables a seamless workflow in the synthesis.

The dispensing of precursor powders is carried out sequentially using a Quantos powder dispenser (Mettler Toledo). Sample vials and powder dosing heads are efficiently exchanged using the robotic arm. Subsequently, a Freedom EVO 150 liquid handling robot (Tecan Life Sciences) dispenses 1mL of ethanol into each vial. The samples then undergo rotary ball milling for 15 hours at 100rpm to achieve a homogeneous and fine mixture of precursor powders. Alumina crucibles (Advalue Technology) are employed to contain the mixed precursors.

Following the ball-milling process, samples are heated to 80°C for 2 hours under vacuum to eliminate residual ethanol. Subsequently, they are transferred to a furnace and subjected to calcination in an air atmosphere for 8 hours at temperatures ranging from 600°C to 1000°C. The resulting powders are meticulously characterized using powder X-ray diffraction (Rigaku Miniflex 600).

For further details regarding the robotic infrastructure, additional insights can be found in the Supplementary Information of Jiadong Chen's paper.[41] However, as the robotic lab is not the primary focus of this thesis, we will not delve into further detail here.

4.3.2 Automated XRD analysis

X-ray diffraction is the primary characterization method used by the ASTRAL platform to determine the outcome of synthesis experiments. Standard methods used for XRD analysis require two steps: (1) identification of phases present in the sample, and (2) pattern fitting through methods such as Rietveld refinement to quantify the lattice parameters and weight percent of the phases. The traditional method for phase identification is to compare collected XRD patterns to a database of reference structures such as the Inorganic Crystal Structure Database (ICSD), most often using a search-match algorithm to compare peak positions and determine likely matches. While this approach is very effective at detecting matches to known structures, it requires a human to review candidate structures to exclude false positives and select true matches. More recently, several research groups have presented machine learning algorithms that can be trained on a set of reference structures to identify phases in experimental XRD [Manuscript References 36, 37]. These machine learning approaches offers great potential for improving automated phase identification, but requires additional steps to construct an appropriate training data set consistent with the characteristics of the experimental setup and chemical spaces. The training of these machine-learning methods is also reported in Ref 36 to take up to 20 hours for a system, also requiring GPU-accelerated machines.

Given the 35 systems that we are investigating here, we were not able to use these machine-learning methods to fully quantify all impurity phases detected in XRD for all samples processed on the ASTRAL platform. However, some quantification of synthesis outcomes is necessary to efficiently analyze trends over large data sets. Therefore, we have adopted a semi-quantitative approach to evaluating synthesis outcomes, based on Rietveld refinement of the XRD using only the crystal structure of the target material.

Rietveld refinement of data is accomplished using the BGMN kernel, with python scripts used for the automated generation of the necessary input files, execution of the Rietveld refinement via the command line, and extraction of the fitting data from the output files. The target structure is used as the sole input phase for the BMGN kernel, and as such, in an ideal case, the Rietveld refinement will split the XRD signal into components associated with the target phase, background, and residual. The fraction of the target phase can then be estimated by dividing the integrated intensity of the target phase by the combined intensity of the target phase and residual, $I_{target}/(I_{target} + I_{residual})$. In this work we considered values greater than 0.5 to be high purity, between 0.2 and 0.5 moderate purity, and less than 0.2 considered low purity.

For samples of low purity, where the peaks corresponding to the target phase are small in magnitude, the integration of co-aligned peaks for small peak heights can be difficult to ascribe precisely to the target phase (as opposed to noise). Therefore, the phase fraction characterized from our XRD result should primarily be interpreted quantitatively for purity greater than 0.2

To minimize the excess residual, for each sample the algorithm supplies a background XRD pattern taken on an empty sample holder, to increase the effectiveness of the BGMN background fitting. As the background differs slightly for different sample holders, this procedure is repeated for each of 16 XRD patterns for empty sample holders, and the lowest residual is used as the final value for the calculation.

The primary limitations of this method are: (1) it neglects the different scattering factors of the target and impurity phases, (2) it can underestimate phase fraction due to any components of the residual that are not associated with impurity phases, and (3) it can overestimate phase fraction due to incorrect fitting of peaks for the target phase to impurity peaks. Due to the possibility of false positives due to (3), a value of 0.2×10^6 counts is used as a detection threshold, so the target

phase is considered not detected for any samples where the target phase intensity is lower than this value.

Despite these potential limitations, we validated that our procedure produces adequate results on a wide range of data, and is suitably accurate for detecting successful or failed synthesis outcomes in the great majority of cases. To perform this validation, we used a set of 255 previously-obtained experimental XRD patterns collected using the ASTRAL platform for which all impurity phases were identified. We then compared our approach of calculating $I_{target}/(I_{target} + I_{residual})$, versus the fully Rietveld refined XRD phase fractions.

Figure 4.9 shows a comparison of the XRD quantification results using both our semi-quantitative method described above and full quantitative Rietveld refinement. The color of the dots correspond to the weighted R-factor R_{wp}/R_{exp} returned by the BGMN kernel as a goodness-of-fit metric, with higher values indicating greater discrepancy between the theoretical and experimental curves. The semi-quantitative method produced an estimated phase fraction that was on average 22.9% lower than the full quantitative refinement, but otherwise the two measures produced good agreement with a root mean squared difference of 4.6%. Therefore, we consider that the phase purity estimates produced by the semi-quantitative method are likely to be conservative, but generally effective for discriminating synthesis outcomes within 10% accuracy.

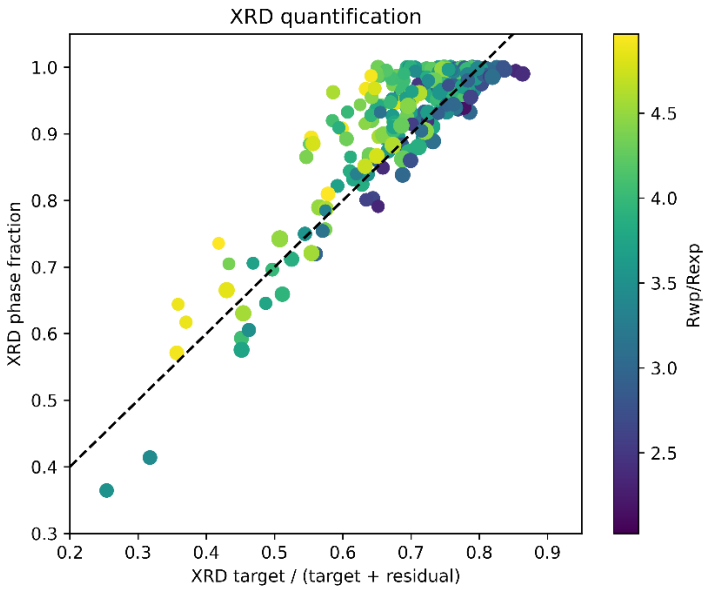

Figure 4.9: Comparison between semi-quantitative XRD analysis (x-axis) and full quantitative Rietveld refinement (y-axis) on a test data set of 255 samples synthesized on the ASTRAL platform. The size of the points is determined by the integrated XRD signal, while the color of the dots are determined by the quality-of-fit metric (R_{wp}/R_{exp}) output by BGMN for the full Rietveld refinement.

4.4 Synthesis results and comparison with traditional recipes

For the 35 materials selected, **Figure 4.10a** shows the relative yield of the target phase starting from computationally-designed versus traditional precursors. **Figure 4.10b** shows the reaction temperatures attempted, and **Figure 4.10c** shows the relative performance of the predicted versus traditional precursors. A full list of targets, precursors and reaction results are listed in **Table 4.2**. For 32 out of 35 compounds (91%), the predicted precursors successfully produce the target phase. In 15 targets, the predicted precursors achieve at least 20% higher phase purity than the traditional precursors (green), and 6 of these 15 target materials could *only* be synthesized by the predicted precursors (dark green). For 16 reactions the precursors have similar target yields (light green), and only in 4 systems do the traditional precursors perform better than the predicted precursors (red). However, we note that even in these 4 systems, the predicted precursors also produce the target materials with moderate to high purities.

Table 4.2: Traditional and predicted precursors for different targets. The colors in the first four columns represent shows how much better the predicted precursors over traditional, where green means predicted precursors perform better, light green means they perform similarly, and red means traditional precursors perform slightly better. The color in the "Best predicted Synthesis" column represents what is the best phase purity the predicted precursors can get, where green means high phase purity, light blue means moderate purity, yellow means low purity, and gray means both traditional and predicted precursors failed with no XRD signal. The "Best Temperature" column shows the reaction temperature to get the best synthesis results using predicted precursors. The last two columns show the inverse hull energies and reaction energies for predicted precursors.

	Target	Traditional Precursors	Predicted Precursors	Best Predicted Synthesis	Best Temperature (C)	For predicted precursors (eV/atom) Inverse hull energy	Reaction Energy
1	$BaLiBO_3$	Li_2CO_3, B_2O_3, BaO	BaO, $LiBO_2$		800	-0.153	-0.192
2	$K_2Zr(PO_4)_2$	K_2CO_3, $NH_4H_2PO_4$, ZrO_2	KPO_3, ZrO_2		800	-0.068	-0.068
3	$Li_3Pr_2(BO_3)_3$	Li_2CO_3, B_2O_3, Pr_6O_{11}	$LiBO_2$, Pr_6O_{11}	High purity	600	-0.015	-0.057
4	$KNiPO_4$	K_2CO_3, $NH_4H_2PO_4$, NiO	KPO_3, NiO		800	-0.050	-0.050
5	$Li_3Sc_2(PO_4)_3$	Sc_2O_3, Li_2CO_3, $NH_4H_2PO_4$	Sc_2O_3, $LiPO_3$		900	-0.034	-0.102
6	$LiGeBO_4$	Li_2CO_3, B_2O_3, GeO_2	$LiBO_2$, GeO_2		800	-0.026	-0.040
7	$KLi(PO_3)_2$	Li_2CO_3, K_2CO_3, $NH_4H_2PO_4$	$LiPO_3$, KPO_3	Moderate	800	-0.009	-0.009
8	$LiNbWO_6$	Li_2CO_3, Nb_2O_5, WO_3	$LiNbO_3$, WO_3	Low purity	700	0.000	0.000
9	$LiZnBO_3$	Li_2CO_3, ZnO, B_2O_3	$LiBO_2$, ZnO		700	0.000	0.000
10	$K_3Fe_2(PO_4)_3$	K_2CO_3, $NH_4H_2PO_4$, Fe_2O_3	KPO_3, Fe_2O_3		700	-0.042	-0.042
11	$KMgPO_4$	K_2CO_3, $NH_4H_2PO_4$, MgO	MgO, KPO_3		800	-0.123	-0.123
12	$K_3Bi_2(PO_4)_3$	K_2CO_3, $NH_4H_2PO_4$, Bi_2O_3	Bi_2O_3, KPO_3		700	-0.079	-0.079
13	$K_3LiP_2O_7$	Li_2CO_3, $NH_4H_2PO_4$, K_2CO_3	$LiPO_3$, K_3PO_4		700	-0.035	-0.071
14	$Na_2Al_2B_2O_7$	Na_2CO_3, Al_2O_3, B_2O_3	Al_2O_3, $NaBO_2$		700	-0.014	-0.024
15	$K_3Al_2(PO_4)_3$	K_2CO_3, $NH_4H_2PO_4$, Al_2O_3	KPO_3, Al_2O_3		700	-0.063	-0.067
16	$Li_2CuP_2O_7$	Li_2CO_3, $NH_4H_2PO_4$, CuO	$LiPO_3$, CuO		700	-0.036	-0.036
17	$LiNbGeO_5$	GeO_2, Li_2CO_3, Nb_2O_5	GeO_2, $LiNbO_3$	High purity	1000	-0.024	-0.024
18	$Li_3Fe_2(PO_4)_3$	Li_2CO_3, $NH_4H_2PO_4$, Fe_2O_3	$LiPO_3$, Fe_2O_3		700	-0.008	-0.048
19	$SrLiBO_3$	Li_2CO_3, B_2O_3, SrO	$LiBO_2$, SrO		600	-0.119	-0.149
20	$KNbWO_6$	K_2CO_3, Nb_2O_5, WO_3	WO_3, $KNbO_3$		800	-0.024	-0.042
21	$LiMgPO_4$	Li_2CO_3, $NH_4H_2PO_4$, MgO	$LiPO_3$, MgO		800	-0.032	-0.143
22	$LiZnPO_4$	Li_2CO_3, $NH_4H_2PO_4$, ZnO	$LiPO_3$, ZnO		800	-0.106	-0.106
23	$KBaPO_4$	K_2CO_3, $NH_4H_2PO_4$, BaO	KPO_3, BaO		700	-0.316	-0.316
24	$KTiPO_5$	K_2CO_3, $NH_4H_2PO_4$, TiO_2	TiO_2, KPO_3		800	-0.057	-0.057
25	$LiMnPO_4$	Li_2CO_3, $NH_4H_2PO_4$, MnO	$LiPO_3$, MnO		700	-0.061	-0.132
26	KTa_2PO_8	K_2CO_3, $NH_4H_2PO_4$, Ta_2O_5	KPO_3, Ta_2O_5		700	-0.015	-0.036
27	$Li_3Y_2(BO_3)_3$	Li_2CO_3, Y_2O_3, B_2O_3	$LiBO_2$, Y_2O_3	Low purity	700	-0.014	-0.038
28	$KTiNbO_5$	K_2CO_3, TiO_2, Nb_2O_5	TiO_2, $KNbO_3$		700	-0.006	-0.013
29	$BaNaBO_3$	Na_2CO_3, BaO, B_2O_3	BaO, $NaBO_2$		600	-0.172	-0.172
30	$Li_3V_2(PO_4)_3$	Li_2CO_3, $NH_4H_2PO_4$, V_2O_3	$LiPO_3$, V_2O_3	Not detected	900	-0.024	-0.062
31	$NaSiBO_4$	Na_2CO_3, SiO_2, B_2O_3	SiO_2, $NaBO_2$		600	-0.008	-0.022
32	Li_2TiGeO_5	GeO_2, Li_2CO_3, TiO_2	GeO_2, Li_2TiO_3	High purity	1000	-0.008	-0.036
33	Li_2TiSiO_5	SiO_2, TiO_2, Li_2CO_3	SiO_2, Li_2TiO_3		1000	-0.026	-0.026
34	$NaSrBO_3$	Na_2CO_3, SrO, B_2O_3	SrO, $NaBO_2$	Moderate	700	-0.118	-0.118
35	$LiSi_2BO_6$	Li_2CO_3, SiO_2, B_2O_3	$LiBO_2$, SiO_2		700	-0.004	-0.010

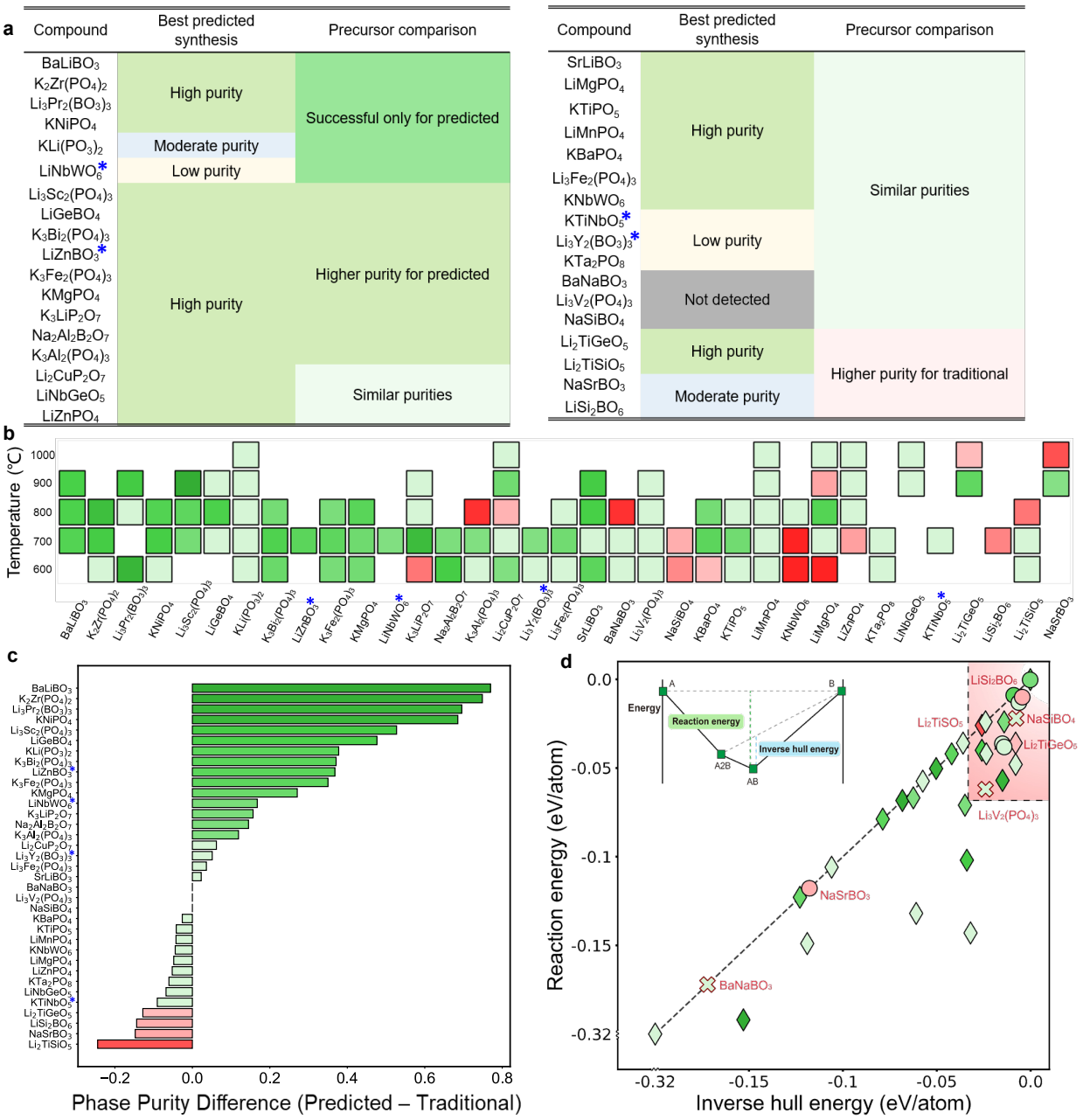

Figure 4.10: Robotic synthesis results of target materials from traditional versus predicted precursors. **a)** Table of the phase purity of 35 targets obtained from predicted precursors using the highest phase purity from various firing temperatures, compared to traditional precursors. Color of "Precursor comparison" column compares purity from predicted precursors versus traditional, where green means predicted precursors achieve >10% better purity, light green means they have purities within ±10%, and red means traditional precursors achieve >10% better purity. Targets with blue color star are metastable materials. Same color scheme is used in b, c, d. **b)** Heatmap of phase purity of predicted precursors at different calcination temperatures. **c)** shows the target phase purity from predicted precursors versus traditional precursors. **d)** Reaction energies and inverse hull energies for all targets. Marker shape corresponds to best phase purity of predicted precursors, where diamonds are high purity, circles are moderate and low purity, and crosses with red outline means both predicted precursors and traditional precursors failed. The dashed line represents when inverse hull energy equals reaction energy. *Inset*: Convex hull illustrating the reaction energy and the inverse hull energy.

We also examined the robotic solid-state synthesis of 4 metastable compounds with mild energies above the convex hull[7]—$LiNbWO_6$ (10 meV/atom), $LiZnBO_3$ (8 meV/atom), $KTiNbO_5$ (1 meV/atom), and $Li_3Y_2(BO_3)_3$ (39 meV/atom), indicated by blue asterisks in **Figure 4.10**. These metastable compounds formed in our solid-state reactions, although generally with low phase purity. However, we still found that our predicted precursors would yield these target metastable phases with similar or better relative purity than when starting from traditional precursors (see **Chapter 4.4.1**). A recent work by Zeng et al. suggests that by tuning the thermodynamic driving forces from the precursors, it may be possible to selectively form desired stable or metastable phases based on their calculated nucleation barriers.[42] Finally, in 3 systems, neither sets of precursors resulted in the target material, which for $NaBSiO_4$ was due to glass formation,[43] for $Li_3V_2(PO_4)_3$ a more reducing atmosphere was needed,[44] and for $NaBaBO_3$ the published reaction temperature[45] was very precise at 790°C, suggesting that perhaps a rounded number like 800°C may be too high. As discussed further in **Chapter 4.4.3**, these potential failure modes represent important considerations in future robotic laboratory design for solid-state synthesis.

Figure 4.10c shows that our predicted precursors tend to synthesize target materials with higher purity than traditional simple oxide precursors. Many of our predicted ternary oxide precursors are unusual, such as $LiPO_3$, $LiBO_2$, $LiNbO_3$ and more in **Table 4.2**—as these precursors do not appear from our previously text-mined database of 19,488 solid-state synthesis recipes.[46] Machine-learning algorithms for synthesis prediction trained on literature datasets would therefore be unlikely to predict our suggested precursors here. This highlights the limitations of machine-learning algorithms in predicting new opportunities in synthesis parameter space, outside the constraints of our anthropogenic biases in chemical reaction data.[47,22]

Our results show that the success of a reaction was not correlated to the crystal structure or chemistry of the target material—rather, it was primarily determined by the geometry of the underlying convex hull, as well as the magnitude of the thermodynamic driving force. The success of our precursor selection principles is somewhat surprising, considering we evaluate precursor selection using only the DFT-calculated convex hull—which does not account for temperature-dependent effects such as vibrational entropy or oxide decomposition; neglects kinetic considerations such as diffusion rates and nucleation barriers,[32] and has known errors in DFT-calculated formation energies.[48]

Here we rationalize with order-of-magnitude energy arguments why, despite many simplifying assumptions, the DFT-calculated thermodynamic convex hull retains predictive power in identifying effective precursors. (**Chapter 4.4.2**) First, entropic contributions can generally be neglected because the ΔG of an oxide synthesis reaction is usually dominated by the ΔH contribution, rather than the $T\Delta S$ contribution. **Figure 4.11** compiles a list of 100 experimental ternary oxide reaction energies, and shows that at 1000K the magnitude of $|\Delta G|$ for reactions are ~200 meV/atom, whereas the $|T\Delta S|$ contribution is only ~15 meV/atom. In 60% of the reactions, $|T\Delta S|/|\Delta G| < 10\%$, except in cases where $|\Delta G| < 100$ meV/atom, in which case $T\Delta S$ can be comparable in magnitude to ΔH. We validate these arguments in **Figure 4.12**, showing that temperature-dependent free-energies are negligibly different than reaction enthalpies.[49] The dominance of ΔH over $T\Delta S$ in oxide synthesis reactions is due to the irreversible exothermic nature of reactions of the form $A + B \rightarrow AB$; as opposed to first-order phase transitions like melting or polymorphic transformations, where $\Delta H \sim T\Delta S$. This assumption relies on both the reactants and products being solid phases—for reactions that evolve gases the reaction entropy is approximately

ΔS = 1 eV/atom/1000K; meaning that higher temperature largely favors the reaction direction with more moles of gas.

Second, ternary convex hulls are often skewed such that certain hull directions are much deeper than others, such as the Li_2O-B_2O_3 and BaO-B_2O_3 directions illustrated on the Li_2O-BaO-B_2O_3 convex hull in **Figure 4.1** (more examples in supplementary information of Jiadong Chen's paper[41]). On a high-dimensional phase diagram, there are many combinations of precursor pairs that can slice through a target phase. Even an approximate convex hull, with systematic DFT formation energy errors of 25 meV/atom,[48,8] can largely capture the relative depths of the convex hull in various compositional directions, as well as the complexity of the hull arising from competing phases. Importantly, DFT is well-poised to capture the very stable phases, which are low-energy thermodynamic sinks to be avoided when designing the reaction isopleths between pairs of precursors.

Finally, although we do not explicitly calculate kinetics here, the magnitude of the thermodynamic driving force is a good proxy for phase transformation kinetics, as $\Delta G_{reaction}$ appears in the denominator of the classical nucleation barrier, as supersaturation in the JMAK theory of crystal growth, and as $d\mu/dx$ in Fick's first law of diffusion.[50] Because we aim to evaluate the *relative* reaction kinetics of different precursors, rather than absolute kinetics, we can usually compare thermodynamic driving forces between different precursor sets without explicitly calculating diffusion barriers[51] or surface energies for nucleation and growth analyses.[52,53].

However, there are limits to this assumption. **Figure 4.10d** shows the reaction energy and inverse hull energy for all 35 reactions using predicted precursors, among which 3 of the unsuccessful syntheses are marked with a cross, and 4 red markers indicate conditions where the traditional precursors outperformed the predicted precursors. In cases where our predicted

precursors were less successful (red box in **Figure 4.10d**), the reaction energy landscapes were shallow with $\Delta E_{reaction}$ > -70 meV/atom, and inverse hull energies of ΔE_{IH} > -50 meV/atom. Because these driving forces are on the order of $k_B T$ at solid-state synthesis temperatures (~1000K), unanticipated kinetic processes may become rate-limiting and disqualify our thermodynamic driving force arguments. These counterexamples provide valuable 'failed synthesis' results[54] to quantify bounds where our precursor selection principles offer less certainty of success, and can serve as soft cutoff energies for future algorithms for solid-state precursor prediction—although we note that many reactions within this energy cutoff can still be successful as shown in our experiments.

Finally, additional opportunities to design large $\Delta G_{reaction}$ include leveraging metathesis reactions,[31,29] for example of the form 2 $NaCrS_2$ + $MgCl_2$ → $MgCr_2S_4$ + 2 NaCl;[55] where reactions can be thermodynamically driven by the formation of a stable salt byproduct. Because there are a wide variety of opportunities to select potential byproduct phases, metathesis reactions represent a rich design space to enhance the thermodynamics, and thereby the kinetics, of solid-state reactions.

4.4.1 Metastable materials synthesis efficacy

In this work, we also considered 4 target materials that are calculated in DFT to be metastable relative to the convex hull, meaning they have an energy above the hull. These metastable materials are listed in **Table 4.3**. We aimed to investigate if the materials were calculated to be metastable, if they were still synthesizable using predicted precursors. We chose $LiZnBO_3$, which is calculated in DFT to be metastable with respect to our predicted precursors ZnO + $LiBO_2$. We also chose $LiNbWO_6$, $KTiNbO_5$, and $Li_3Y_2(BO_3)_3$, which are metastable with respect to decomposition products that are not our precursors. We hypothesized that by starting

with precursors that are in a different 'compositional direction', we might be able to synthesize these metastable phases. To determine the predicted precursors for these metastable compounds, we constructed artificial entries for these compositions, but with an energy slightly smaller than the existing convex hull energy at that composition. For this work, we chose an arbitrary value of $\Delta E_{hull} = -0.01$ eV.

Of these four systems, we obtained a reasonably high target yield for $LiZnBO_3$, whereas the three metastable targets received low yields from both the predicted and traditional precursors. All three metastable materials were synthesized with low sample purity, ostensibly within the noise of the XRD characterization method. This illustrates that our algorithm is better suited to predict precursors for target materials that are convex hull stable, rather than metastable.

Table 4.3: Target materials that are not thermodynamic stable on the convex hull.

Target	Energy above hull (meV/atom)	Decomposition products	Target phase fraction	
			From predicted precursors	From traditional precursors
$LiZnBO_3$	8	1/3 ZnO + 2/3 $LiBO_2$	0.52	0.15
$LiNbWO_6$	10	$LiNb_3O_8$ + Li_2WO_4 + WO_3	0.17	0.05
$KTiNbO_5$	1	$K_4Nb_6O_{17}$ + $K_2Ti_6O_{13}$	0.18	0.27
$Li_3Y_2(BO_3)_3$	39	19/34 $Li_6Y(BO_3)_3$ + 15/34 YBO_3	0.17	0.12

4.4.2 Comparison of energy contribution between TΔS and ΔH

In this section, we compared the magnitude of the entropy contribution, $T\Delta S$, to the overall ΔG of a reaction. We used experimental thermochemical data queried through Materials Project API in the 'Experimental Data' field. This experimental thermochemical data originated from NIST JANAF, [56] Materials Thermochemistry, [57] and the CODATA Key Values for Thermodynamics.[58] We collected entropy (S) and formation enthalpy (H_f) data at 298K for all convex hull stable binary and ternary oxides among 49 common metal elements. Then, using the selected binary metal oxides as precursors, we generated all possible pairwise combination

reactions for the formation of the selected ternary oxides, resulting in exactly 100 reactions total. The energy contributions of $T\Delta S$, ΔH_f, reaction formation energy ΔG, are plotted in **Figure 4.11a**, **4.11b**, and **4.11c**, respectively. The ratio of the magnitude of the entropy contribution to total reaction energy magnitude ($|T\Delta S / \Delta G|$) was also calculated for each individual reaction, shown in **Figure 4.11d**.

Altogether, **Figure 4.11** indicates that for the majority of reactions, the energy contribution of entropy at 1000K is considerably smaller in magnitude than the total reaction energy. By choosing a characteristic synthesis temperature of 1000K, the distribution peak of |TΔS| term is ~15 meV/atom, while that of ΔH term is -185 meV/atom. Specifically, 60% of reactions have $|T\Delta S / \Delta G|$ values less than 0.1. Among the remaining 40% of reactions where $|T\Delta S / \Delta G|$ values are greater than or equal to 0.1, approximately half have a relatively low reaction formation energy ΔG (~100 meV/atom). Therefore, in the context of oxide synthesis reactions, entropic contributions are usually negligible due to the dominant contribution of the enthalpy ΔH to the free energy ΔG.

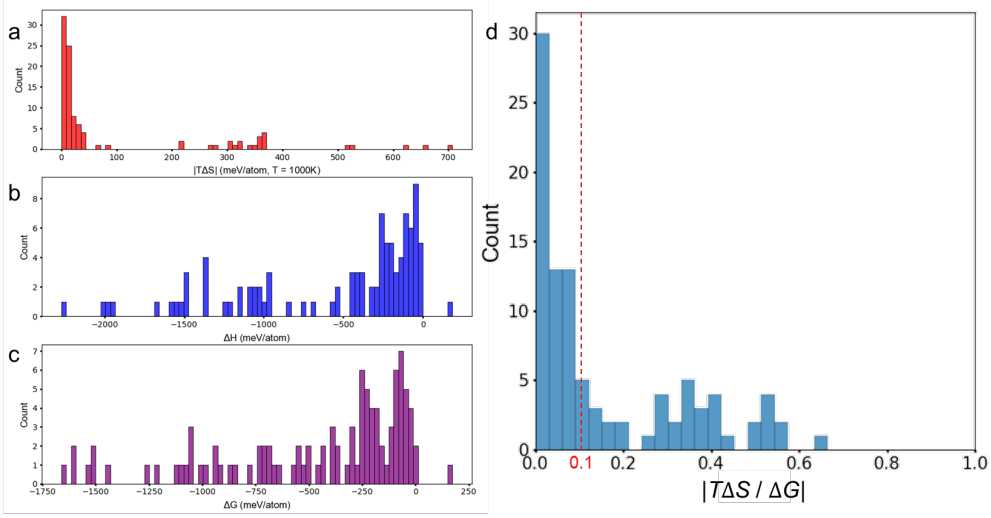

Figure 4.11: Histograms of **a**. $|T\Delta S|$, **b**. ΔH, **c**. ΔG, **d**. $|T\Delta S/\Delta G|$ of 100 reactions which uses binary metal oxides as reactants to synthesize ternary metal oxides in Materials Projects database. The entropy and enthalpy data we use is experimental data in room temperature (298K). The synthesis temperature T we choose is 1000K.

To explicitly illustrate that the temperature-dependent reaction free energies are negligible, **Figure 4.12** shows the candidate pairwise reaction *free-energies* for $LiZnPO_4$, $BaLiBO_3$, and $SrLiBO_3$ as a function of temperature. $BaLiBO_3$ and $LiZnPO_4$ are the systems from Figures 1 and 2 of the manuscript. These free-energy calculations were conducted utilizing the *GibbsStructureComputedEntry* module within the *Pymatgen* package, where Bartel *et al*. [Manuscript Reference 45] developed a physical descriptor to predict temperature-dependent Gibbs free energy using the SISSO (Sure Independence Screening and Sparsifying Operator) machine-learning approach. This module takes both materials structure and temperature as input parameters, and calculates the temperature-dependence of the free energy.

Figure 4.12 shows that as the temperature elevates from 0 to 1000K, the free energy of these solid-state reactions deviate from the reaction enthalpy by less than 10%. The magnitude of the TΔS contribution is much smaller than the difference in reaction enthalpies between the different precursors. Our result here reinforces the dominance of the enthalpy contribution in overall reaction energy, and supports the validity of our assumption in not accounting for the temperature-dependent free-energy in this study.

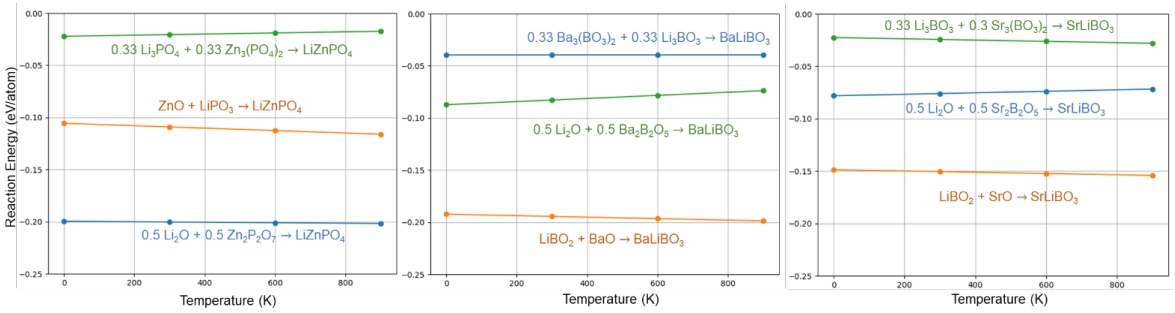

Figure 4.12: The relationship between reaction energy and temperature for three distinct pairwise reactions of $LiZnPO_4$ system.

We note that this assumption is relevant in because we have specifically chosen reactions in this study where the reactants and products are solids. When volatile gases are involved in a

solid-state reaction, the temperature dependence of the reaction is largely dominated by whether the reactant or product side has more moles of gas, which contribute an entropy of approximately ΔS = 1 eV/atom/1000K. (Note that by this normalization, 1 molecule of O_2 gas contributes 2 eV/atom at 1000K).

4.4.3 Failed synthesis: Summary/discussion

For a number of compounds, neither set of precursors produced an XRD signal matching the target crystal structure, and as such these synthesis attempts are classified as failures based on the XRD quantification method used in this study. While it is often not possible to determine the exact reason for an unsuccessful synthesis, there are several common factors that can result in failed synthesis even for a thermodynamically stable target:

1) **Insufficient synthesis temperature**

- If the calcination temperature is insufficient, some of the precursors may not fully decompose and react, and as a result does not form a uniform product.
- Likely applies to $KTiNbO_5$ and $Li_3Y_2(BO_3)_2$ in the present study.

2) **Evaporation of precursors**

- Some precursors have significant vapor pressure and are prone to being lost to evaporation during calcination, resulting in deficiency of the affected components.
- Well known to occur with Li, P, B precursors.
- The great majority of studies on Li-oxide synthesis for example add excess Li precursor, most often 10%, to hedge against evaporation. We did not do this here, since it was difficult to apply this uniformly over such a broad chemical space, including Na- and K- based compounds.
- It is hard to determine *a prioi* which samples evaporation could apply to here – usually this will affect purity more than overall success/failure, but it can be very impactful in cases where (a)

formation of the target phase requires high temperature and/or longer times, or (b) there is a small composition window for the target phase.

3) **Excessive oxidation during synthesis**

- For all ASTRAL synthesis experiments presented in this study, calcination was performed in ambient air, and as such each element will attain the most energetically favorable oxidation state based on reaction with oxygen gas at high temperature.
- For materials containing transition metals, this can result in incorrect oxidation states during synthesis, preventing formation of the target phase.
- Likely applies to $Li_3V_2(PO_4)_3$ – in the literature report, a reducing atmosphere ($Ar + H_2$) is used for the final synthesis reaction. Also, V has many available oxidation states (+2, +3, +4, +5), and for the target material we need V^{3+}, so it is reasonable to suspect that V^{5+} formation could be the cause of the failure.

4) **Amorphous synthesis products**

- ASTRAL classifies synthesis outcomes based on powder XRD, and so any amorphous phases present are not detected or used for quantification. This can result in an apparently failed synthesis, even in cases where the sample has formed a homogeneous mixture of the correct composition.
- For such glass forming compositions, successful crystallization requires controlled cooling, typically with a period of annealing at an appropriate temperature to nucleate and grow crystals.
- Likely applies to $KLi(PO_3)_2$ and $NaSiBO_4$ in the present study, as each (1) contains a high proportion of glass-forming elements, (2) each formed fully fused samples with a glassy appearance, and (3) despite adequate yield of reaction product, almost no crystalline peaks were observed on XRD.

4.5 Outlook

Synthesis science is poorly understood, but new theories can be developed by examining falsifiable predictions through empirical validation. In this work, we hypothesized several principles to identify superior precursors for high-purity synthesis of multicomponent oxides. We argued that in high-dimensional phase diagrams with skewed energy landscapes, there is an opportunity to find precursors that are both high in energy and have compositions that circumvent low-energy undesired kinetic byproducts. Using a robotic synthesis laboratory, we validated this hypothesis over 35 target materials with diverse crystal chemistries, producing in this one study as many experimental results as a typical review paper might survey.

This work heralds a new paradigm of data-driven experimental synthesis science, where the high throughput and reproducibility of robotic laboratories enable a more comprehensive interrogation of synthesis science hypotheses. This exciting robotic platform can be directed to investigate further fundamental questions, such as the role of temperatures and reaction times in ceramic oxide synthesis. As we use these robotic laboratories to verify human-designed hypotheses, we will deepen our fundamental understanding of the interplay between thermodynamics and kinetics during materials formation. Simultaneously, this scientific understanding will drive the development of physically-informed AI synthesis planning frameworks to enable truly autonomous materials processing and manufacturing.

[1] Jansen, Martin. "A concept for synthesis planning in solid-state chemistry." *Angewandte Chemie International Edition* 41.20 (2002): 3746-3766.

[2] Kovnir, Kirill. "Predictive synthesis." *Chemistry of Materials* 33.13 (2021): 4835-4841.

[3] Cheetham, Anthony K., Ram Seshadri, and Fred Wudl. "Chemical synthesis and materials discovery." *Nature Synthesis* 1.7 (2022): 514-520.

[4] Jenks, Cynthia, et al. *Basic Research Needs for Transformative Manufacturing*. US. DOE Office of Science (SC), 2020.

[5] Narayan, Awadhesh, et al. "Computational and experimental investigation for new transition metal selenides and sulfides: The importance of experimental verification for stability." *Physical Review B* 94.4 (2016): 045105.

[6] Acharya, Megha, et al. "Searching for new ferroelectric materials using high-throughput databases: An experimental perspective on BiAlO3 and BiInO3." *Chemistry of Materials* 32.17 (2020): 7274-7283.

[7] Sun, Wenhao, et al. "The thermodynamic scale of inorganic crystalline metastability." *Science advances* 2.11 (2016): e1600225.

[8] Bartel, Christopher J., et al. "The role of decomposition reactions in assessing first-principles predictions of solid stability." *npj Computational Materials* 5.1 (2019): 4.

[9] Chen, Hailong, Geoffroy Hautier, and Gerbrand Ceder. "Synthesis, computed stability, and crystal structure of a new family of inorganic compounds: carbonophosphates." *Journal of the American Chemical Society* 134.48 (2012): 19619-19627.

[10] Stach, Eric, et al. "Autonomous experimentation systems for materials development: A community perspective." *Matter* 4.9 (2021): 2702-2726.

[11] Szymanski, Nathan J., et al. "Toward autonomous design and synthesis of novel inorganic materials." *Materials horizons* 8.8 (2021): 2169-2198.

[12] Abolhasani, Milad, and Eugenia Kumacheva. "The rise of self-driving labs in chemical and materials sciences." *Nature Synthesis* (2023): 1-10.

[13] Kusne, A. Gilad, et al. "On-the-fly closed-loop materials discovery via Bayesian active learning." *Nature communications* 11.1 (2020): 5966.

[14] Zakutayev, Andriy, et al. "An open experimental database for exploring inorganic materials." *Scientific data* 5.1 (2018): 1-12

[15] MacLeod, Benjamin P., et al. "Self-driving laboratory for accelerated discovery of thin-film materials." *Science Advances* 6.20 (2020): eaaz8867.

[16] Burger, Benjamin, et al. "A mobile robotic chemist." *Nature* 583.7815 (2020): 237-241.

[17]Jonderian, Antranik, Michelle Ting, and Eric McCalla. "Metastability in Li–La–Ti–O perovskite materials and its impact on ionic conductivity." *Chemistry of Materials* 33.12 (2021): 4792-4804.

[18] Yang, Lusann, et al. "Discovery of complex oxides via automated experiments and data science." *Proceedings of the National Academy of Sciences* 118.37 (2021): e2106042118.

[19] Ament, Sebastian, et al. "Autonomous materials synthesis via hierarchical active learning of nonequilibrium phase diagrams." *Science Advances* 7.51 (2021): eabg4930.

[20] Anderson, Ethan, et al. "Combinatorial study of the Li-La-Zr-O system." *Solid State Ionics* 388 (2022): 116087.

[21] Young, Samuel D., et al. "Thermodynamic Stability and Anion Ordering of Perovskite Oxynitrides." *Chemistry of Materials* 35.15 (2023): 5975-5987.

[22] David, Nicholas, Wenhao Sun, and Connor W. Coley. "The promise and pitfalls of AI for molecular and materials synthesis." *Nature Computational Science* (2023): 1-3.

[23] Bruce, Duncan W., Dermot O'Hare, and Richard I. Walton, eds. *Functional oxides*. John Wiley & Sons, 2011.

[24] Tian, Yaosen, et al. "Promises and challenges of next-generation "beyond Li-ion" batteries for electric vehicles and grid decarbonization." *Chemical reviews* 121.3 (2020): 1623-1669.

[25] Hautier, Geoffroy, et al. "Phosphates as lithium-ion battery cathodes: an evaluation based on high-throughput ab initio calculations." *Chemistry of Materials* 23.15 (2011): 3495-3508.

[26]Zhao, Qing, et al. "Designing solid-state electrolytes for safe, energy-dense batteries." *Nature Reviews Materials* 5.3 (2020): 229-252.

[27] Miura, Akira, et al. "Observing and Modeling the Sequential Pairwise Reactions that Drive Solid-State Ceramic Synthesis." *Advanced Materials* 33.24 (2021): 2100312.

[28] Bianchini, Matteo, et al. "The interplay between thermodynamics and kinetics in the solid-state synthesis of layered oxides." *Nature materials* 19.10 (2020): 1088-1095.

[29] McDermott, Matthew J., Shyam S. Dwaraknath, and Kristin A. Persson. "A graph-based network for predicting chemical reaction pathways in solid-state materials synthesis." *Nature communications* 12.1 (2021): 3097.

[30] Evans, Daniel, et al. "Visualizing temperature-dependent phase stability in high entropy alloys." *npj Computational Materials* 7.1 (2021): 151.

[31] Todd, Paul K., et al. "Selectivity in yttrium manganese oxide synthesis via local chemical potentials in hyperdimensional phase space." *Journal of the American Chemical Society* 143.37 (2021): 15185-15194.

[32] Aykol, Muratahan, Joseph H. Montoya, and Jens Hummelshøj. "Rational solid-state synthesis routes for inorganic materials." *Journal of the American Chemical Society* 143.24 (2021): 9244-9259.

[33] Todd, Paul K., et al. "Selectivity in yttrium manganese oxide synthesis via local chemical potentials in hyperdimensional phase space." *Journal of the American Chemical Society* 143.37 (2021): 15185-15194.

[34] Aykol, Muratahan, Joseph H. Montoya, and Jens Hummelshøj. "Rational solid-state synthesis routes for inorganic materials." *Journal of the American Chemical Society* 143.24 (2021): 9244-9259.

[35] Sun, Wenhao, and Matthew J. Powell-Palm. "Generalized Gibbs' Phase Rule." arXiv preprint arXiv:2105.01337 (2021).

[36] Chen, Jiadong, Matthew J. Powell-Palm, and Wenhao Sun. "The geometry of high-dimensional phase diagrams: II. The duality between closed and open chemical systems." *arXiv preprint arXiv:2404.05197* (2024).

[37] Chen, Jiadong, Matthew J. Powell-Palm, and Wenhao Sun. "The geometry of high-dimensional phase diagrams: III. Engineering relative stability in four dimensions." *arXiv preprint arXiv:2404.05201* (2024).

[38] Jain, Anubhav, et al. "Commentary: The Materials Project: A materials genome approach to accelerating materials innovation." *APL materials* 1.1 (2013): 011002.

[39] He, Tanjin, et al. "Similarity of precursors in solid-state synthesis as text-mined from scientific literature." *Chemistry of Materials* 32.18 (2020): 7861-7873.

[40] Yoshikawa, Naruki, et al. "Digital pipette: Open hardware for liquid transfer in self-driving laboratories." (2023).

[41] Chen, Jiadong, et al. "Navigating phase diagram complexity to guide robotic inorganic materials synthesis." *Nature Synthesis* (2024): 1-9.

[42] Zeng, Yan, et al. "Selective formation of metastable polymorphs in solid-state synthesis." arXiv preprint arXiv:2309.05800 (2023).

[43] Feltz, A., and P. Büchner. "Structure and ionic conduction in solids: I. Na+-ion conducting glasses in the systems NaBSiO4-Na2SiO3, NaBSiO4-Na4SiO4 and NaBSiO4-Na3PO4." *Journal of non-crystalline solids* 92.2-3 (1987): 397-406.

[44] Chen, Shanhua, et al. "Kinetic Studies on the Synthesis of Monoclinic Li3V2 (PO4) 3 via Solid-State Reaction." *The Journal of Physical Chemistry A* 118.21 (2014): 3711-3716.

[45] Zhong, Jiyou, et al. "Understanding the blue-emitting orthoborate phosphor NaBaBO 3: Ce 3+ through experiment and computation." Journal of Materials Chemistry C 7.3 (2019): 654-662.

[46] Kononova, Olga, et al. "Text-mined dataset of inorganic materials synthesis recipes." *Scientific data* 6.1 (2019): 203.

[47] Jia, Xiwen, et al. "Anthropogenic biases in chemical reaction data hinder exploratory inorganic synthesis." *Nature* 573.7773 (2019): 251-255.

[48] Hautier, Geoffroy, et al. "Accuracy of density functional theory in predicting formation energies of ternary oxides from binary oxides and its implication on phase stability." *Physical Review B* 85.15 (2012): 155208.

[49] Bartel, Christopher J., et al. "Physical descriptor for the Gibbs energy of inorganic crystalline solids and temperature-dependent materials chemistry." *Nature communications* 9.1 (2018): 4168.

[50] Balluffi, Robert W., Samuel M. Allen, and W. Craig Carter. *Kinetics of materials*. John Wiley & Sons, 2005.

[51] Cosby, Monty R., et al. "Thermodynamic and Kinetic Barriers Limiting Solid-State Reactions Resolved through In Situ Synchrotron Studies of Lithium Halide Salts." *Chemistry of Materials* (2023).

[52] Sun, Wenhao, et al. "Nucleation of metastable aragonite CaCO3 in seawater." *Proceedings of the National Academy of Sciences* 112.11 (2015): 3199-3204.

[53] Sun, Wenhao, et al. "Non-equilibrium crystallization pathways of manganese oxides in aqueous solution." *Nature communications* 10.1 (2019): 573.

[54] Raccuglia, Paul, et al. "Machine-learning-assisted materials discovery using failed experiments." *Nature* 533.7601 (2016): 73-76.

[55] Miura, Akira, et al. "Selective metathesis synthesis of MgCr 2 S 4 by control of thermodynamic driving forces." *Materials horizons* 7.5 (2020): 1310-1316.

[56] Chase, Malcolm W., and National Information Standards Organization (US). NIST-JANAF thermochemical tables. Vol. 9. Washington, DC: American Chemical Society, 1998.

[57] Kubaschewski, Oswald, Charles B. Alcock, and P. J. Spencer. "Materials thermochemistry. revised." Pergamon Press Ltd, Headington Hill Hall, Oxford OX 3 0 BW, UK, 1993. 363 (1993).

[58] Cox, J. D., Wagman, D. D., and Medvedev, V. A., CODATA Key Values for Thermodynamics, Hemisphere Publishing Corp., New York, 1989.

Chapter 5 Conclusion and Outlook

Materials design, discovery, and optimization have been significantly accelerated by high throughput computation techniques such as density functional theory, molecular dynamics, Monte Carlo simulation, phase field simulation, machine learning, artificial intelligence, data mining, and big data analytics. The rapid analysis and computation of large volumes of data using computer technology facilitate the utilization of these advanced computational tools. However, looking back to 150 years ago, during an era devoid of such powerful computational resources, Gibbs and Maxwell constructed the first volume-entropy-Helmholtz free energy phase diagram manually, laying the groundwork for thermodynamics as the cornerstone of materials science. Now is an opportune moment to integrate classic thermodynamics more with modern computational resources, leveraging their capabilities to advance the field further.

We conclude this dissertation by re-iterating Gibbs' first sentence in thermodynamics: "*Although geometrical representations of propositions in the thermodynamics of fluids are in general use, and have done good service in disseminating clear notions in this science, yet they have by no means received the extension in respect to variety and generality of which they are capable*." Despite a rich 150-year-old history, equilibrium thermodynamics still has many exciting opportunities for fundamental development.

Altogether, this dissertation provides a foundation to construct, navigate, and interpret new varieties of phase diagrams, with thermodynamic axes beyond temperature, pressure, and composition, with as many axes as needed to capture all the essential physics of the thermodynamic

system. We have explored chemical potentials, pH, redox potential, particle size, impurity composition, and ion concentration, in the contexts of both solid-state and solvothermal synthesis across different solvent types, as well as for single-phase stability regions and relative stability across phase boundaries.

As is often the case with thermodynamics, it is not strictly necessary to have perfect thermochemical data before we can derive meaningful scientific insights, or formulate promising engineering decisions. Most importantly, one needs a robust understanding of the geometric *structure* of thermodynamics. If one can visualize and anticipate the underlying geometry of free energy surfaces, as well as the conditions of heterogeneous equilibrium, we will altogether eliminate confusion and strengthen our intuition for materials design. Hopefully, this will enable us to better exercise our creativity to design the complex functional materials that drive modern technology.

While the thermodynamic framework presented in this thesis holds promise for tackling a wide range of material synthesis challenges, there remain numerous unresolved questions that fall outside the purview of this dissertation. Addressing these inquiries would necessitate further methodological or theoretical advancements. Below, I outline several of these systems:

- Materials' extensive molar quantities are typically not fixed values; instead, they are often related to conjugate or other intensive variables. For example, in real life, metal oxides usually have a range of compositions, and the magnetic moment of a material can change in response to externally applied magnetic fields. The half-space intersection method that used in this dissertation is inadequate for handling this complex conjugate relationship. Is there a computationally efficient way to incorporate this complex relationship into high-dimensional phase diagrams?

- In Chapter 4, while we optimize the selection of precursors to increase phase purity, the determination of reaction temperature remains a trial-and-error process. What is the underlying mechanism behind the effect of reaction temperature on material formation? Can we predict the optimal reaction temperature and enhance our understanding of material science, rather than relying solely on machine learning algorithms?
- The computation of thermodynamic data in different solvents remains a significant challenge in constructing phase diagrams for solvothermal synthesis in non-aqueous solvents. Currently, most solubility and formation energy data are available primarily for aqueous systems. The experimental data and computational tools needed to calculate ion and solid energies in non-aqueous systems are either underdeveloped or still in need of further development.
- In experiments, how can we better control intensive variables, such as the chemical potential of metal elements or high magnetic fields? Our calculations indicate that most magnetic materials do not respond effectively until exposed to magnetic fields of hundreds of Teslas. However, achieving a 10 Tesla magnetic field in experiments is already considered very high.
- What new insights do automated labs bring to science? Without a deeper understanding of material formation, automated labs might simply accelerate the trial-and-error process, potentially leading to inefficient use of resources.